THE OXIDATION OF Fe-Mn ALLOYS IN CARBON DIOXIDE-CARBON MONOXIDE ATMOSPHERES AT 1000°C

THE OXIDATION OF Fe-Mn ALLOYS IN CARBON DIOXIDE-CARBON MONOXIDE ATMOSPHERES AT 1000°C

by

PETER MAYER, Dipl. Eng. (Met.)

A Thesis

Submitted to the Faculty of Graduate Studies

in Partial Fulfilment of the Requirements

for the Degree

Master of Engineering

McMaster University

February 1971

MASTER OF ENGINEERING (1971) McMaster University
(Metallurgy and Materials Science) Hamilton, Ontario.

TITLE: The Oxidation of Fe-Mn Alloys in Carbon Dioxide-Carbon Monoxide Atmospheres at 1000°C.

AUTHOR: Peter Mayer, Dipl. Eng. (Met.) (Slovak Technical University, Kosice, Czechoslovakia).

SUPERVISOR: Professor W. W. Smeltzer.

NUMBER OF PAGES: (xii) 130.

SCOPE AND CONTENTS:

The oxidation kinetics of iron-manganese alloys with manganese contents up to 60 w/o exposed to carbon dioxide-carbon monoxide atmospheres at 1000°C have been determined as a function of gas composition by a gravimetric technique. The experimental conditions were chosen in order that the product of the reaction between metal and oxidizing atmosphere would be a single-phase oxide scale.

The main objective of this study was to determine the oxidation characteristics of iron-manganese alloys. It has been found that the rate of oxidation of alloys up to 12% manganese at the early stages is limited by interfacial reaction control and later by diffusion processes in the oxide scale. Oxidation rates of alloys containing more than 27% manganese are entirely controlled by diffusion in the oxide scales. The experiments show that the linear oxidation rate is independent of alloy composition. On the other hand, the rate of parabolic oxidation becomes lower with increasing manganese content in the alloy.

The results from gravimetric measurements and chemical analyses have been interpreted by a model for the diffusion of iron and manganese through the wustite scale. The phenomenological equations from this theoretical

approach have enabled calculations of self-diffusion coefficients for iron and manganese and the concentration of defects in the FeO-MnO solid solution as a function of MnO content. The calculated defect concentrations are compared with theoretical models assuming different types of defect structures.

To my wife Tanya

ACKNOWLEDGMENTS

The author wishes to thank his supervisor, Dr. W. W. Smeltzer for his continuing guidance, encouragement, help and advice throughout the course of this study. The author is indebted to many of the faculty, post-doctoral fellows, graduate students and technical staff in the Department of Metallurgy and Materials Science for their helpful discussion and aid. The manuscript was typed with skill and remarkable patience by Miss BettyAnne Bedell, to whom I give special thanks.

The author gratefully acknowledges the following groups for their financial support: The Department of Metallurgy and Materials Science of McMaster University for the graduate fellowship and the National Research Council for the research grants to Dr. Smeltzer.

TABLE OF CONTENTS

		PAGE
CHAPTER I	INTRODUCTION	1
CHAPTER II	GENERAL PRINCIPLES OF OXIDATION	3
2.1	Introduction	3
2.2	Oxidation of Pure Metals	3
2.2.1	Oxidation Kinetics	5
2.2.2	Wagner's Theory of Parabolic Oxidation	7
2.3	Oxidation of Alloys	11
2.3.1	Classification of Modes of Alloy Oxidation	13
2.3.2	The Oxidation Rate and the Distribution of Cations in Oxide	15
2.3.3	Variation of Defect Concentration in Mixed Oxides Forming Continuous Ideal Solid Solutions	21
CHAPTER III	PRINCIPLES OF OXIDATION IN CO_2-CO ATMOSPHERES	24
3.1	Oxidation of Iron	24
3.1.1	Thermodynamics	24
3.1.2	Properties and Structures of FeO	26
3.1.3	Mechanisms and Kinetics of Iron Oxidation	29
3.2	Oxidation of Manganese	31
3.2.1	Thermodynamics	31
3.2.2	Properties and Structure of MnO	33
3.2.3	Mechanisms and Kinetics of Manganese Oxidation	34
3.3	Oxidation of Fe-Mn Alloys	35

		PAGE
3.3.1	Thermodynamics	35
3.3.2	Properties and Structure of FeO-MnO Solid Solutions	37
3.3.3	Oxidation of Fe-Mn Alloys	39
CHAPTER IV	EXPERIMENTAL TECHNIQUES	41
4.1	Introduction	41
4.2	Alloy and Specimen Preparation	41
4.3	Oxidation Apparatus	42
4.4	Oxidation Procedure	46
4.5	Analytical and Examination Methods	47
CHAPTER V	EXPERIMENTAL RESULTS	55
5.1	Introduction	55
5.2	Oxidation Kinetics	55
5.3	Scale Structure and Composition	63
5.3.1	Metallography and Microscopic Observations	63
5.3.2	X-ray and Chemical Analyses	65
5.3.3	Concentration Profiles in Metal and Oxide Scale	65
CHAPTER VI	ANALYSIS AND DISCUSSION OF EXPERIMENTAL RESULTS	78
6.1	Introduction	78
6.2	Reaction Rates	78
6.2.1	Linear Oxidation	79
6.2.2	Parabolic Oxidation Kinetics	85
6.3	Self-Diffusion Coefficients of Cations in FeO-MnO Solid Solutions	95
6.4	Concentration and Type of Defects in FeO-MnO Solid Solutions	105

		PAGE
6.5	Proposals for Future Work	123
CHAPTER VII	CONCLUSIONS	126
REFERENCES		128

LIST OF TABLES

TABLE	TITLE	PAGE
4.1	Computer Program Used to Calculate the Corrections of Electron Probe Microanalyzer Measurements.	52
5.1	Chemical Analyses of Fe-Mn Alloys.	56
5.2	Oxidizing Atmospheres and Corresponding Oxygen Potentials at 1000°C and 1 atm of Total Pressure.	57
5.3	Results of Volumetric and X-ray Diffraction Analysis	67
5.4	The Deviation Limits of Microprobe Measurements of Concentration Profiles in Alloys and Oxide Scales.	75
6.1	Second Linear Oxidation Rate [g/cm^2]	83
6.2	Parabolic Oxidation Rate Constant for Fe-Mn Alloys in CO_2-CO Atmospheres at 1000°C.	91
6.3	Least-Square Approximations for Parabolic Oxidation Constands as a Function of C_{Mn} (w/o Mn in Alloy) in Fe-Mn Alloys.	93
6.4	Self-Diffusion Coefficients of Iron at 1000°C in the FeO-MnO Solid Solution.	101
6.5	Self-Diffusion Coefficients of Manganese at 1000°C in the FeO-MnO Solid Solution.	103
6.6	Calculated Values of Defect Concentration from Present Investigation.	107

LIST OF FIGURES

		PAGE
Figure 2.1	Schematic representation of a simple, single layered MO p-type scale growing on M.	9
Figure 2.2	Oxidation modes of alloys.	14
Figure 3.1	Standard free energy of formation for oxides of iron and corresponding equilibrium ratio of CO_2 and CO as a function of temperature.	25
Figure 3.2	Standard free energy of formation for oxides of manganese and corresponding equilibrium ratio of CO_2 and CO as a function of temperature.	32
Figure 3.3	The equilibrium oxygen potential (2 log CO_2/CO) as a function of FeO content in FeO-MnO solid solution in equilibrium with Fe-Mn alloy.	36
Figure 3.4	Concentration of vacancies as a function of MnO content in the oxide.	40
Figure 4.1	Schema of experimental assembly.	43
Figure 4.2	Electron probe calibration for iron-manganese alloys.	50
Figure 4.3	Electron probe calibration for FeO-MnO solid solution.	51
Figure 5.1	Oxidation kinetics.	59
Figure 5.2	Oxidation kinetics.	60
Figure 5.3	Oxidation kinetics.	61
Figure 5.4	Oxidation kinetics.	62
Figure 5.5	The metallographical cross section of oxidized Fe-12.33% Mn alloy in CO_2-CO = 70/30 atmosphere at 1000°C. 30X.	64
Figure 5.6	Diffraction pattern from scale formed on Fe-12.33% Mn alloy.	66
Figure 5.7	Lattice parameter as a function of MnO content in the FeO-MnO solid solution.	68

		PAGE
Figure 5.8	Concentration profiles for Mn in alloy and MnO in oxide of Fe-0.93% Mn alloy oxidized at 1000°C.	69
Figure 5.9	Concentration profiles for Mn in alloy and MnO in oxide of Fe-12.33% Mn alloy oxidized at 1000°C.	70
Figure 5.10	Concentration profiles for Mn in alloy and MnO in oxide of Fe-27.35% Mn alloy oxidized at 1000°C.	71
Figure 5.11	Concentration profiles for Mn in alloy and MnO in oxide of Fe-31.83% Mn alloy oxidized at 1000°C.	72
Figure 5.12	Concentration profiles for Mn in alloy and MnO in oxide of Fe-59.04% Mn alloy oxidized at 1000°C.	73
Figure 5.13	Line scan for distribution of Mn in the alloy matrix and oxide phase near the internal interface.	76
Figure 6.1	Linear oxidation kinetics.	81
Figure 6.2	Linear oxidation kinetics.	82
Figure 6.3	Linear oxidation constant as a function of Mn content in Fe-Mn alloys.	84
Figure 6.4	Parabolic oxidation kinetics.	87
Figure 6.5	Parabolic oxidation kinetics.	88
Figure 6.6	Parabolic oxidation kinetics.	89
Figure 6.7	Parabolic oxidation kinetics.	90
Figure 6.8	Parabolic oxidation constant as a function of Mn content in Fe-Mn alloys.	92
Figure 6.9	Self-diffusion coefficient of iron as a function of MnO content in the FeO-MnO solid solution at 1000°C.	102
Figure 6.10	Self-diffusion coefficient of manganese as a function of MnO content in the FeO-MnO solid solution at 1000°C.	105
Figure 6.11	Variation of concentration of defects in FeO-MnO solid solutions in CO_2/CO = 70/30 atmosphere.	108
Figure 6.12	Variation of concentration of defects in FeO-MnO solid solutions in CO_2/CO = 50/50 atmosphere.	110

PAGE

Figure 6.13 Dependence of standard free energy change of oxygen dissolution in FeO-MnO solid solution at 1000°C on mole fraction of MnO in oxide. 118

Figure 6.14 Dependence of standard free energy change of oxygen dissolution in FeO-MnO solid solution at 1000°C on mole fraction of MnO in oxide. 119

Figure 6.15 Auxiliary plot for the complex type defect model. 121

Figure 6.16 Auxiliary plot for the simple type defect model. 122

Figure 6.17 Logarithms of defect concentration vs. concentration of MnO in scale. 124

CHAPTER I

INTRODUCTION

One of the major alloys in use today is steel. Steel generally must be of uniform structure and composition and exhibit sufficient strength for different design specifications. These unique properties are attained by the addition of alloying elements. The most often occurring alloying element in steel production is manganese. The concentrations of manganese vary in a wide range depending on purpose of use. During the manufacturing process the steel is often exposed to the oxidizing atmosphere with reduced oxygen potential in heating and annealing furnaces. Excessive surface oxidation is usually undesirable because an excessive amount of metal is wasted and the external and internal oxidation leads to steels of inferior mechanical properties.

The present experiments were designed to investigate the influence of manganese on oxidation properties of Fe-Mn alloys at high temperatures. In order to simulate the actual manufacturing conditions, CO_2-CO atmospheres at 1000°C were used. The chosen experimental problem is in fact a simplified industrial case.

Preliminary experiments were done on simultaneous decarburization and exclusive internal oxidation of Fe-Mn-C alloys. The experiments showed that the carbon content up to 1 w/o does not have any influence on internal oxidation kinetics except for early stages at very low oxygen potentials. The results of this work are not included in this thesis.

In the presented work, the oxidation kinetics, morphological development and compositions of the wustite scale on Fe-Mn alloys exposed to CO_2-CO atmospheres at 1000°C were investigated. The experiments were carried out under the conditions to insure formation of only a single phase FeO-MnO solid solution oxide scale.

The experimental results were obtained by a thermogravimetric method in the form of weight-gain time continuous recordings. Alloys exhibited parabolic oxidation kinetics, when the diffusion through the oxide phase was the rate limiting process. However, the alloys exhibited in the early stages linear oxidation kinetics, when the phase boundary reaction between the solid and gas was the rate limiting reaction.

The following sections present a literature survey on the subject, description of the experimental and analytical techniques, experimental results and discussion. Further, the experimental results are used to calculate the transport properties of the FeO-MnO solid solution at 1000°C. Because of the unique properties of the FeO-MnO solution, the concentration of point defects and its dependence on composition of the oxide solution could be calculated from transport properties. The calculated dependence enables an assessment of the type of defects occurring in the system. Proposals for future work are outlined in the last section of the discussion.

CHAPTER II

GENERAL PRINCIPLES OF OXIDATION

2.1 Introduction

The following section summarizes the literature relevant to the problem of alloy oxidation which bear on this study along with brief discussion of pertinent metal and alloy oxidation principles.

2.2 Oxidation of Pure Metals

All metals, except gold, form stable oxides upon exposure to normal atmospheric or extreme corrosion and oxidation conditions. The type of oxide formed depends on the thermodynamic properties of the metal under consideration, the type of oxidizing atmosphere and temperature. The rate at which oxide is formed varies widely depending on temperature, type of oxidizing atmosphere, gas flow rate, surface preparation and pre-treatment of exposed metal.

Usually the oxides formed on the surface of a metal are not stoichiometric compounds. The nonstoichiometry in oxides is equivalent to the presence of point defects. In order to conserve the electrical neutrality, complementary valence or electronic defects are simultaneously created. This kind of structure is characteristic for semiconductors. The conductivity of oxides, like that of semiconductors is several orders of magnitude lower than that of metals. The approximate limits at room temperature being $10^{-10} \div 10^{1}\ \Omega^{-1}$. The positive temperature coefficients also confirm the semiconducting character of oxides. The conductivity of oxides is, therefore,

predominately electronic, and is due to the movement of electronic defect (electron holes or electrons).

If the conductivity occurs by transport of electrons, the oxides are characterized by either excess cations present in interstitial positions in the oxide lattice, such as ZnO, or by anion vacancies in lattice positions, such as ZrO_2, and are classified as metal excess oxides. Similarly, if the conductivity occurs by transport of electron holes, the oxides are characterized by cation vacancies in lattice positions, such as FeO, MnO, CoO, etc., or by anions in interstitial positions (only one case of this kind was discovered by oxidation of Si, involving diffusion of interstitial O_2 molecules in silica), and are classified as metal deficit oxides.

The extent and type of nonstoichiometry in an oxide is dependent on the temperature and on partial pressure of its components in the surrounding. For metal excess oxides it is seen that nonstoichiometry increases with decreasing oxygen pressure. It has been shown that these oxides have a principal oxygen pressure dependence ranging from $P_{O_2}^{-1/2}$ to $P_{O_2}^{-1/6}$ for concentration of oxygen vacancies and metal interstitials respectively. For metal deficit oxides the concentration of defects increases with the square to sixth root of oxygen pressure.

The knowledge and understanding of defect structures in oxides may be obtained through studies of properties and reactions which are dependent on the concentration of ionic and electronic defects. Standard techniques are thermogravimetric measurements of nonstoichiometry and studies of electrical conductivity. These studies are necessary, for evaluation of the type of structure which predominates in a particular oxide.

2.2.1 Oxidation Kinetics

The formation of a metal oxide as a result of the action of oxygen on the metal at elevated temperatures appears to be one of the simple reactions, but it is not really so. The reaction product frequently is a compact phase, which separates the reacting substances from each other, and further reaction is possible only if at least one of the reactants diffuses through the layer to the other reaction partner. The diffusion process of the atoms via interstitial or vacant lattice sites is caused within a homogeneous solid by a concentration or a electrical gradient. In such cases, the course of the reaction is determined by diffusion process and phase-boundary reactions. Generally, there are several partial processes as phase boundary reactions, diffusion of cations, anions and electrons through the scale and transport processes in space charge boundary layers in the case of thin tarnishing layers at low temperatures. The slowest one is therefore the rate determining step.

Methods of investigating the rate of oxidation include determinations of the changes in thickness of scale, in weight of sample or in the volume of oxygen consumed from the atmosphere as a function of time. Because of the very complexity of the oxidation processes, the rate laws observed in the oxidation of metals may take various forms. Most quantitative data were obtained as changes in weight (Δm) per unit surface area (A) which are directly proportional to the oxide thickness, if it can be assumed, that density is constant throughout the oxide layer.

$$\frac{\Delta m}{A} = \frac{\text{mol. wt. of oxygen}}{\text{mol. wt. of oxide}} \cdot \rho . x \qquad (2.1)$$

where ρ - density of oxide

x - thickness of oxide layer.

The simplest rate law observed is the linear relationship,

$$\frac{\Delta m}{A} = k_L t \qquad (2.2)$$

where k_L - linear scaling rate constant

t - time.

This type of behaviour is associated with growth of porous films where the direct contact occurs between metal and gas, such as for the alkali metals. It was also observed in growth of compact scales, such as wustite in CO_2-CO atomospheres when diffusion in the scale is sufficiently rapid and the rate controlling step is chemical reaction at the oxide-gas interface.

The most common type of oxidation behaviour, and also best-described theoretically is the parabolic relationship which will be discussed in more detail later. In this case the oxidation rate is inversely proportional to the film thickness

$$\frac{dx}{dt} = \frac{k_p}{x} \qquad (2.3)$$

Integration of the equation (2.3) and substitution into (2.1) yields the parabolic relationship

$$\left(\frac{\Delta m}{A}\right)^2 = k_p t + C \qquad (2.4)$$

where k_p - parabolic rate scaling constant. In this case the rate controlling step is diffusion of either cations or anions across a relatively compact layer.

Experimental values have occasionally been found to agree with a cubic relationship

$$(\Delta m)^3 = K_k.t \tag{2.5}$$

or logarithmic

$$\Delta m = k_\ell.\log\ (a.t + t_0) \tag{2.6}$$

and also inverse logarithmic

$$\frac{1}{\Delta m} = A - k_{iL} \log t\ . \tag{2.7}$$

These relationships are most applicable in describing the formation of very thin films at lower temperatures.

Combinations of two or more of these rate laws in a single oxidation-time curve are also quite common. In most cases, the temperature effect of the rate laws previously described can be expressed by an Arrhenius relationship

$$k = k_0\ e^{-Q/RT} \tag{2.8}$$

2.2.2 Wagner's Theory of Parabolic Oxidation

If the concentrations of ionic and electronic defects in a metal oxide as functions of the respective independent thermodynamic variables and the mobilities of these defects in an oxide are known and, furthermore, the rates of the phase boundary reactions involved are known, it is possible to calculate the scaling rate of a metal from these data provided that no irregularities such as break away of the oxide occurs. Conversely, it is

possible to obtain information regarding lattice defects or phase boundary reactions from the observations on the oxidation kinetics.

Wagner[1] in 1933 published a general theory of high temperature oxidation of metals for the growth of a one-phase compact scale. This situation is often considered as the simplest in oxidation practice. Oxide is considered to be a nonstoichiometric, p-type or n-type semiconductor.

If we take a metal deficit oxide, as an example, Fig. 2.1, with a virtually perfect anion lattice, but with vacancies in the cation sublattice, the electrical neutrality is maintained by the inclusion of higher valency cations in the cation sublattice. Because there is an oxygen pressure or activity difference across the scale, fixed by equilibrium dissociation pressure of the considered oxide in the contact with metal at the metal-oxide interface, π_{MO_x}, and by the ambient atmosphere at the gas oxide interface, P_{O_2}, there exists an activity or concentration gradient of cation vacancies. The driving force is essentially the free energy change associated with the oxide formation from metal and oxygen. Reactions at phase boundaries are considered to be rapid and it is assumed that thermodynamic equilibrium persist at the interfaces. Consequently, volume diffusion of reacting ions under the chemical potential gradient is rate-determining. This consideration is valid when the scale is sufficiently thick since the electrical potential gradient is then negligible.

Wagner's classical work[1] shows that growth could be expected to follow a parabolic relationship under these conditions. Two processes are necessary to maintain scale growth. Electrons move rapidly through

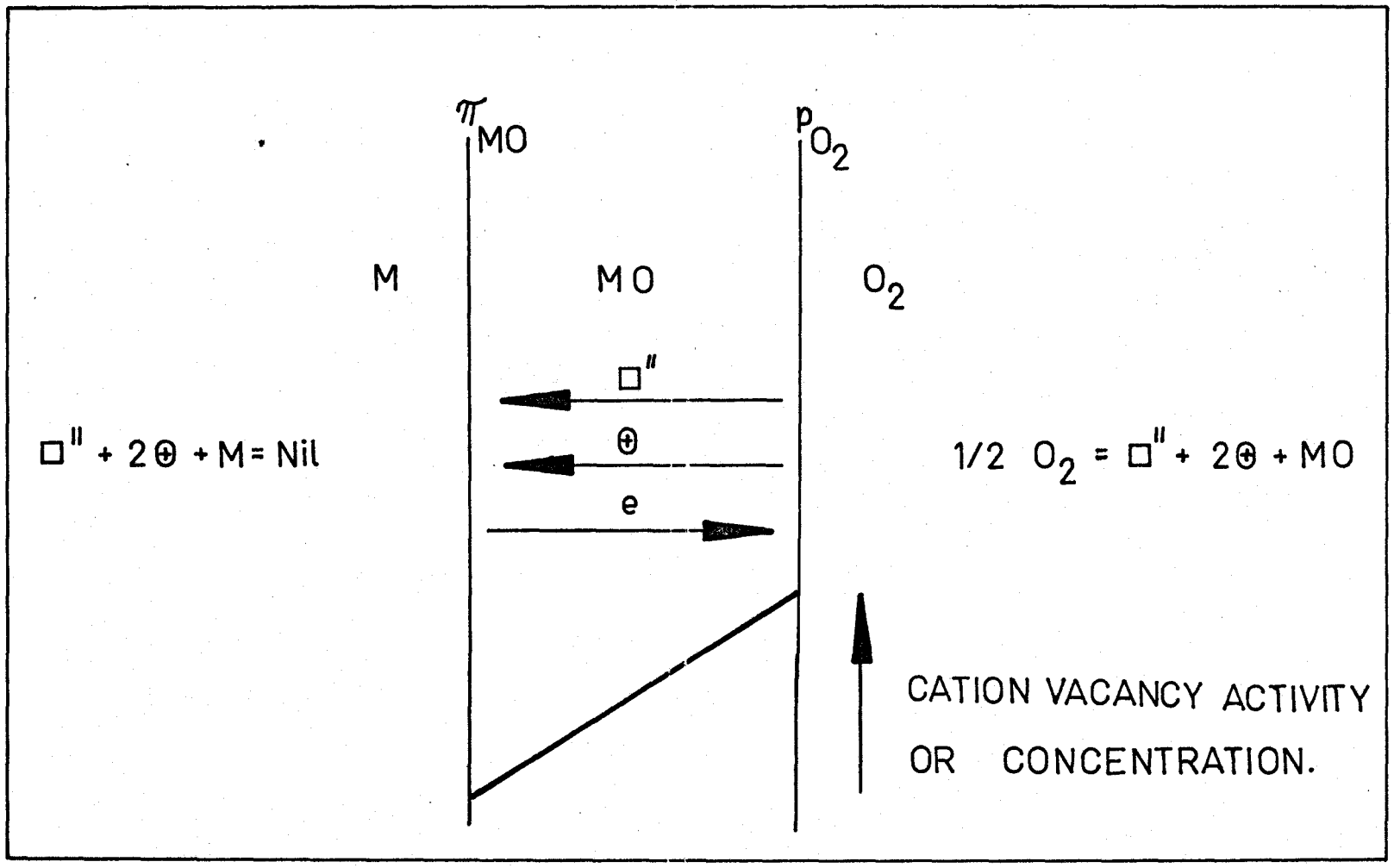

Figure 2.1 Schematic representation of a simple, single layered MO p-type scale growing on M.

the film to ionize chemisorbed oxygen atoms on the outer scale surface. The cations, which move slower and are rate determining, diffuse independently through the cation vacancies, principally under the vacancy activity gradient, to form fresh oxide at the outer surface. Effectively, cation vacancies are moving in the opposite direction and must be absorbed at the scale-metal interface.

The original form of the derived expression for the parabolic scaling rate constant was in terms of electrical conductivity and transference numbers of ions and electrons. The most popular form of the relation makes use of more easily determined ion diffusivities. Wagner writes the following expression for the rational rate constant

$$k_r = C_{eq.} \int_{a_{1(0)}}^{a_{1(i)}} (D_2^* \left(\frac{Z_2}{Z_1}\right) + D_1^*) \, d \ln a_1 \qquad (2.9)$$

or

$$k_r = C_{eq} \int_{a_{2(i)}}^{a_{2(0)}} (D_1^* \left(\frac{Z_1}{Z_2}\right) + D_2^*) \, d \ln a_2 \qquad (2.10)$$

where

k_r — rational rate constant in equivalents /cm^2/sec. (for a reaction product 1 cm thick).

$a_{1,2(0)}$ - activity of metal, resp. oxygen at oxide-gas interface.

$a_{1,2(i)}$ - activity of metal, resp. oxygen at metal-oxide interface.

Z_2 - valence of oxygen.

Z_1 - valence of metal.

D_1 - cation diffusivity.

D_2 - anion diffusivity.

$C_{eq} = C_1 Z_1$ or $C_2 Z_2$ equivalent concentration in equivalents /cm^3.

These equations demonstrate that in general the oxidation rate depends upon the difference in activity of the migrating species across the scale, and that large diffusivities mean increased attack of the metal. Equation (2.9) has been verified for a number of cases[1, 2, 3] and most rigorously for the oxidation of copper[4] to Cu_2O. Equation (2.10) has been successfully tested for the oxidation of cobalt[5], iron[6] and nickel[7].

This simple and elegant model has been questioned in several respects in recent years. The lattice defect and electron defect properties of oxides are probably much more complex than originally suggested. For example, the number of electron holes ionized or associated with each cation vacancy may be temperature dependent and may also vary with oxygen pressure [8, 9, 10]. The complex formation, diffusion and interaction of these variously charged vacancies through an oxide scale might well influence the oxidation kinetics[11].

2.3 Oxidation of Alloys

Oxidation of alloys involves more general phenomena than those previously discussed and described for pure metals. Since alloys contain two or more oxidizable constituents, a number of additional factors and

parameters must be taken into account if a comprehensive description of the oxidation behaviour of alloys is to be given. As a result the oxidation mechanisms for alloys are extremely complex.

If an alloy is subjected to oxidation, one component is, in general, oxidized preferentially because the alloy components have different affinities for oxygen. Differences in diffusion rates for different alloy components in metal and oxide give rise to concentration gradients within metal and oxide. Consequently the simple kinetic rate equations are often not followed and the compositions of scale and alloy change in complex ways with time. The second component may enter the scale, affecting its lattice defect structure, or may accumulate a metal or an oxide beneath the main scale. Also, if oxygen diffuses into the alloy in atomic form, precipitation of the oxide of less noble metal may occur as internal oxide. When it is considered that scales crack, contain voids, spall, sinter and give multiple layers of irregular thickness, it is clear that the general situation is complex.

Thermodynamics, usually in the form of ternary equilibrium diagrams involving two alloying elements and oxygen, are useful in predicting the alloying element likely to be preferentially oxidized and sometimes the likely steady-state scale. They can also provide information on subsequent reactions, such as the changes occurring when internal oxide is incorporated into the scale. In order to clarify these complex phenomena it is often useful to consider alloy oxidation by certain limiting cases, applicable specifically to binary alloys, which can be treated qualitatively and often semiquantitatively.

2.3.1 Classification of Modes of Alloy Oxidation

When an alloy is oxidized, the oxides of the components may be completely miscible, producing an oxide solid solution, or they may be completely or partially immiscible, producing multiphase scales. Classification due to Moreau and Benard[12], and Wood[13] permits the subsequent discussion to be seen in the perspective of the entire alloy oxidation scene.

An alloy AB represents, the general alloy under consideration, in which A is the more noble metal and B the less noble metal. Initially, the special case of the exclusive oxidation of one alloy component is considered before proceeding to the more general case where both components oxidize (Fig. 2.2).

Class I - Only one of the elements oxidizes under the prevailing conditions, giving BO. (a) The addition (minor) element B oxidizes under given conditions: (1.) internally, giving BO particles in a matrix of A, the oxygen pressure in the atmosphere being less than dissociation pressure of AO. Fig. 2.2.a). (2.) exclusively externally, giving a single layer of BO above an alloy matrix depleted in B since the oxygen pressure in the atmosphere is again usually less than the dissociation pressure of AO. A special case of this latter situation exists, however, where both elements can oxidize but the kinetic and geometrical conditions permit B to be selectively oxidized. (Fig. 2.2.b).

(b) The element is now the major element and oxidizes exclusively: (1) leaving the nonoxidizable metal A dispersed in BO (Fig. 2.2.c). (2) leaving the nonoxidizable metal A in an A-enriched zone beneath the BO scale (Fig. 2.2.d).

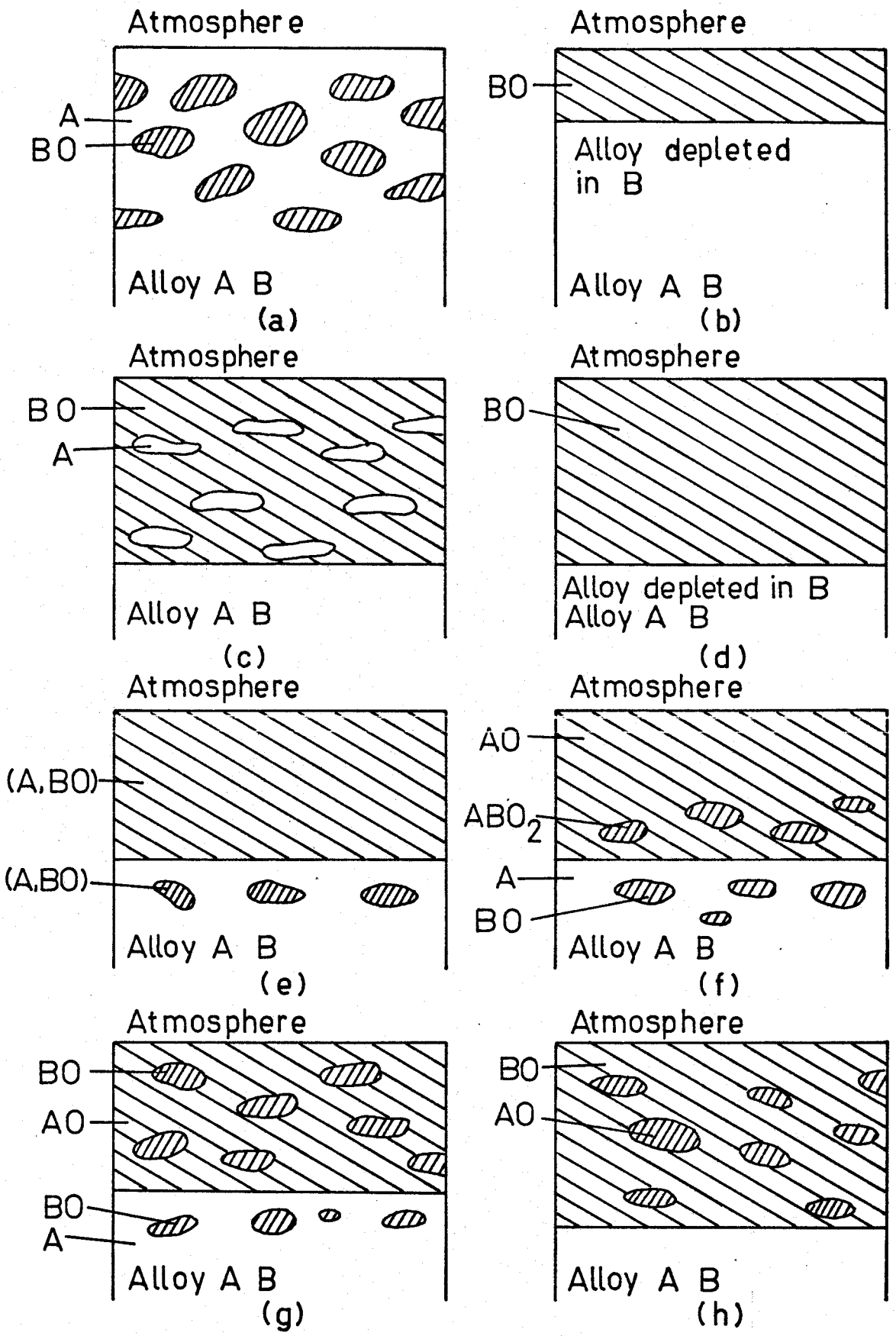

Figure 2.2 Oxidation Modes of Alloys.

Class II - Both alloying elements oxidize simultaneously to give AO and BO, the oxygen pressure in the atmosphere being greater than the equilibrium dissociation pressures of both oxides. (a) AO and BO react to give a compound: (1) AO and BO give a solid solution (A,B)O (Fig. 2.2.e). In practice, some internal (A,B)O richer in B than the surface scale if found in the alloy. (2) a double oxide is formed, often as a spinel, which may give a complete surface layer of variable composition, or particles incorporated into a matrix of AO, if the reaction is incomplete (Fig. 2.2.f). (b) AO and BO are virtually insoluble in each other: (1) the less noble metal B is minor component and the internal oxide of BO lies beneath a mixed layer of AO and BO (Fig. 2.2.g). (2) the less noble element is the major component so that no internal oxidation is observed but conditions may develop so that the AO oxide particles link up to give a complete layer underneath of BO (Fig. 2.2.h).

From this classification, it is apparent that there is not a single comprehensive theory of alloy oxidation. Rather there is a sequence of special cases. Furthermore, it must be recognized that in certain alloy systems several classifications of behaviour are possible depending on the composition, and oxidation atmosphere, temperature, pressure, time, etc. Changes from one type of behaviour to another may occur on a single specimen.

2.3.2 The Oxidation Rate and the Distribution of Cations in Oxide

Owing to the complexity of alloy oxidation, it is often difficult to give an overall quantitative description of the process. Hence, at the present

stage of our knowledge, the oxidation behaviour of alloys may not be easily predicted except for relatively simple systems. In view of the fact that the present investigation is concerned with an example of a relatively simple system, theoretical treatment of the problem will be discussed in detail.

In this system, an alloy of metals A and B of equal valence reacts with nonmetal X, e.g., oxygen. A scale consisting of a solid solution of the corresponding compounds is formed. In general the ratio of the number of moles of metals A and B in the scale is not equal to the ratio in the alloy inasmuch as the less noble metal tends to enter the scale preferentially. Further, in view of different diffusivities of cations, the ratio of metals A and B in the scale varies with distance X from the alloy-scale interface.

For theoretical calculation of the overall scaling rate as a function of alloy composition it is necessary to know the local distribution of A and B in the scale. Thus, it is necessary to calculate the concentration profiles in scale. Wagner[14] has very recently treated the subject theoretically. This model provides the basis for considering the general distribution of cations through oxide scales formed on alloys. In order to treat this problem theoretically the following presuppositions are needed to be satisfied: (1) The Alloy A-B may be a single phase or two-phase alloy whose initial composition is uniform. (2) The scale consists only of a single phase. (3) Exclusive diffusion control is presumed. (4) The alloy is given as a flat sample and the alloy-scale interface is presumed to be planar. (5) In the scale, metal only diffuses and the oxide exhibits only small deviations from stoichiometry.

In general the flux of the ions of A and B in the scale is due to both a concentration and electrical gradients. It is, however, not necessary to consider details of the driving force for movement of the ions. In the following derivation, correlation effects are disregarded. Thus equations for the flux of cations in the scale are

$$\dot{J}_{A(eq)} = - D_A \frac{(1-\xi)}{V_{eq}} \cdot \frac{\partial \ln a_A}{dx} \tag{2.11}$$

$$J_{B(eq)} = - \frac{D_B \xi}{V_{eq}} \cdot \frac{\partial \ln a_B}{dx} \tag{2.12}$$

where

$\dot{J}_{A(eq)}$, $\dot{J}_{B(eq)}$ - transport rates of ions in equivalents per unit area and time.

ξ - local equivalent fraction of B(0).

D_A, D_B - self diffusion coefficients.

V_{eq} - volume per equivalent of A(0), B(0) in scale.

a_A, a_B - activities of A and B.

x - distance from the alloy-scale interface in scale.

A solid solution A(o) - B(o) involving derivations from the ideal metal-to-nonmetal ratio must be treated as a ternary system. In addition to pressure P, temperature T and ξ, one has, therefore a fourth independent variable, which may be chosen to be activity a_o of oxygen.

Thus, the equations (2.11) and (2.12) we may rewrite upon expressing the activities a_A and a_B of the metals in scale by a_o and activities of oxides

$$\dot{J}_{A(eq)} = - \frac{D_A(1-\xi)}{V_{eq}} \left(\frac{\partial \ln a_A(o)}{\partial \xi} \frac{\partial \xi}{\partial x} - \frac{Z_A}{Z_o} \frac{\partial \ln a_o}{\partial x} \right) \tag{2.13}$$

$$\dot{J}_{B(eq)} = - \frac{D_B \xi}{V_{eq}} \left(\frac{\partial \ln a_{B(o)}}{\partial \xi} \frac{\partial \xi}{\partial x} - \frac{Z_A}{Z_o} \frac{\partial \ln a_o}{\partial x} \right) \tag{2.14}$$

Since the rate of scaling is supposed to be controlled by diffusion, the rate of thickening of the scale is presumed to be inversely proportional to the instantaneous thickness x_S,

$$\frac{dx_S}{dt} = \frac{k}{x_S} \tag{2.15}$$

Integration of (2.15) yields the parabolic rate law in accord with Tamman[15]

$$x_S = (2kt)^{1/2} \tag{2.16}$$

With equation

$$(\dot{J}_{A(eq)} + \dot{J}_{B(eq)}) V_{eq} = \frac{dx_S}{dt} \tag{2.17}$$

by substitution of dimensionless variable of distance

$$y = x/x_S \tag{2.18}$$

equations (2.13, 14, 16, 17, 18) yield

$$D_A(1-\xi) \left(- \frac{\partial \ln a_{A(o)}}{\partial \xi} \frac{d\xi}{dy} + \frac{Z_A}{Z_o} \frac{d \ln a_o}{dy} \right)$$

$$+ D_B \xi \left(- \frac{\partial \ln a_{B(o)}}{\partial \xi} \frac{\partial \xi}{\partial y} - \frac{Z_B}{Z_o} \frac{d \ln a_o}{dy} \right) = k \tag{2.19}$$

Three additional independent equations are needed in order to solve this problem analytically if k is known. Utilizing Fick's second law and equations (2.14) and (2.18) we can derive a second independent equation which is the rate of concentration change in scale

$$y\ k\ \frac{d\xi}{dy} = -\frac{d}{dy}\left[D_B\ \xi\left(\frac{\partial \ln a_{B(o)}}{\partial \xi}\ \frac{d\xi}{dy} - \frac{Z_B}{Z_o}\ \frac{d \ln a_o}{dy}\right)\right] \tag{2.20}$$

Similarly it is possible to derive the expression for the rate of concentration change in the alloy by substituting

$$\mu = \lambda t^{1/2} \tag{2.21}$$

where λ - dimensionless variable of distance.

μ - distance from the initial surface of alloy in inward direction.

and using Fick's second law

$$\frac{1}{2}\ \lambda\ \frac{dN_B}{d\lambda} = -\frac{d}{d\lambda}\left[D_{AB}\ \frac{dN_B}{d\lambda}\right] \text{at } \lambda > \mu_S/t^{1/2} \tag{2.22}$$

which is the third independent equation,

where

N_B - mole fraction of B in alloy

D_{AB} - interdiffusion coefficient in alloy.

In order to calculate ξ and a_o as a function of y and, N_B as a function of μ from the ordinary differential equations of second order (2.20) and (2.22) five additional conditions are needed which include the composition of the alloy, the thermodynamics of the ternary A-B-O

system which give equilibrium compositions at the allov-scale interface, and the activity of O at the outer interface. The fifth condition is also the fourth and the last independent equation needed to solve the problem. Formulation of the material balance at the alloy - scale interface yields the equation

$$Z_B N_B' \left(\frac{1-\xi_{av}}{Z_A} + \frac{\xi_{av}}{Z_B}\right) + \frac{2^{\frac{1}{2}} Z_B D_{AB} V_{eq}}{V_m k^{1/2}} \left(\frac{dN_B}{dx}\right) = \lambda = \mu_S / t^{1/2}$$

$$= - \left[\frac{D_B \xi}{k} \left(\frac{\partial \ln a_{B(o)}}{\partial \xi} \cdot \frac{a\xi}{dy} - \frac{Z_B}{Z_o} \frac{d \ln a_o}{dy}\right)\right]_{y=o} \qquad (2.23)$$

where $\xi_{av} = \int_o^1 \xi \, dy$ and N_B' is mole fraction of B is alloy. (2.24)

If the parabolic rate constant k, which appears as a parameter in equations (2.19), (2.20) and (2.23), is not known the additional independent relation is needed. This could be obtained from the material balance for B at the outer interface.

$$\dot{J}_{B(eq)} \; (x = x_S) = \frac{\xi'' \, dx_S}{V_{eq} \, dt} \qquad (2.25)$$

where ξ'' is the outside composition of the oxide scale.

Substitution of equation $x = y \, x_S$ in (2.14) and equation (2.17) in (2.25) yields

$$- \left[D_B \xi \left(\frac{\partial \ln a_{B(o)}}{\partial \xi} \frac{d\xi}{dy} - \frac{Z_B}{Z_o} \frac{d \ln a_o}{dy}\right)\right]_{y=1} = \xi'' k \qquad (2.26)$$

The solution of all five equations with necessary auxiliary functions even with the help of modern computors is a tremendous task. Consequently, one may try to obtain results for special cases which permit introduction of appropriate simplifications.

2.3.3 Variation of Defect Concentration in Mixed Oxides Forming Continuous Ideal Solid Solutions [42]

Suppose that AO and BO at elevated temperatures existing in equilibria with an oxidizing atmosphere are metal deficit oxides corresponding to formulae of the type $Me_{1-\delta}O$ due to vacancies in the cation lattice. The anion lattice is supposed to be almost perfect. In addition, an equivalent number of defect electrons must be introduced in order to maintain electrical neutrality. Since the elements Fe and Mn may have +2 or +3 valences, the defect electrons are located at cations corresponding to the number of trivalent cations formed. The formation of defects proceed by reaction of oxide with oxygen

$$\frac{1}{2}\,O_2(\text{gas}) + A^{+2}\ (\text{lattice position}) \rightarrow$$

$$O^{2-}(\text{lattice position}) + \text{cation vacancy} + 2A^{+3}(\text{lattice position}) \qquad (2.27)$$

Substitution of bivalent cations A^{+2} with foreign cations B^{+2} does not change the electrical neutrality of the crystal. If the energetic barrier for formation of B^{+3} from B^{+2} is greater than for formation of A^{+3} from A^{+2}, the number of bivalent cations taking part in the above reaction is decreased. The equilibrium of reaction (2.27) will be shifted to the left with increasing concentration of B^{+2} cations. When the partial enthalpy

and entropy of vacancies are dependent on the type of neighboring cations, the concentration of vacancies is also a function of the B^{+2} concentration.

Certain systems like CaO-MnO, Co-FeO, CoO-NiO, CoO-MgO, NiO-MgO, NiO-MnO, FeO-MgO, FeO-MnO do not show any pronounced deviations from ideality and it is possible to consider them as ideal solid solutions where Rault's or at least Henry's law is valid.

The equilibrium constant for equation (2.27) could be written as

$$k_1 = \frac{(x_A^{+3})^2 \, x_{\square}}{(x_A^{+2})^2 \, P_{O_2}^{\frac{1}{2}}} \tag{2.28}$$

x - molar concentrations.

The corresponding relation could be written for reaction of B^{+2} cations with oxygen

$$k_2 = \frac{(x_B^{+3})^2 \, x_{\square}}{(x_A^{+2})^2 \, P_{O_2}^{\frac{1}{2}}} \tag{2.29}$$

The molar fraction of electron holes may be written

$$x_{\oplus} = x_{A^{+3}} + x_{B^{+3}} = \frac{x_A^{+2} . k_1^{\frac{1}{2}} . P_{O_2}^{\frac{1}{4}}}{x_{\square}^{\frac{1}{2}}} + \frac{x_B^{+2} . k_2^{\frac{1}{2}} P_{O_2}^{\frac{1}{4}}}{x_{\square}^{\frac{1}{2}}} \tag{2.30}$$

For negligible concentrations of defects,

$$x_A^{+2} = x_{Ao} - x_A^{+3} \approx x_{Ao} \tag{2.31}$$

$$x_{B}^{+2} = x_{BO} - x_{B}^{+3} \approx x_{BO} \tag{2.32}$$

and

$$x_{A}^{+2} + x_{B}^{+2} = x_{AO} + x_{BO} \approx 1 \tag{2.33}$$

From the condition of neutrality

$$\delta = x_{\square} = \frac{1}{2} x_{\oplus} \tag{2.34}$$

and substitution in equation (2.30) yields

$$x_{\oplus} = 2^{1/3} P_{O_2}^{1/6} (x_{AO} k_1^{1/2} + x_{BO} k_2^{1/2})^{2/3} \tag{2.35}$$

The equilibrium constants are dependent on the concentration ratio of each oxide in the solid solution. If $k_2 << k_1$, we can k_2 neglect and write

$$x_{\oplus} = x_{A}^{+3} = 2^{1/3} P_{O_2}^{1/6} x_{AO}^{2/3} k_1^{1/3} \tag{2.36}$$

from equation (2.35). Equation (2.35) and (2.36) are useful since they may be used to calculate the concentration of defects in a binary solid solution oxide.

CHAPTER III

PRINCIPLES OF OXIDATION IN CO_2-CO ATMOSPHERES

3.1 Oxidation of Iron

3.1.1 Thermodynamics

The possible reactions between iron and CO_2-CO atmospheres are discussed with the help of a thermodynamic diagram. Fig. 3.1 shows such a diagram of the Fe-O system superimposed on that of the C-O system. The data were taken from Elliott and Gleiser[18]. The ordinate of the diagram represents the chemical potential of oxygen, $\Delta G° = -RT \ln P_{O_2}$, and the abscissa gives the temperature, T. Lines 1 to 3 represent the equilibrium between two condensed phases of the Fe-O system and divide the T-ΔG diagram plane into several regions in any one of which a specified condensed phase is most stable. Line 4 gives the equilibrium between carbon and carbon dioxide at 1 atm pressure. Line 5 represents the equilibrium between carbon and CO. Line denoted by 6, shows the equilibrium between CO_2 and CO. Lines 4, 5, and 6 divide the T-ΔG° plane into three regions. In the regions where the chemical potential of oxygen is low, carbon is the most stable species. At temperatures above the triple point, CO is the most predominant component in the gas phase. From the diagram we can see that at 1000°C, which is in our interest FeO, exists only in a narrow region of CO_2/CO ratios. The upper limit of FeO existence is the CO_2/CO ratio approximately 8 and at the lower limit the ratio is approximately 0.33.

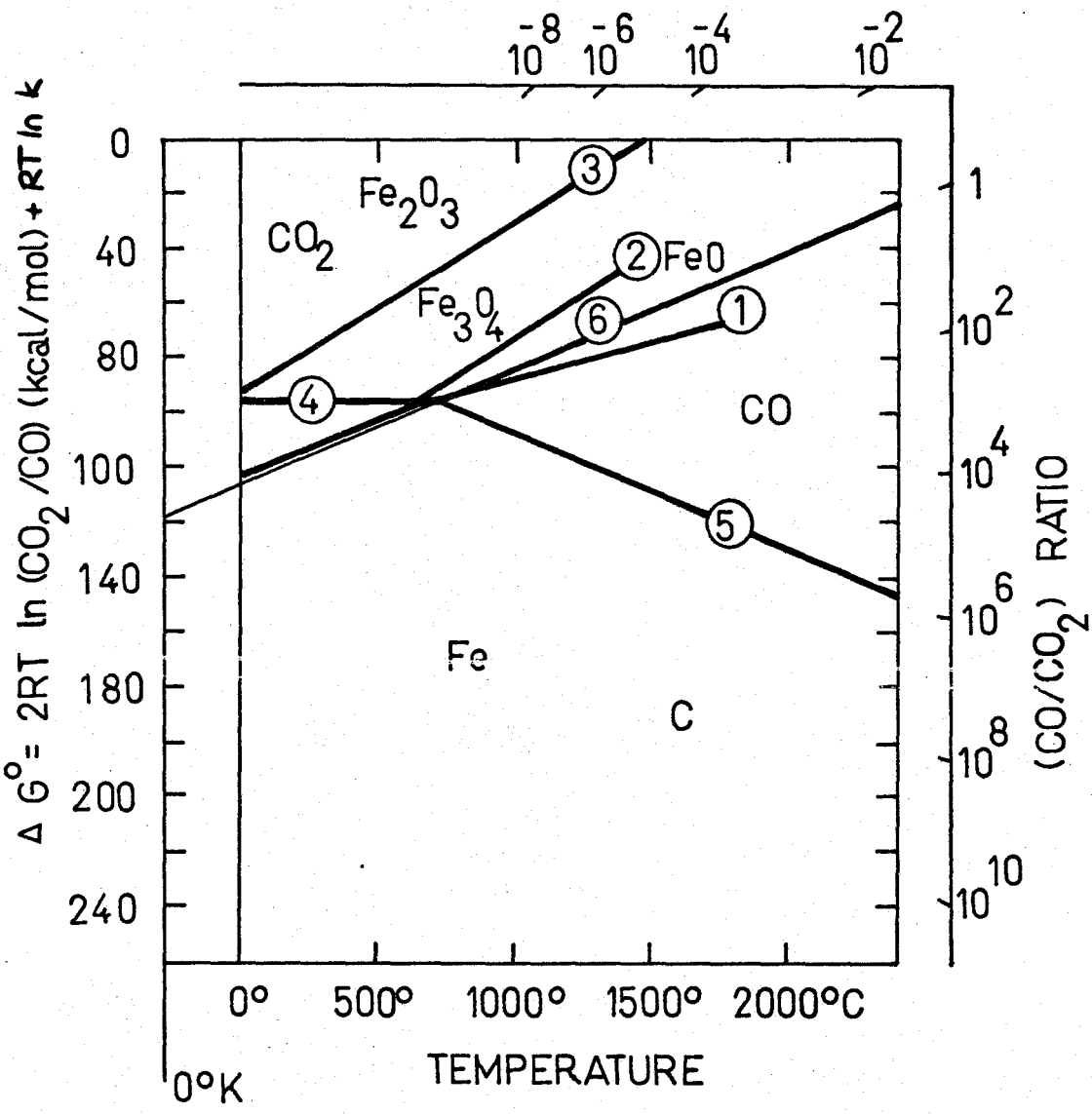

Figure 3.1 Standard Free Energy of Formation for Oxides of Iron and Corresponding Equilibrium Ratio of CO_2 and CO as a Function of Temperature.

Above the ratio of 8 there is formation of Fe_3O_4 and possibly even Fe_2O_3. Below the lower limit there should not be any oxide formation. Between the limits the reaction is

$$Fe + CO_2 \rightarrow FeO + CO \tag{3.1}$$

3.1.2 Properties and Structure of FeO

Wustite[17] is a metal deficit semiconductor with the lattice disorder being cation vacancies. Using the common notation, the dissolution of oxygen into wustite using CO_2-CO atmospheres is represented by

$$CO_2\ (g) \rightleftarrows CO(g) + O_\ell + Fe^{k}_{\square}{}'' + k\oplus \tag{3.2}$$

Applying the law of mass action and assuming a dilute solution of defects in the wustite yields

$$k_1 = [C^{k}_{\square}] \times [C_{\oplus}]^{k}\ P_{CO}/P_{CO_2} \tag{3.3}$$

where the C denotes concentrations. Furthermore, when k = 2 the cation vacancies are completely ionized, and both the concentration of cation vacancies and concentration of electron holes are proportional to the third root of the ratio, P_{CO_2}/P_{CO}. This analysis is valid for one particular model based on an ideal solution at elevated temperatures ($t \geq 1000°C$)[18]. At lower temperatures, it has been shown[18] that the pressure dependence of the electronic conductivity changes in a manner which suggests that vacancies interact with or "trap" electron holes.

Recently an attempt has been made by Kofstad and Hed[19] to

correlate the experimental data of Vallet and Raccah[20] on the deviation from stoichiometry of wustite on the basis of a defect structure model involving complex defects.

Neutron diffraction studies have suggested that for each vacancy which is formed in $Fe_{1-\delta}O$, an equal number of iron Frenkel defect pairs are formed in the metal lattice[51]. Each defect may on this basis be considered as a complex defect consisting of two iron vacancies associated with an interstitial atom. Such a complex defect also results in the same local structure configuration as found in Fe_3O_4. It is also noteworthy that the heat of formation of the defects in $Fe_{1-\delta}O$ is negative, i.e., the deviation from stoichiometry at a given oxygen pressure increases with decreasing temperature. In oxides with single, unassociated vacancies the heat of formation is commonly positive[52], and the negative value found for $Fe_{1-\delta}O$ thus serves as a further indication that defects in this oxide are complex. From these facts it was concluded[19] that it is highly unlikely that the defects are doubly charged vacancies. Hence, the complex defect was assumed to be composed of two iron vacancies on octahedral sites and on iron interstitial on a tetrahedral site. This complex may be neutral or singly charged. The equation for the formation of these defects may be written as

$$Fe^{+2} + V_i + \frac{1}{2} O_2 \rightarrow Fe_C^{\,x} + O_o \qquad (3.4)$$

and

$$Fe^{+2} + Fe_C^{\,x} \rightarrow Fe_C^{\,\prime} + Fe^{+3} \qquad (3.5)$$

where Fe_C^x and $Fe_C^{\,\prime}$ are neutral and singly ionized complex defects,

respectively. V_i represents an interstitial (tetrahedral) site, Fe^{+2} divalent and Fe^{+3} iron cation on normal (octahedral) site and O_o on oxygen lattice site. The calculated nonstoichiometry of $Fe_{1-\delta}$ using equations (3.4) and (3.5) show very good agreement with experimental data of Vallet and Raccah[20]. Calculated values of nonstoichiometry using singly charged defects model correspond very closely with experimental data at high temperatures (1000°C) which suggests, that degree of ionization of neutral defects is very high. This model enables one to calculate the concentration of free charge carriers and therefore the electrical conductivity and Seebeck coefficient. As was shown[21], however a straightforward calculation does not yield the observed experimental values obtained for the electrical conductivity.

Vallet and Raccah[20] and Kleman[22] have proposed that their thermogravimetric data and high temperature X-ray studies of $Fe_{1-x}O$ may be explained only by assuming three different phases in the wustite homogeneity range. In a recent publication, Feuder and Riley[23] suggest that the high temperature electrolytic cell studies supports the existence of three different phases in wustite. It has been proposed that the occurrence of different phases are due to differences in ordering of the defects. The identification of these phases is, however, still an open question and is based on the fact that plots of emf values vs temperature at constant composition consists of three linear regions. Rizzo et al.[24] have made similar measurements and have found a simple nonlinear relation over the whole range. The problem can be reduced simply to the question of whether these data are best fitted by three different straight lines with different slopes or a single continuous curve.

3.1.3 Mechanisms and Kinetics of Iron Oxidation

In view of the fact that this work is concerned with oxidation studies when only one oxide phase is formed, the oxidation of iron will be discussed under conditions where wustite is formed as the only oxidation product. The thermodynamic relations of the two systems Fe-O and CO_2-CO have been previously discussed.

Hauffe and Pfeiffer[25] observed linear oxidation rates with iron in CO_2-CO atmospheres at 900°-1000°C, indicating that the rate-controlling step was not diffusion through the oxide, but instead a phase-boundary reaction. However, the oxidation rate was found to be a function of the CO_2/CO ratio. If the interface reaction was rate determining, the oxidation rate should be independent of pressure. This led authors to suggest that the rate-controlling reaction is chemisorption of oxygen produced at the wustite surface by decomposition of CO_2. Smeltzer[26] found that oxidation kinetics of iron in CO_2 in the temperature range 600°- 1100°C were linear, transforming to parabolic at longer times. The following reaction mechanisms were proposed.

$$CO_2 \rightarrow O_{ads} + 2\oplus_{(o)} + CO \qquad (3.6)$$

$$O_{ads} \rightarrow FeO + Fe^{++}\square_{(o)} \qquad (3.7)$$

$$Fe^{++}\square_{(o)} + 2\oplus_{(o)} \rightarrow Fe^{++}\square_{(i)} + 2\oplus_{(i)} \qquad (3.8)$$

$$Fe + Fe^{++}\square_{(i)} + 2\oplus_{(i)} \rightarrow Nil \qquad (3.9)$$

$$O_{ads} + 2\oplus_{(o)} \rightarrow \frac{1}{2} O_2 \qquad (3.10)$$

Subscripts (o) and (i) refer to the oxide-gas interface and the metal-oxide interface respectively. "Nil" refers to annulment of lattice defects by solution of iron into the oxide.

If diffusion of iron vacancies across the oxide scale is the rate-controlling step, reaction 3.8, then a parabolic oxidation rate would be observed. Since linear kinetics are observed in the early stages of the reaction, the rate determining step could be chemisorption or incorporatiion of adsorbed oxygen into the wustite lattice. By assuming that the surface coverage of adsorbed oxygen remained constant, and that lattice defects in the oxide were in equilibrium with the metal, Smeltzer[26] derived an expression for the dependence of the linear rate constant, k_L on CO_2 partial pressure

$$k_L = \text{constant } (P_{CO_2} - P_{CO_2}^{*}) \qquad (3.11)$$

where $P_{CO_2}^{*}$ is the partial pressure of CO_2 over wustite equilibrated with iron.

Nearly simultaneously, Pettit, Yinger and Wagner[27] derived a similar expression assuming that chemisorption was the rate-determining step. They also found that k_L is directly proportional to P, the sum of partial pressures of CO_2 and CO. Linear oxidation rates were observed up to an oxide thickness of 10^{-2} cm., and parabolic rates for thicker scales. In a later paper, Pettit and Wagner[28] presented a theory describing the transition from linear to parabolic kinetics, which agreed well with their experimental observations. In more recent publications Turkdogan et al.[29] and Morris and Smeltzer[30] have advanced the mechanisms for linear oxidation based upon the surface steps for dissociation

of the triatomic reactant and incorporation of the resulting adsorbed oxygen into the oxide. They have demonstrated from the detailed balance of reaction steps that the linear oxidation rate constant can be expressed as,

$$k_L = k_1\theta_V \left(1 - \frac{a_o^*}{a_o^{(g)}}\right) P_{CO_2} = k_1\theta_V (1 + k)(P_{CO_2} - P_{CO_2}^*) \qquad (3.12)$$

where k_1 is the rate constant for dissociation of carbon dioxide, θ_V is the fraction of surface devoid of adsorbed oxygen, a_o^* and $a_o^{(g)}$ are the corresponding oxygen activities corresponding to the partial pressures of carbon dioxide and k is the equilibrium constant for formation of wustite.

3.2 Oxidation of Manganese

3.2.1 Thermodynamics

The possible reactions between manganese and CO_2-CO atmospheres are discussed with the help of a thermodynamic diagram. Figure 3.2 shows such a diagram[31,32] of the MnO system superimposed on that of the C-O system. The data were taken from Elliot and Gleiser[16]. The ordinate of the diagram represents the chemical potential of oxygen, $\Delta G° = -RT \ln P_{O_2}$, and the abscissa gives the temperature T. Lines 1 to 2 represent the equilibria between condensed phases of the Mn-O system and divide the T - $\Delta G°$ plane into several regions in any one of which a specified condensed phase is most stable. Line 3 gives the equilibrium between carbon and carbon dioxide at 1 atm. The line denoted 4 gives the equilibrium between carbon and carbon monoxide. Similarly the line denoted 5, shows the equilibria between CO_2 and CO at specified ratios of CO_2 to CO.

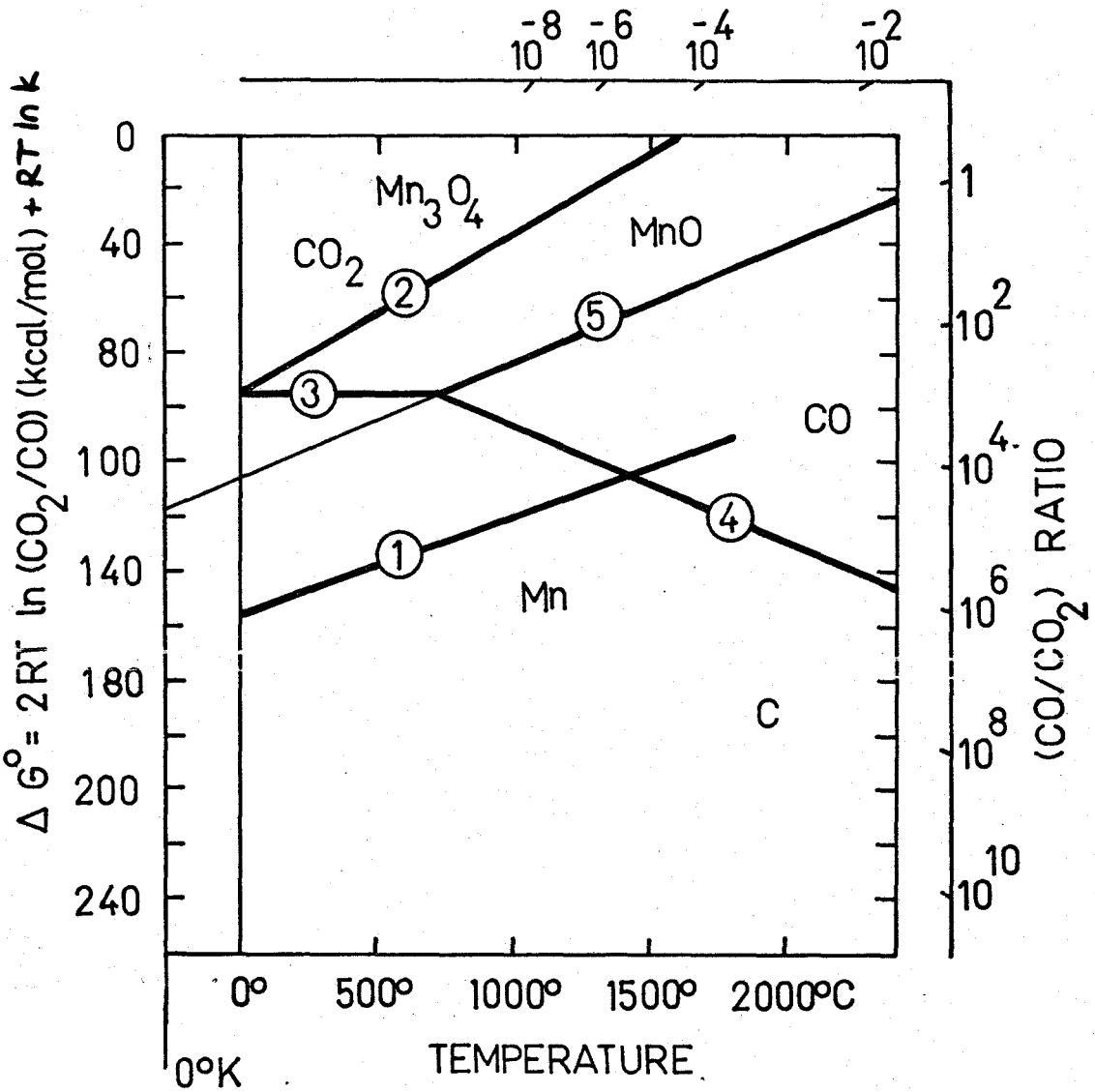

Figure 3.2 Standard Free Energy of Formation for Oxides of Manganese and Corresponding Equilibrium Ration of CO_2 and CO as a Function of Temperature.

Lines 3, 4 and 5 divide the T - ΔG° plane into three regions. In a region where the chemical potential of oxygen is high, carbon dioxide is most predominant. In a region where the chemical potential of oxygen is low carbon is the most stable species. At temperatures above the triple point, carbon monoxide is the most predominant gas phase. It is seen that manganeous oxide is the only oxide formed in CO_2-CO atmospheres by the reaction

$$Mn + CO_2 \rightarrow MnO + CO \qquad (3.13)$$

which only takes place at 1000°C. As we alter the temperature, other possibilities could occur[33].

3.2.2 Properties and Structure of MnO

One would expect the non-stoichiometry of manganeous oxide to resemble that of ferrous oxide. The structures of the two oxides are very similar, and they form a complete series of solid solutions with each other, the activity coefficients being ideal (at least to within 10%) over the whole composition range[34]. It is reasonable therefore to attribute the metal deficit to cation vacancies in the lattice. But MnO is different from FeO in that the departures from stoichiometry are considerably smaller [35]. The thermodynamic properties also show substantial differences.

Cation vacancies could be created in MnO mainly by mechanisms

$$\frac{1}{2} O_2 \rightleftarrows Mn_{\square}'' + 2\oplus + MnO \qquad (3.14)$$

where $Mn_{\square}''$ is a cation vacancy and $\oplus$ is an electron hole.

At very low oxygen potentials mainly by Frenkel mechanisms

$$Ni\ 11 \rightleftarrows Mn_{\square}'' + Mn_i \ldots \quad (3.15)$$

or by a Schottky mechanisms

$$Ni\ 11 \rightleftarrows Mn_{\square}'' + O_{\square}\cdot\cdot \quad (3.16)$$

where the symbols $Mn_i\ldots$ and $O_{\square}\ldots$ denote an interstitial manganeous ion and oxygen ion vacancy, respectively.

Davies and Richardson[35] have found that manganese oxide at 1500°-1650°C has a composition from $MnO_{1.000}$ to $MnO_{1.045}$. The electrical conductivity of MnO has been measured by Eror and Wagner[36] in the temperature range of 900°-1150°C in CO_2-CO gas mixtures. The transition of n-type to p-type conduction was found to occur near the CO_2-CO ratio of 1:1. They also found that above the ratio of 10:1, a $P_{O_2}^{1/6}$ dependence was followed, while a $P_{O_2}^{-1/6}$ dependence of the conductivity was obeyed below the ratio of 1:10.

3.2.3 Mechanisms and Kinetics of Manganese Oxidation

The oxidation properties of electrolytic Mn in CO_2-CO atmospheres were investigated by Fueki et al.[33] at 1000°C. They found that the oxidation of manganese in CO_2-CO mixtures is controlled by the outward diffusion of manganeous ions through a single layer of MnO. The dependence of the parabolic constant on the ratio of P_{CO_2}/P_{CO} is approximately linear and the slopes are 1/3 which corresponds to 1/6 for $k_p \propto P_{O_2}$ relationship. The oxidation studies are consistent with those of Eror and Wagner[36] in the p-type region of MnO. Marker studies confirmed the

mechanism in which the movement of manganous ions play the major role of material transport in the oxide under conditons reported above.

The value of the self diffusion coefficient of manganous ions was independent of P_{CO_2}/P_{CO} in the region, where the value of log P_{CO_2}/P_{CO} is less than zero. The independence was explained by a mechanism whereby intrinsic defects, Frenkel and Schottky, are more prevalent, than those formed by the introduction of oxygen into the lattice according to Eq. (3.12). In the region where the value for the logarithms of the gas ratio was larger than zero, the dependence of the value of the self diffusion coefficient on P_{CO_2}/P_{CO} was 1/3.7 to 1/3.0. This dependence could be explained by the creation of one cation vacancy and two electron holes for each incorporated oxygen atom according to Eq. (3.14).

3.3 Oxidation of Fe-Mn Alloys

3.3.1 Thermodynamics

The possible reactions between Fe-Mn alloys and CO_2-CO mixtures is very difficult to estimate, because of lack of thermodynamic and constitutional data. However, some data in limited ranges of oxygen potentials are available. Foster and Welch[34] determined the equilibrium oxygen pressures (at 850°, 1000° and 1150°C) for reduction of solid solutions of ferrous oxide and manganous oxide to metal. Comparison of experimental oxygen pressure data with calculated values shows that the oxide solid solution is thermodynamically ideal over its whole range of composition. The results shown in Fig. 3.3 specify the lower limit of stability for FeO-MnO solid solutions. Similar values for equilibrium of FeO-MnO solid solution with

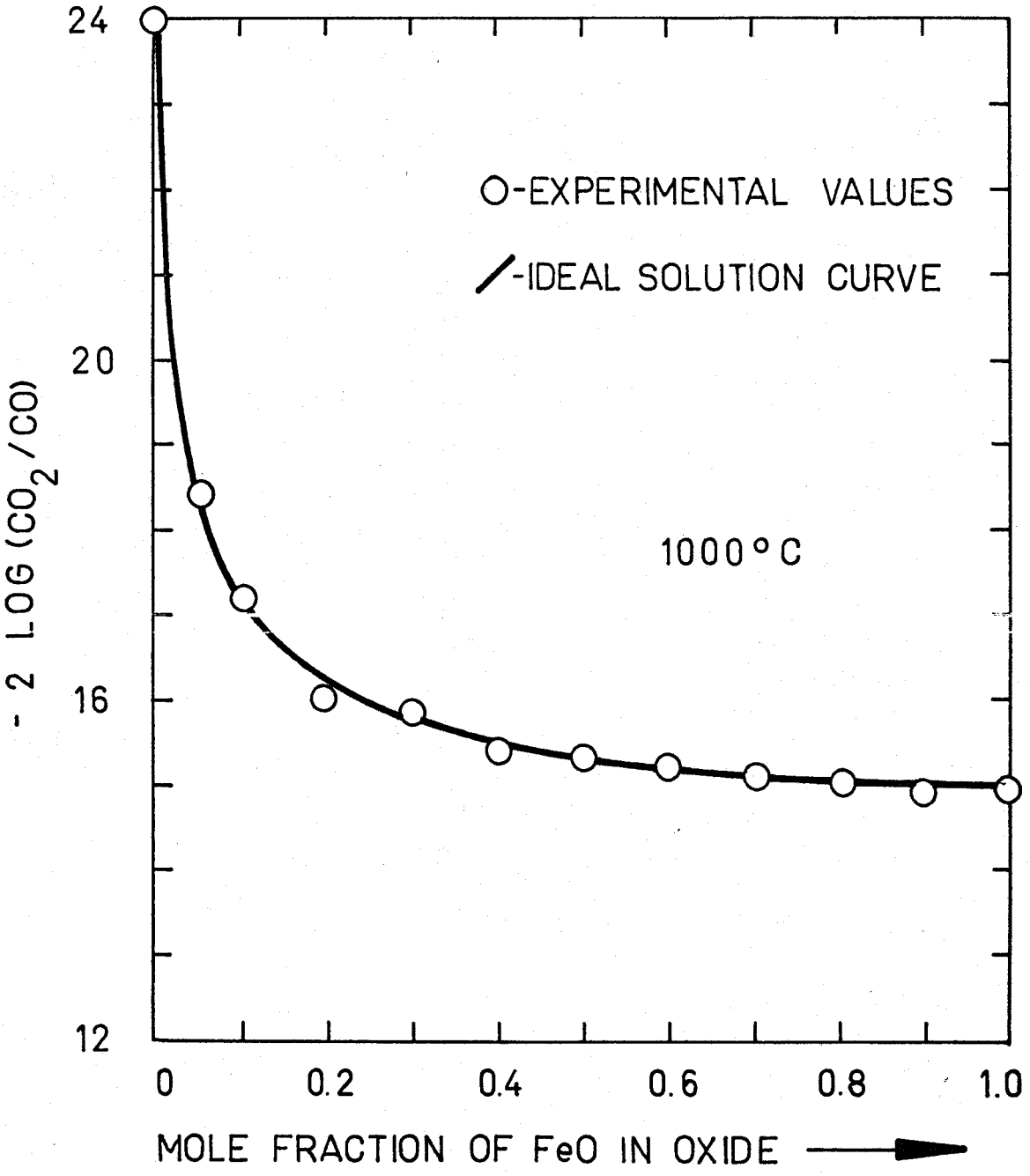

Figure 3.3 The Equilibrium Oxygen Potential (2 log CO_2/CO) as a Function of FeO Content in FeO-MnO Solid Solution in Equilibrium with Fe-Mn Alloy.

Fe_3O_4, Mn_3O_4, their solution or spinels are not available. However, recent experiments show[37] that Mn has a stabilizing effect on FeO and increases the oxidation rate of Fe-Mn alloys. These facts were used in designing our experiments. The aim was to obtain a single phase scale consisting only of an FeO-MnO solid solution.

The FeO-MnO solid solution has been examined by a number of investigators. The measurements by Foster and Welch[34] show that the FeO-MnO system at 1000°C form a homogeneous solid solution obeying Vegard's law within the experimental error of the employed X-ray technique. Hay, Howatt and White[38] claim formation of an ordered structure due to a miscibility gap which could occur at 1000°C, but at the present time there is no experimental evidence to confirm this assertion.

Thermodynamic properties of FeO-MnO solid solutions have been the subject of numerous investigations. Foster and Welch[39] found this system having properties of an ideal solid solution. The thermodynamic deviations from ideality were negligible. Driessens[40] explains the small positive thermodynamic deviations from ideality of the system by coulombic interactions between the cations. Upon summarizing all the experimental results, it is possible to consider the system as an ideal solid solution to a first approximation.

3.3.2 Properties and Structure of FeO-MnO Solid Solutions

Both wustite[17] and MnO[33] are metal deficit semiconductors with the lattice disorder being cation vacancies and positive holes. There is strong evidence[41] to believe that this structure is conserved in the solid solution of both oxides. As in aqueous solutions, the tendency

of iron to become trivalent in solid solutions of oxides is more pronounced than of manganese. The measure of this tendency is the equilibrium oxygen pressure between MeO and Me_3O_4. For a solid solution of FeO and MnO, positive holes will therefore be concentrated on iron cations. Manganese cations, on the other hand, are only present in the bivalent state. For the solid solution, we can write the following equations.

$$3\ Fe^{2+} + \frac{1}{2}\ O_2 \rightarrow Me^{+2}_{\square} + 2\ Fe^{+3} + FeO \tag{3.17}$$

and

$$2\ Fe^{2+} + Mn^{+2} + \frac{1}{2}\ O_2 \rightarrow Me^{+2}_{\square} + 2\ Fe^{3+} + MnO \tag{3.18}$$

Utilizing the law of mass action, we can write

$$\frac{y^3}{x^2\sqrt{P_{O_2}}} = k' \tag{3.19}$$

where $y = n_{\square}/(n_{\square} + n_{Me^{+2}})$, is the molar fraction of vacancies, k' is the equilibrium constant and x is the concentrations of Fe cations. From (3.18) the concentration of defects is [41]

$$y = x^{2/3} \cdot P_{O_2}^{1/6} \cdot k'^{1/3} \tag{3.20}$$

which is equivalent to Eq. (2.36) from the general analysis given by Zintl[42].

The experimental results obtained by Engell and Kohl [41] for FeO-MnO solid solutions are not in good agreement with the theoretically calculated defect concentrations for particular conditions. The measured

values of vacancy concentrations at 1250°C illustrated in Fig. 3.4 show noticeable deviations from the theoretical curves. The general variation of increased vacancy concentration with increasing oxygen activity is similar, but the reason for the deviations are unknown. It would appear that corrections must lie inside the simple assumptions for the solution behavior of the metal vacancies.

3.3.3 Oxidation of Fe-Mn Alloys

To the present, work has not been reported in the literature on the oxidation of Fe-Mn alloys in CO_2-CO atmospheres. Existing work has been carried out on the oxidation properties of the Fe-Mn alloys in oxygen and on exclusive internal oxidation in H_2O-H_2 atmospheres[43].

Owing to the similarity of chemical properties of iron and manganese, there is little change with composition in the oxidation properties of Fe-Mn alloys in oxygen[44]. The weight changes or lifetimes on oxidation of alloys containing 0 - 4% Mn increase or decrease slightly with concentration depending on temperature[45,46], the diffusion rates of iron and manganese ions in the FeO-MnO and Fe_3O_4-Mn_3O_4 solid solutions being apparently similar[44]. Manganese is found in approximately equal proportions in the oxide layers and in the bulk alloys[45,47,48]. Kubashewski and Hopkins[49] conclude that manganese additions to iron and steel have negligible effect on the oxidation behaviour. However, manganese can negate the beneficial effects ordinarily introduced by the alloying elements that eliminate or retard wustite growth[50] by stabilizing it.

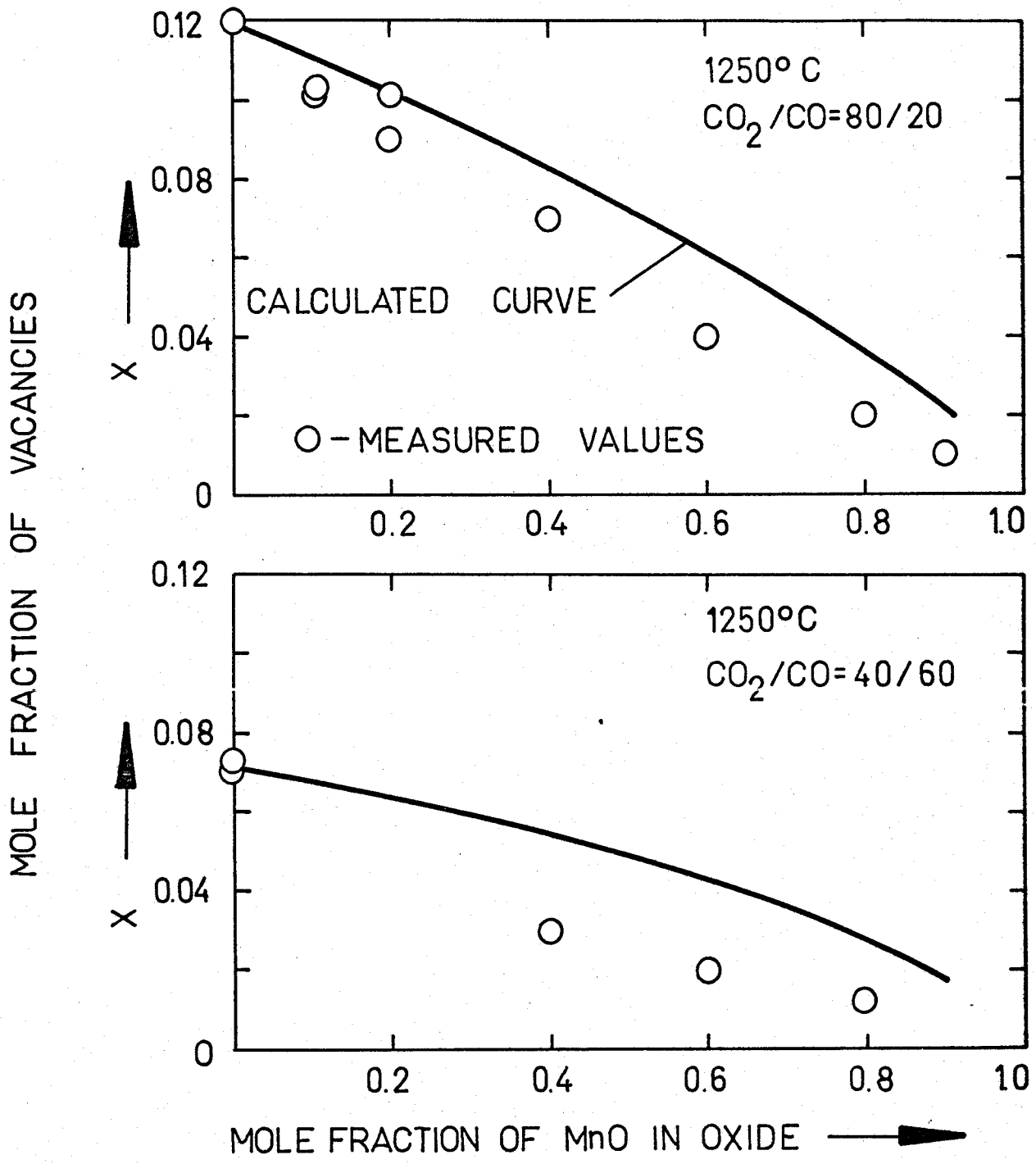

Figure 3.4 Concentration of Vacancies as a Function of MnO Content in the Oxide.

CHAPTER IV

EXPERIMENTAL TECHNIQUES

4.1 Introduction

In order to determine the reaction kinetics in the investigations on metal oxidation, various experimental techniques are used. Most commonly used are the methods which measure the growth of the oxide layers. Gravimetric, volumetric, manometric and electrometric methods are the examples of simple, but very reliable experimental techniques. In this investigation the thermogravimetric method was employed for measuring the oxidation rates of rectangular samples. The samples were exposed at 1000°C to the CO_2-CO atmospheres at a total pressure of 1 atm.

4.2 Alloy and Specimen Preparation

The alloys were prepared from high purity electrolytic iron and manganese. The melting operation was carried out in a non-consumable arc furnace with a tungsten electrode operating under argon at 200 mm pressure. In order to obtain alloy samples of required size from one charge, the chips of high purity metals, previously cleaned by pickling with dilute sulphuric acid, were melted into the form of 50 gm. buttons. After cleaning with a wire brush, the buttons of each metal were accurately weighed to yield alloys containing 1, 10, 25, 35 and 50 weight per cent manganese. Approximately 300 gms. of material was placed into the melting chamber. Each charge was melted, inverted and then remelted until a total of four melting operations had been completed in order to prevent any long range

segregations. Then the product was sealed in a quartz-tube filled with argon and annealed for five days at 1000°C. The compositions of obtained alloys are given in Table 5.1.

The alloys were hot rolled at 800°C to a thickness of 4 mm. The surfaces of each sheet were cleaned by pickling in dilute hydrochloric acid and by abrasion using 600 gnt. silicon carbide grinding paper. The sheets were then cold rolled to a thickness of approximately 2.5 mm. The test specimens were then cut from the sheets as rectangular plates approximately 10 mm x 10 mm x 2mm. A hole approximately 1.0 mm was drilled in each sample in order to suspend it in the kinetic assembly. These samples were mounted in bakelite and metallographically polished on all sides through 220, 320, 400 and 600 silicon carbide grinding papers under water as lubricant. Final polishing was then carried out on selvyt cloths impregnated with 6 μ and 1 μ diamond abrasive using kerosene as lubricant. After removal from the bakelite, specimens were washed with petroleum ether and stored in acetone. Immediately before an experimental test, the specimens were dried, weighed and the surface area was obtained by measuring the specimen dimensions with a micrometer.

4.3 Oxidation Apparatus

Essentially the experimental assembly was comprised of three parts: reaction gas supply system, reaction chamber with a suspension device for specimens and a continuous recording semiautomatic microbalance. The schematic diagram in Fig. 4.1 represents an overall picture of the basic components of the assembly. The numbers in the brackets in the following text

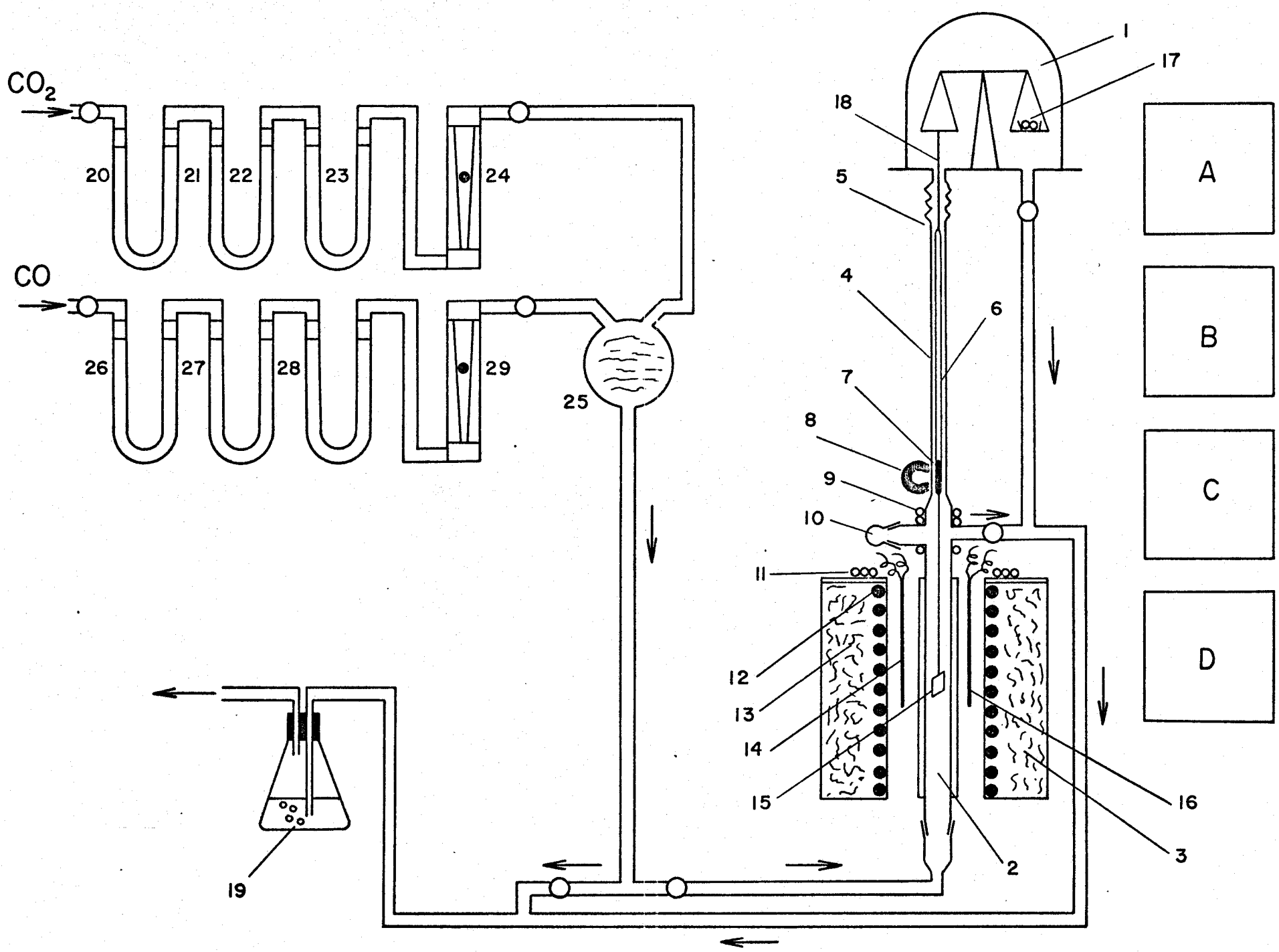

Figure 4.1 Schema of Experimental Assembly.

represent the corresponding parts of the experimental apparatus.

The gas supply system provided flowing atmospheres utilized for oxidation tests. For almost all experiments, the atmospheres contained CO_2 and CO. The carbon dioxide was supplied by Matheson of Canada Limited. Its purity as stated by the manufacturer was better than 99.95 vol %. CO_2 was dried by passage through columns containing silica gel (20), reduced BTS catalyst (21), magnesium perchlorate (22) and activated alumina (23). The carbon monoxide was also supplied by Matheson of Canada Limited. Its purity was minimum purity 99.5 vol %. CO was purified by passage through columns containing silica gel (26), magnesium perchlorate (27) and ascarite (28).

The gases were metered by Rotameters supplied by Matheson of Canada Limited. For measuring flow rates of CO_2 and CO tube No. 1-15-6 with stainless steel float (24) and tube No. 14-11-6 with stainless steel float (29) were used respectively. The rotameters were carefully calibrated by measuring the rate of movement of a soap bubble in a calibrated burette.

The individual gases were thoroughly mixed by means of a one-liter mixing bulb (25) filled with glass wool. The mixture then was directed to an inlet at the bottom of the oxidation tube. Flow rates of gas in the furnace tube were sufficiently rapid to prevent thermal segregation of the gases. This flow was maintained at 5 ccm/sec.

The reaction chamber was a mullite tube (2) 30 in. long and 1 5/8 in. in O.D. surrounded by furnace (3) consisting of a 20 in. Kanthal element imbedded in insulation. Power was supplied to the heating element from the 220V line through a 2500 V.A. transformer. The temperature was controlled to ± 2°C by a Philips controller. The mullite tube was fused to the glass

tube (4) by which the reaction chamber was connected to balance (1) by means of a flexible aluminum metal bellows vacuum joint (5). The fluctuation of temperature in the approximately 4 in. long zone was limited by sensitivity of the controller. The control Pt-Pt 10% Rh thermocouple for the latter (16) was placed between the mullite tube (2) and Kanthal windings (12) at the centre of the hot zone as well as the reference Pt-Pt 10% Rh thermocouple (14) at the same level. The reaction temperature was measured by means of the reference thermocouple. This thermocouple was calibrated against another Pt-Pt 10% Rh thermocouple attached to a specimen and suspended within the hot zone of the reaction chamber. Hence the actual reaction temperature could be maintained by using reference thermocouple (14).

The suspension device consisted of a Pyrex tube (6) which was closed at the top and partially open at the bottom. It was connected to a nylon fibre (18) suspended from one beam of the balance. An Armco iron core inside the tube (6) could be manipulated with a magnet from outside the assembly. The specimen was suspended in the furnace by means of platinum wire attached to the iron core. This arrangement allowed the test specimen to be raised and lowered in the furnace without any direct contact from outside. From the second beam of the balance was suspended a dish for delicate balancing (17).

The specimens were introduced and removed from the assembly through the loading inlet (10) located in the cold region above the reaction chamber.

The Ainsworth, Type RV, continuous recording semiautomatic microbalance was used to determine and record the weight change of a specimen exposed to a reaction atmosphere. The balance was capable of continuously measuring and recording weight gains up to 400 mg. The sensitivity of the

instrument was such that 0.1 mg. could be detected under the experimental conditions.

The CO_2-CO atmosphere was exhausted outside the building through controlling bubbler (19) which also served as a pressure regulator in the reaction chamber.

4.4 Oxidation Procedure

A brief description of the experimental procedure will only be given here because it is not the purpose of this section to give detailed operational instructions.

At the onset of an experimental run, the two cooling systems were turned on (air (9) and water (11)) and the ice in the cold junctions of the thermocouples was renewed. The test sample was introduced through the loading inlet opening and was suspended from the wire by a platinum hook, attached to the sample by a small hole. The inlet was then closed and the balance was adjusted to record a suitable zero point for maintenance of the correct range and sensitivity. The balance was then arrested and the specimen was raised to the upper position. The reaction chamber was flushed for 30 minutes with the CO_2-CO atmosphere. The exact composition of an atmosphere was set in this period for the experimental run. Power was then supplied to the furnace and once the temperature in the reaction chamber reached the required temperature, the sample was lowered into the hot zone and automatics (A) of the balance, weight change recorder (B) were turned on. Simultaneously the balance beam was released and the weight gains immediately recorded.

At the termination of the run, the balance was arrested and the specimen was raised rapidly into the cool upper position. The atmosphere continued to flow until the furnace was cooled below the ignition temperature of the atmosphere. The flow of gas was then turned off, the specimen was removed from the assembly and stored in the desicator for subsequent examinations and analyses.

4.5 Analytical and Examination Methods

The compositions of the alloys were determined by two methods. Mn was determined by a standard wet chemical analysis for steels. In this method, a metal sample was dissolved in H_2SO_4 (1:4) containing a few drops of HNO_3. After dissolution and addition of silver nitrate and ammonium persulfate, the manganese content was determined titrating with arsenic oxide solution. Standard steel samples from the American Bureau of Standards were used as analytical standards. The atomic absorption photometry, a modern and now commonly used way of chemical analysis, was used to check the results from the wet analyses. The metal samples, accurately weighed, were dissolved by boiling in concentrated HCl. After cooling, the solution was diluted to yield the approximate concentration acceptable for the atomic absorption photometer, model No. 303 manufactured by Perkin-Elmer Limited. The measured concentrations were recalculated to give contents of manganese in weight per cents. The manganese in oxide scales was determined volumetrically by the method due to Lang[53]. In this method, bivalent manganese is oxidized by didromate and stabilized in the tetravalent state as a metaphosphoric acid complex. The excess dichromate is removed

by addition of sodium arsenite, and the tetravalent Mn then quantitatively reduced by a standard ferrous solution, N-methyl-diphenylamine being used as indicator. Manganese sulphate monohydrate was taken as the analytical standard.

The exposed specimens were mounted vertically in araldite. This cold setting resin was found to be more suitable than bakelite which tends to cause the scale to break away from the metal. The mounting compound was very hard, which helped to reduce the surface area relief arising in polished cross sections due to various constituents of different hardness. They were polished through 220, 320, 400 and 600 silicon carbide grinding papers, with final polishing on 6 μ and 1 μ diamond-impregnated cloths. In all polishing operations only kerosene was used as lubricant which minimizes the final oxide porosity due to chipping out of the oxide. The microstructures of the specimens were examined by means of the Zeiss optical microscope.

X-ray analyses were used to determine phases and bulk compositions of oxides. Oxide was scraped off the exposed samples and ground to a fine powder. The samples were prepared by filling very fine glass capillaries powder, placed in the Debye-Scherer camera, and exposed to cobalt $K\alpha$ radiation. From so obtained radiograms, it was possible to identify the oxide phases as well as the bulk compositions of the scales. In order to detect phases, which could have formed at the surface of the scale in a small quantity, the Philips X-ray fluorescent diffractometer was used.

The concentration profiles of Fe and Mn in the scales were determined using an Acton electron probe microanalyser. Samples for these

measurements were prepared the same way as for optical examinations. It was necessary to deposit a thin layer of carbon on the surface to prevent any build up of charge on the non-conductive phases present in the sample. The operating conditions to obtain the best results for the Fe-Mn system were found to be a 15 K.V. acceleration voltage and a specimen current between 50-80 nano amperes. In order to use the microprobe for quantitative analysis, it is necessary to calibrate it for the elements of interest. The results of calibration are the diagrams of relative intensity versus the composition of phase. The relative intensity is the ratio of the X-ray intensity from a given element in alloy, minus the background intensity and the X-ray intensity from a pure element minus background. The background intensity is determined by counting with the spectrometer set a few degrees off the peak, or as in the case of Fe-Mn alloys, by setting the spectrometer for Mn and counting pure Fe. The calibration curves could be obtained by two methods: by the use of standards or theoretical calculations using all the available knowledge of the various corrections necessary. The first method was used to calibrate the probe for Fe-Mn alloys. The calibration curve was obtained from measuring the relative intensities of X-rays generated by standards containing known amounts of the elements in solid solution. The results are shown in Fig. 4.2. The second method was used to obtain the calibration curves for FeO-MnO mixtures. It was impractical to prepare separately the FeO-MnO standards; therefore, the calibration curve was obtained by theoretical calculations of various corrections. The theoretical relative intensities were calculated by the procedure due to Dalvi[54]. The computer program shown as Table 4.1 was used to speed up numerical operations. The calculated values are plotted in Fig. 4.3. These data were used for

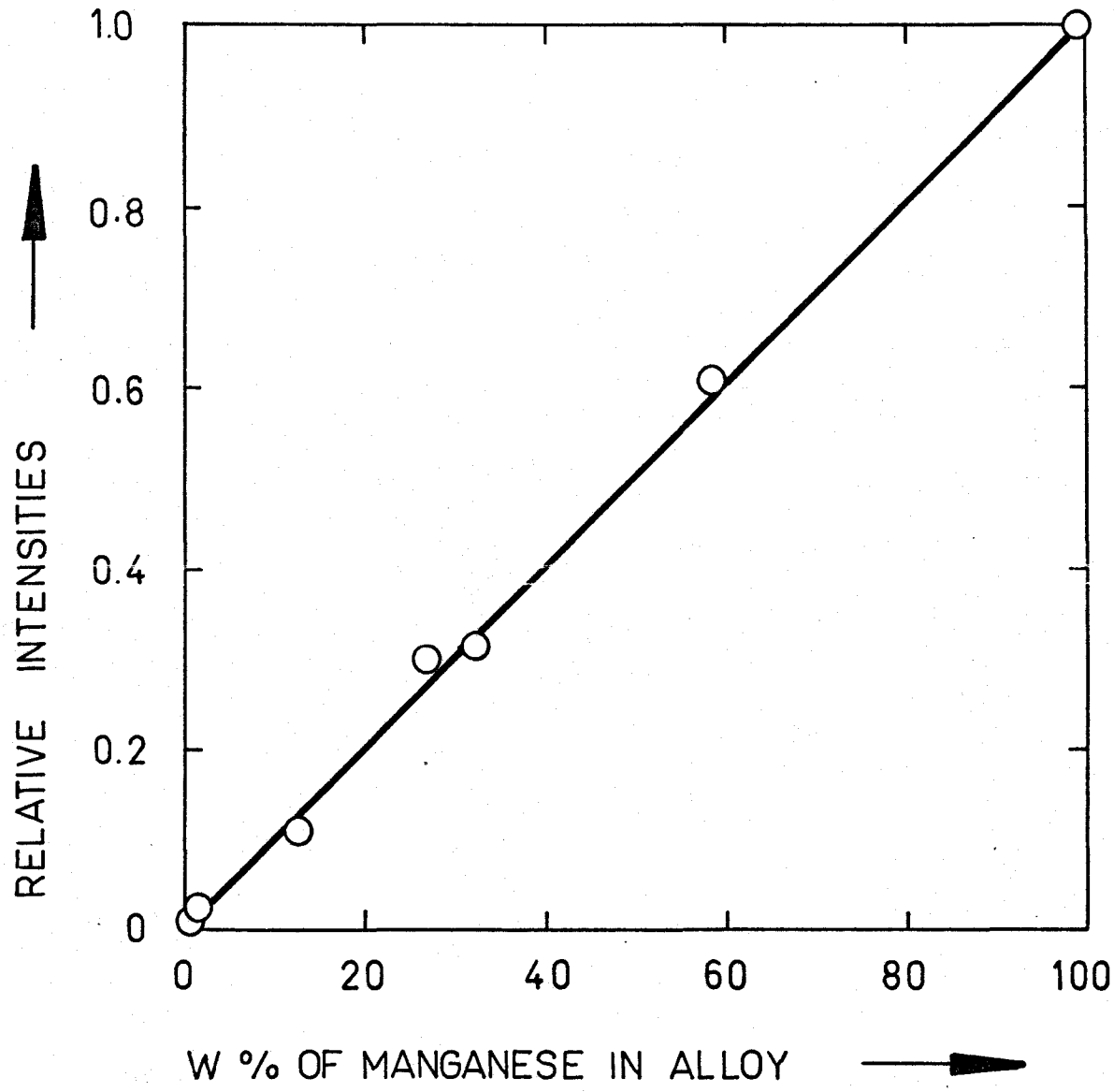

Figure 4.2 Electron Probe Calibration for Iron-Manganese Alloys.

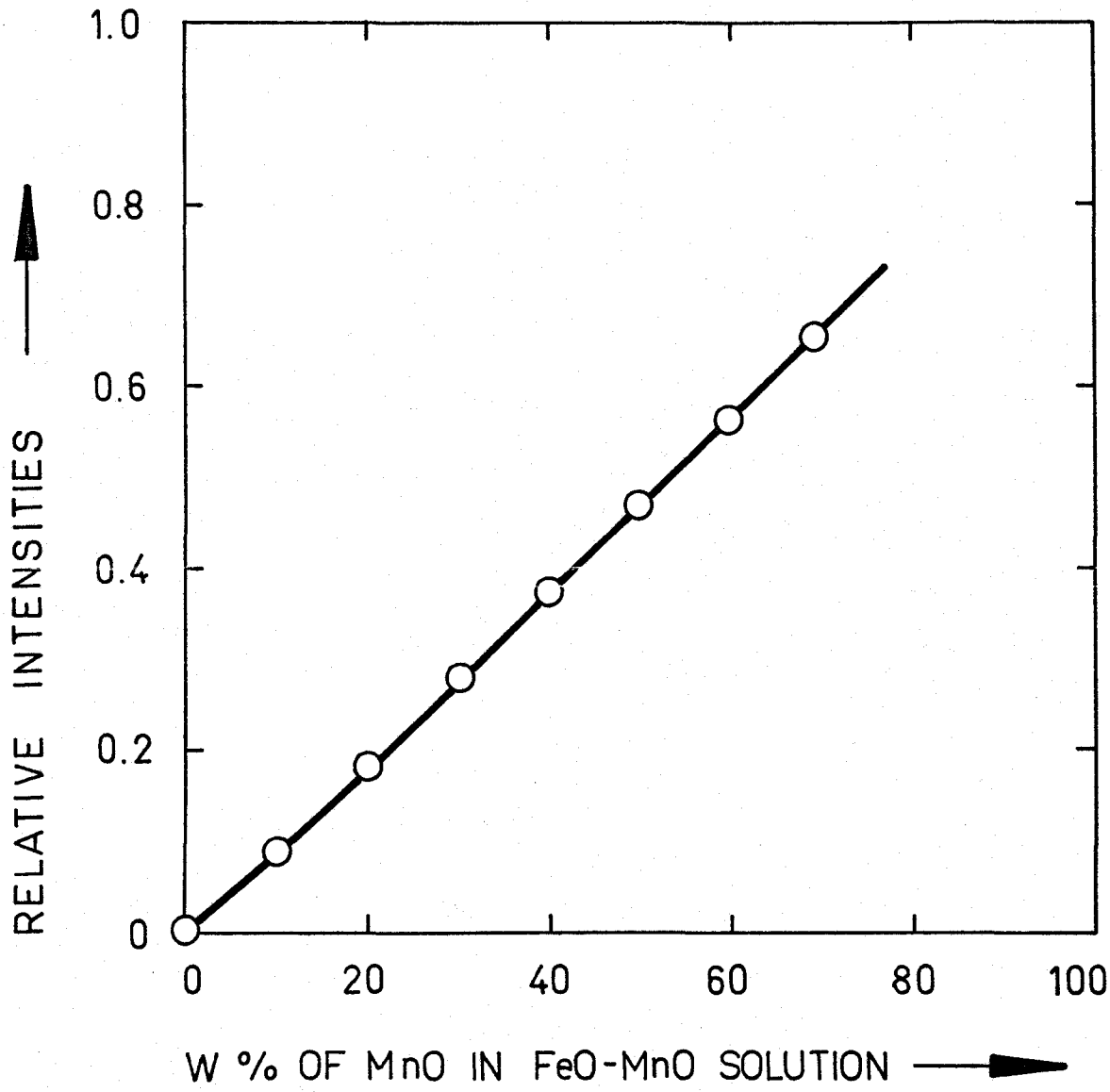

Figure 4.3 Electron Probe Calibration for FeO-MnO Solid Solution.

Table 4.1

Computer Program Used to Calculate the Corrections of Electron Probe Microanalyzer Measurements

```
      PROGRAM TST (INPUT, OUTPUT, TAPES = INPUT, TAPE 6 + OUTPUT)
C     COMPUTATION OF CORRECTIONS FOR ELECTRON PROBE MICROANALYZER
C     WRITTEN BY PETER MAYER ON OCTOBER 17TH, 1970.
C
      READ (5, 100) AWA, AWB, AWO
  100 FORMAT (3F10.4)
      READ (5, 101) RAA, RAB, RAO
  101 FORMAT (3F10.4)
      READ (5, 102) ZA, ZB, ZO
  102 FORMAT (3F10.4)
      READ (5, 103) AJ, BJ, OJ
  103 FORMAT (3F10.4)
      READ (5, 104) HAA, HAB, HAO
  104 FORMAT (3F10.4)
      READ (5, 105) EAK, ANGLE
  105 FORMAT (2F10.4)
      WRITE (6, 201)
  201 FORMAT (1H1,/75H                    CMN          CFE          CO
     1        KMN                KMMN,/)
C
      DO 300 I = 1,770
      CA = FLOAT (I)*0.001
      FA = AWO/AWA
      FB = AWO/AWB
      CB = (1.0 - CA* (1.0 + FA))/(1.0 + FB)
      CO = CA*FA + CB*FB
C
C     ATOMIC NUMBER CORRECTION FOR MANGANESE IN MNO-FEO SOLID SOLUTION
C
      RABO = CA*RAA + CB*RAB + CO*RAO
      EA = (15.0 + EAK)/2.0
      SAA = (ZA/(AWA*EA))* ALOG ((1.166*EA)/AJ)
      SAB = (ZB/(AWB*EA))* ALOG ((1.166*EA)/BJ)
      SAO = (ZO/(AWO*EA))* ALOG ((1.166*EA)/OJ)
      SABO = CA*SAA + CB*SAB + CO*SAO
      AA = ((CA*RABO*SAA)/(RAA*SABO))
C
C     ABSORPTION CORRECTION FOR MANGANESE IN MNO-FEO SOLID SOLUTION
C
      HABO = CA*HAA + CB*HAB + CO*HAO
      F1 = HAA*(1.0/SIN(ANGLE))
      E1 = HABO* (1.0/SIN(ANGLE))
      G1 = 1.2* (AWA/(ZA)**2)
      D1 = 1.2* ((CA*AWA + CB* AWB + CO* AWO)/((CA*ZA + CB*ZB + CO*ZO)**2))
      C1 = (2.39* (10.0**5)/ ((15.0**1.5) - (EAK**1.5)))
```

Table 4.1, Computer Program Used to Calculate the Correction of Electron Probe Microanalyzer Measurements, continued.

```
      A1 = (1.0 + (F1/C1))*(1.0 + ((G1*F1)/C1*(1.0 + G1)))
      B1 = (1.0 + (E1/C1))*(1.0 + ((D1*E1)/C1*(1.0 + D1)))
      X1 = 1.0/(1.0 + G1)
      X2 = 1.0/(1.0 + D1)
      AAM = AA* (A1/B1)*(X2/X1)
C
      WRITE  (6, 200) CA, CB, CO, AA, AAM
  200 FORMAT (5F15.5)
  300 CONTINUE
      END
```

determinations of the concentration profiles in the oxide scales.

CHAPTER V

EXPERIMENTAL RESULTS

5.1 Introduction

The results from the oxidation experiments and various tests will be presented in this section in the form of graphs, tables, and photomicrographs. The experimental and test conditions will be discussed accordingly.

5.2 Oxidation Kinetics

The dependences of the oxidation kinetics on the compositions of exposed alloys and on the oxygen potentials in the reaction atmospheres were determined. All oxidation experiments were conducted at 1000°C, this temperature being maintained within ± 2°C.

The compositions of alloys used in these experiments are shown in Table 5.1. The variation of oxygen potential in a reaction atmosphere was obtained by means of mixing different amounts of CO_2 and CO at 1 atm total pressure. In order to maintain a constant oxygen potential for a given experimental run, a flowing atmosphere was used. Table 5.2 shows the different mixtures of CO_2-CO in v/o used in the present investigations and corresponding oxygen potentials in these atmospheres at 1000°C. The atmospheres were chosen so that only a single phase FeO-MnO solid solution scale is formed. Accordingly, atmospheres 100/1 and 100/10 for the specimens containing zero and 0.93% Mn were omitted due to Fe_3O_4 formation.

Table 5.2

Oxidizing Atmospheres and Corresponding Oxygen Potentials at 1000°C and 1 atm of Total Pressure[44]

CO_2-CO Mixtures [v/o CO_2/ v/o CO]	Oxygen Potential [atm]
100/1	7.45×10^{-12}
100/10	7.45×10^{-14}
70/30	4.06×10^{-15}
50/50	7.45×10^{-16}

Table 5.1

Chemical Analyses of Fe-Mn Alloys

No. of Charge Nominal Composition of Alloys in % [Mn]	% [Mn] in Alloys from Volumetric Wet-way Analysis	% [Mn] in Alloys from Atomic Absorption Spectrophotometry Analysis	Remarks
I/1%	1.0	0.95	
II/1%	0.9	0.93	* No. 2
I/10%	12.0	12.33	* No. 3
II/10%	10.9	10.67	
I/25%	27.5	27.35	* No. 4
II/25%	27.9	27.82	
I/35%	34.0	33.94	
II/35%	31.9	31.83	* No. 5
I/60%	60.0	59.04	* No. 6
II/60%	59.2	58.94	* No. 6

* Alloys used in the present investigations and the alloy No. Specimen designated by No. 1 is pure iron.

The experimental data obtained by recording the increase in weight of a specimen as a function of time are illustrated in Figs. (5.1), (5.2), (5.3) and (5.4). The results are presented as smooth curves since a continuous recording balance was used. In all cases, the weight gains are represented in mg /cm^2. The curves are denoted by numbers which correspond to the particular alloys (see Table 5.1). The oxidation atmosphere is given as a ratio of volume per cent of CO_2 and CO.

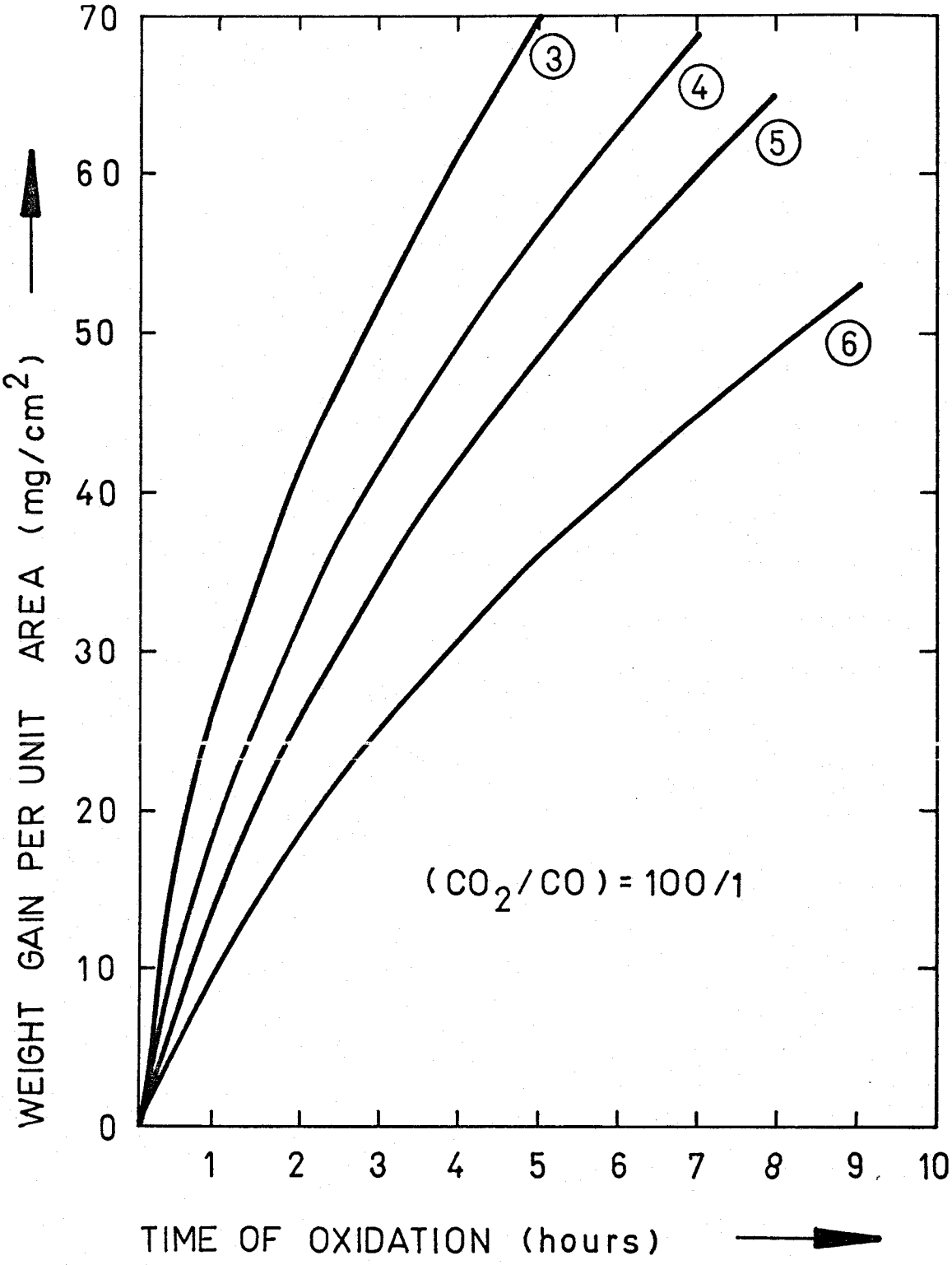

Figure 5.1 Oxidation Kinetics

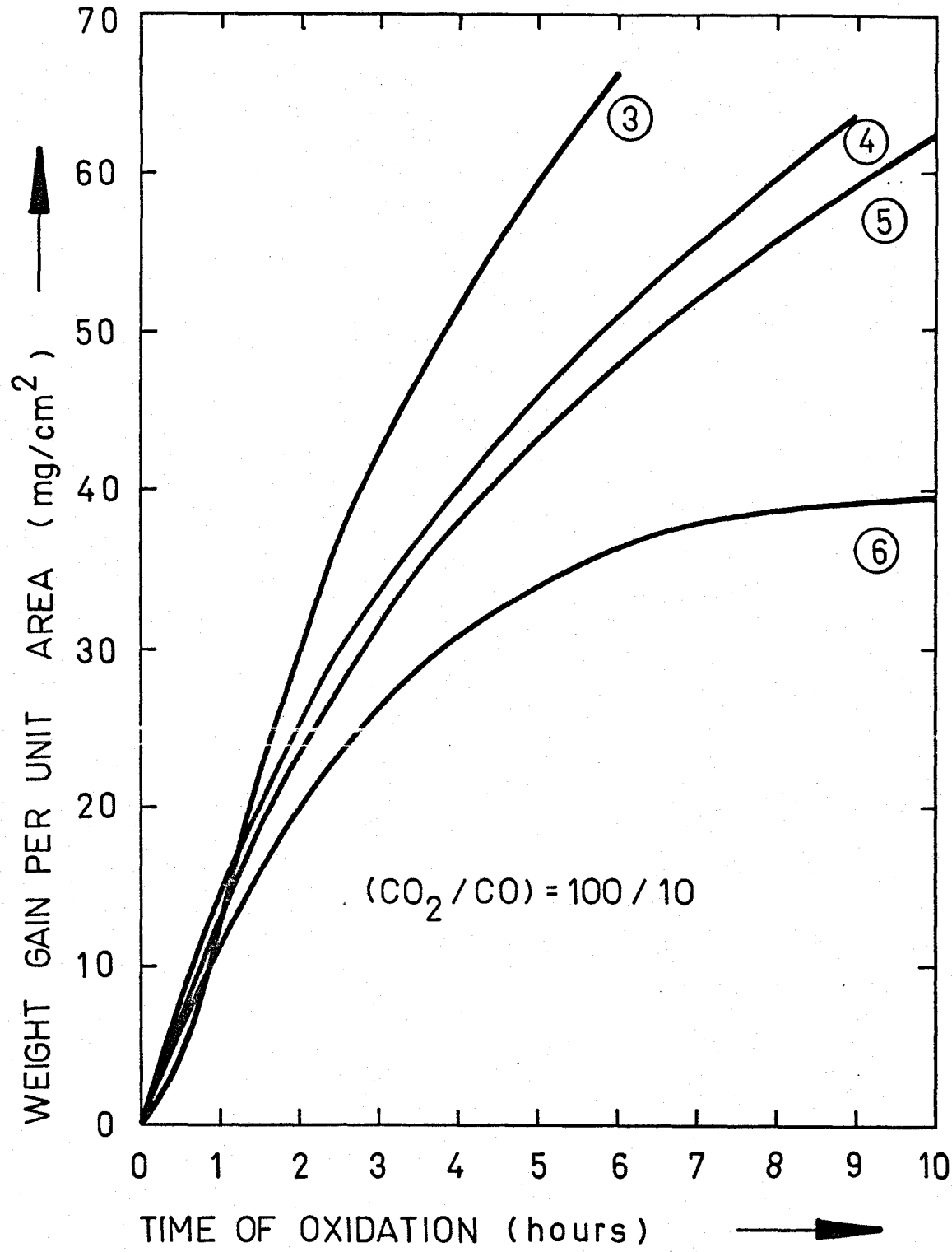

Figure 5.2 Oxidation Kinetics

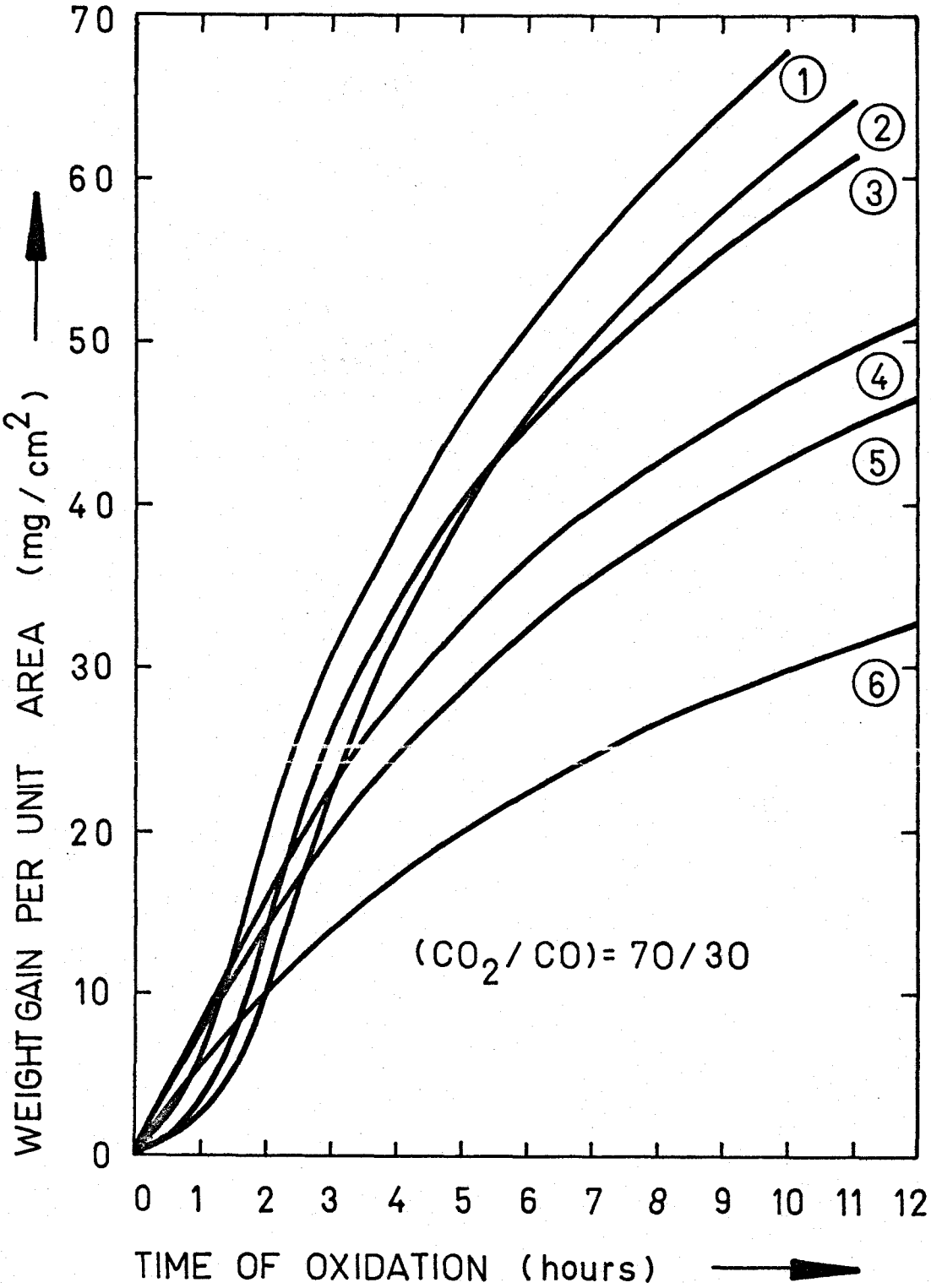

Figure 5.3 Oxidation Kinetics

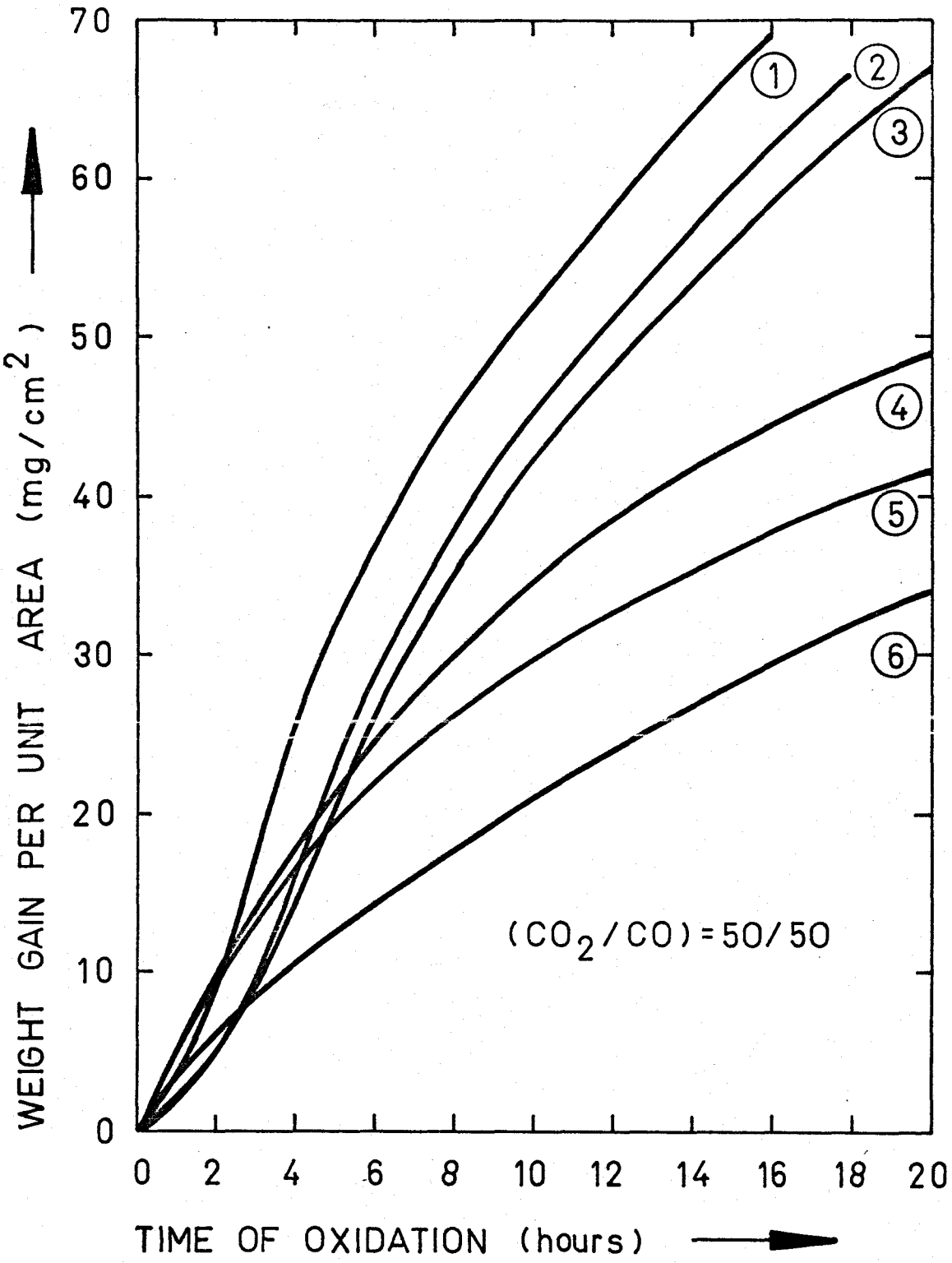

Figure 5.4 Oxidation Kinetics

5.3 Scale Structure and Composition

The structure and composition of an oxide scale were examined as we mentioned earlier by means of optical microscopy, X-ray diffraction, electron microprobe analyses and wet chemical analyses.

5.3.1 Metallography and Microscopic Observations

The metallography in this section is pertinent to observations at room temperature on the oxide scales and metal structures formed at the reaction temperature 1000°C. The basic characteristic, which Fe-Mn alloys exhibited under the experimental conditions used in the present investigation, was formation of an adherent oxide scale on the top of the underlying metal. The alloy beneath the scale did not exhibit any extensive internal oxidation phenomenon. The final oxide scale was in the order of a few hundred μm.

A series of micrographs for the oxidized samples is shown in Fig. (5.5). The first micrograph in Fig. (5.5) represents the cross section of an exposed Fe-12.33% Mn sample in 70% CO_2 and 30% CO atmosphere for 4 hours. The remaining micrographs represent the same alloy exposed for 5 and 6 hours. The one phase oxide scale is attached to the base alloy. Various etching techniques were used in order to identify the occurrence of different phases but all of them were unsuccessful. Metallographically it was possible to distinguish only one oxide phase which apparently is a solid solution of FeO-MnO. This series of micrographs demonstrates the common feature of the oxidation of Fe-Mn alloys.

4 hours of oxidation

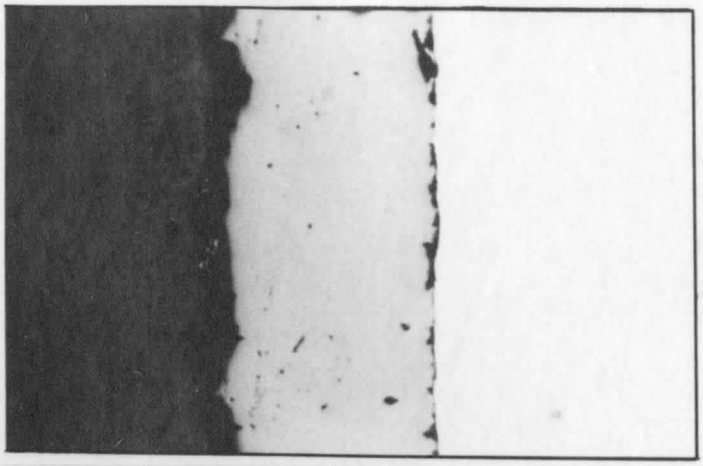

5 hours of oxidation

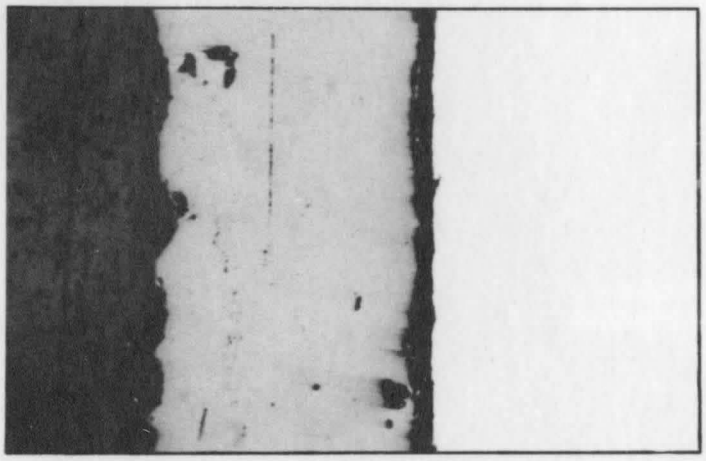

6 hours of oxidation

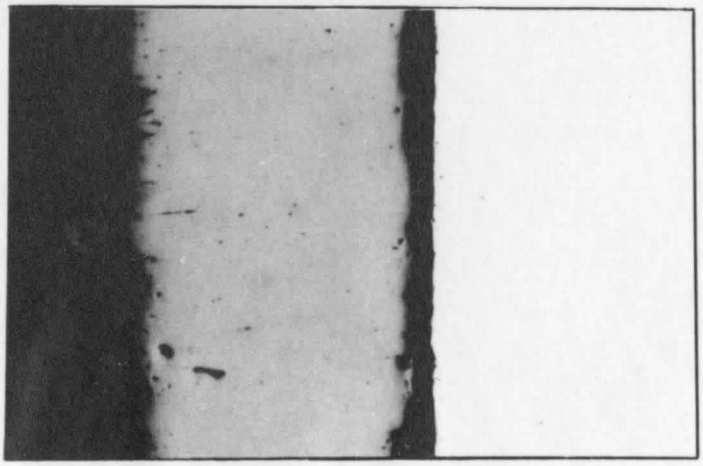

Figure 5.5 The Metallographical Cross Section of Oxidized Fe-12.33% Mn Alloy in CO_2-CO = 70/30 Atmosphere at 1000°C. 30X.

5.3.2 X-ray and Chemical Analyses

A standard X-ray Debye-Scherrer method described previously was used to determined the crystallographic structure of an oxide scale. Finely ground (particle size 1-10μ) scales formed on the top of pure Fe, and Mn and alloys used in the present investigation were exposed to molybdenum radiation in order to obtain powder photographs. Fig. (5.6) represents the typical diffraction pattern obtained from wustite, manganeous oxide and from scales of alloys formed in various CO_2-CO atmospheres at 1000°C. All the powder photographs exhibited similar diffraction patterns which were easy to identify as a face centred cubic (rock-salt type) structure. No other phases were identified by this method with the exception of pure iron and alloy No. (1) exposed to pure CO_2 and a 100/10 CO_2-CO atmosphere. In these cases, the presence of magnetite was identified. However, the powder micrographs obtained from the scales of different alloys as well as from pure Fe and Mn showed variations in the lattice parameter. Table 5.3 shows the observed values of the lattice parameter calculated with the help of a computer and also the corresponding bulk chemical composition of scales obtained from chemical analyses by means of the volumetric method. So obtained experimental results are illustrated in Fig. (5.7).

5.3.3 Concentration Profiles in Metal and Oxide Scale

The specimens exposed to various oxidation atmospheres in the kinetic tests were examined, in order to determine concentration profiles of Mn and Fe in the metal phase as well as in the adjoining oxide scale. In Figs. (5.7-5.11) the concentration profiles are illustrated as calculated from the electron microprobe measurements by the point counts method. The

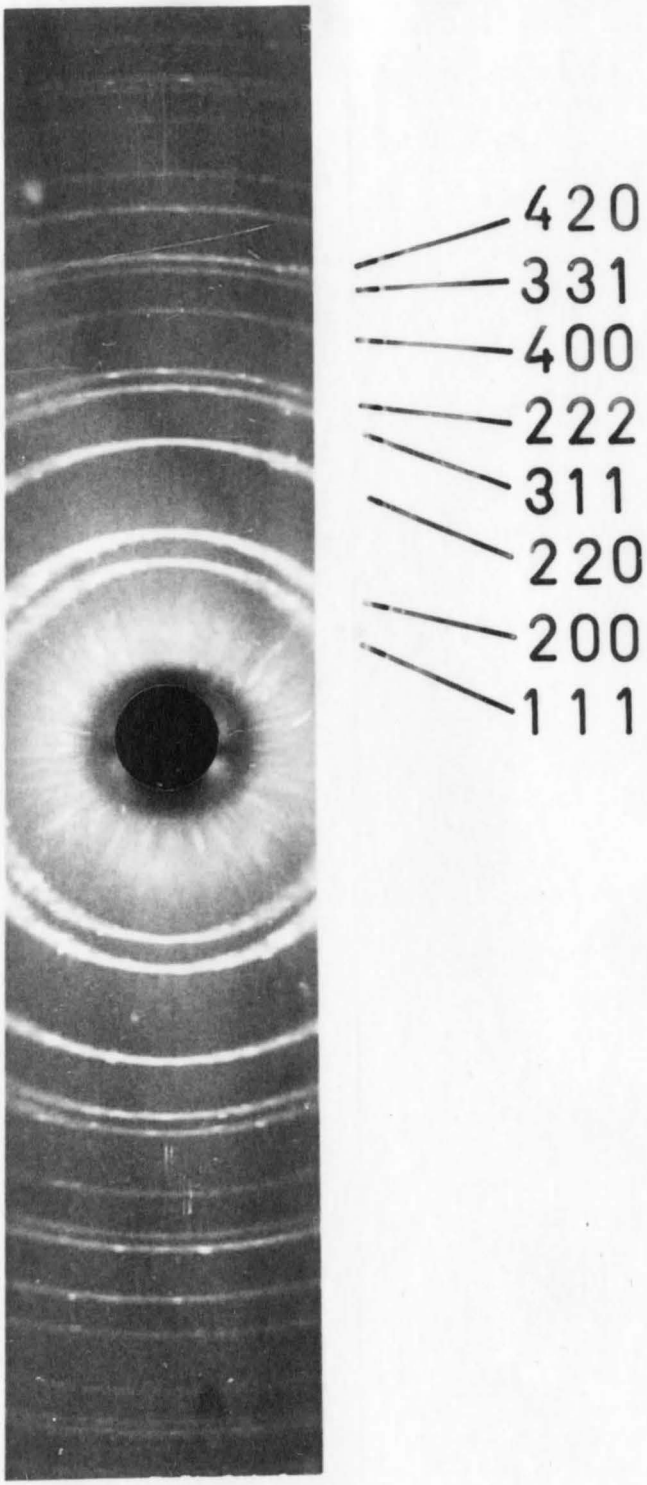

Figure 5.6 Diffraction Pattern from Scale Formed on Fe-12.33% Mn Alloy.

Table 5.3

Results of Volumetric and X-ray Diffraction Analysis

Base Alloy Mole Fraction of Mn in Base Alloy	Atmosphere $\frac{CO_2}{CO}$ = 100/1 [v/o]		100/10		70/30		50/50	
	Mole Fraction of MnO in Scale	Lattice Parameter [Å]	MnO	Lattice Parameter	MnO	Lattice Parameter	MnO	Lattice Parameter
Pure Fe	0.000	4.3154	0.000	4.3104	0.000	4.3059	0.000	4.3168
.0093	.0097	4.3168	0.0097	4.3191	.0097	4.3108	.0097	4.3124
.1233	.1208	4.3301	.1210	4.3257	.1212	4.3310	.1212	4.3304
.2735	.2735	4.3598	.2738	4.3584	.2732	4.3581	.2740	4.3599
.3183	.3183	4.3603	.3183	4.3614	.3189	4.3616	.3190	4.3609
.5904	.5904	4.9113	.5908	4.4100	.5914	4.4109	.5920	4.4103
1.0000	1.0000	4.4491	1.0000	4.4490	1.0000	4.4482	1.0000	4.4490

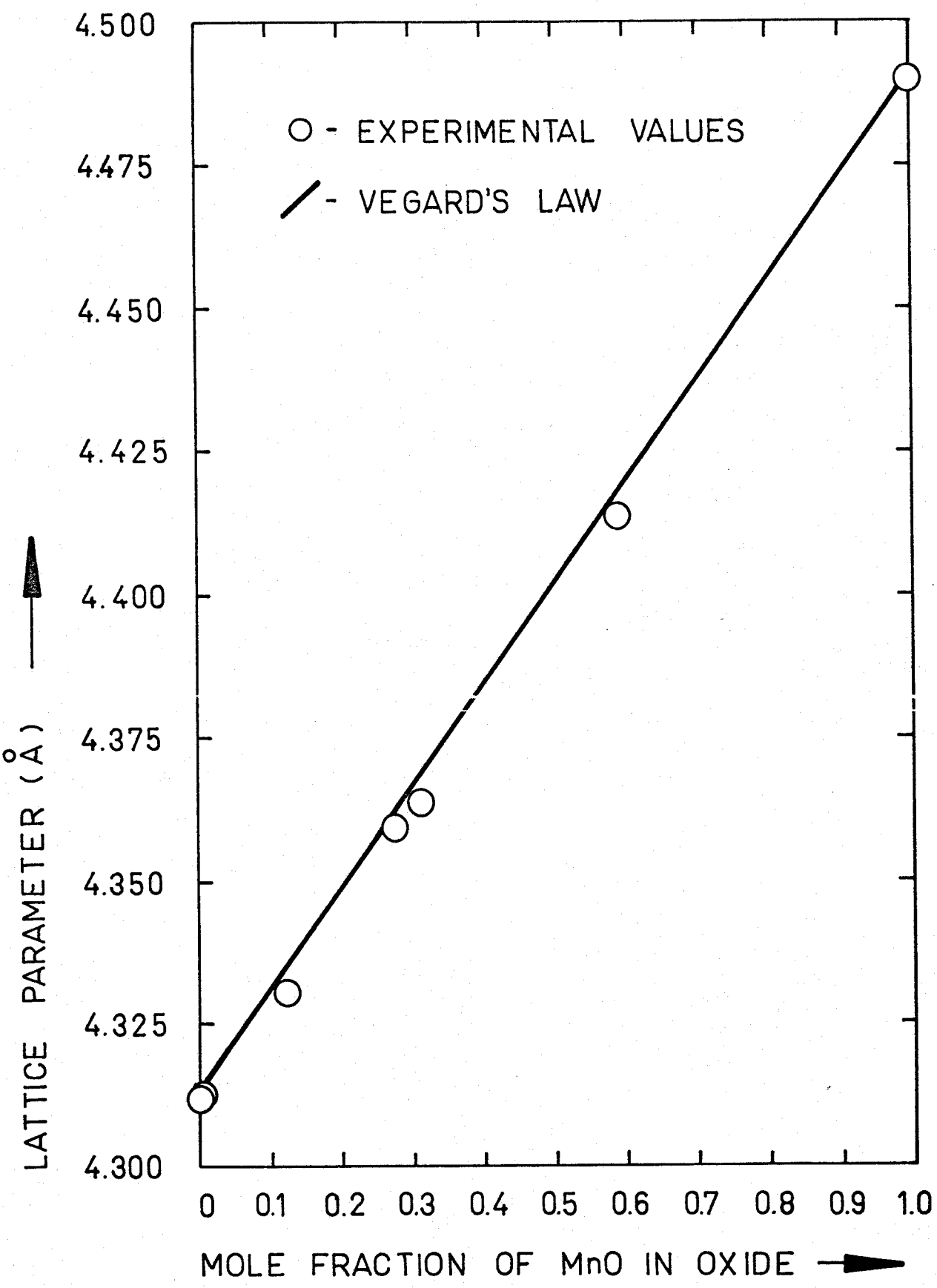

Figure 5.7 Lattice Parameter as a Function of MnO Content in the FeO-MnO Solid Solution.

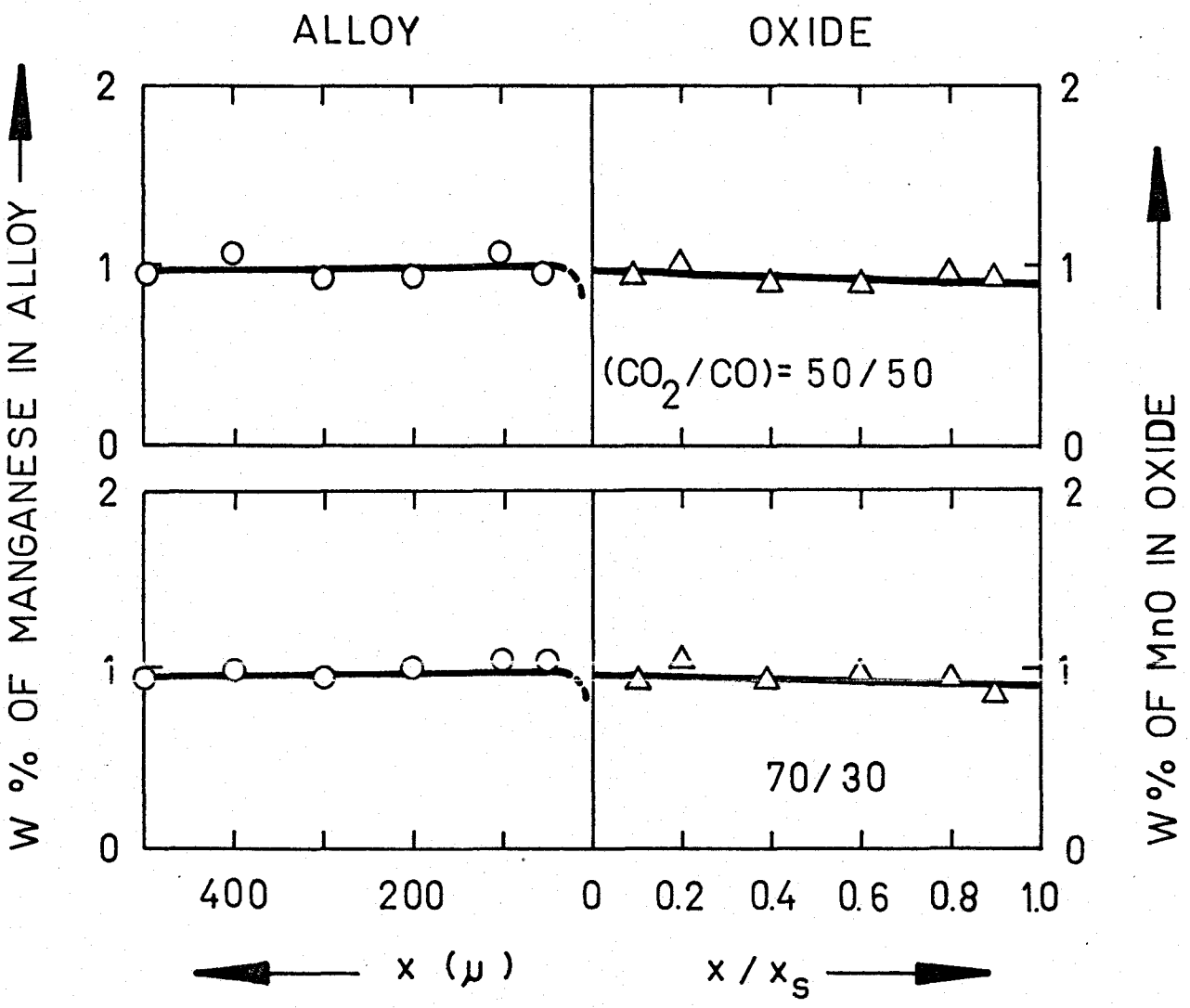

Figure 5.8 Concentration Profiles for Mn in Alloy and MnO in Oxide of Fe-0.93 % Mn Alloy Oxidized at 1000°C.

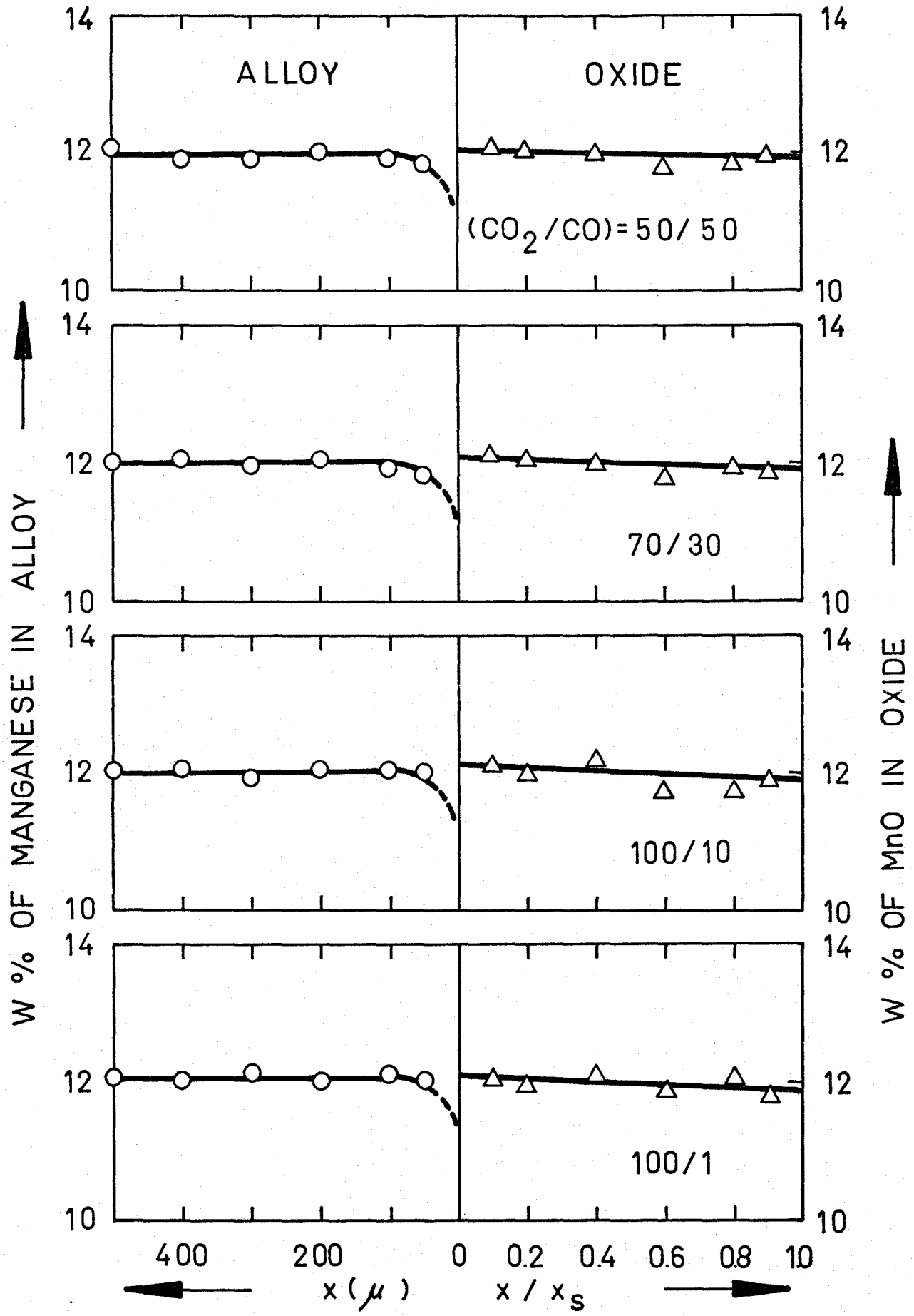

Figure 5.9 Concentration Profiles for Mn in Alloy and MnO in Oxide of Fe-12.33% Mn Alloy Oxidized at 1000°C.

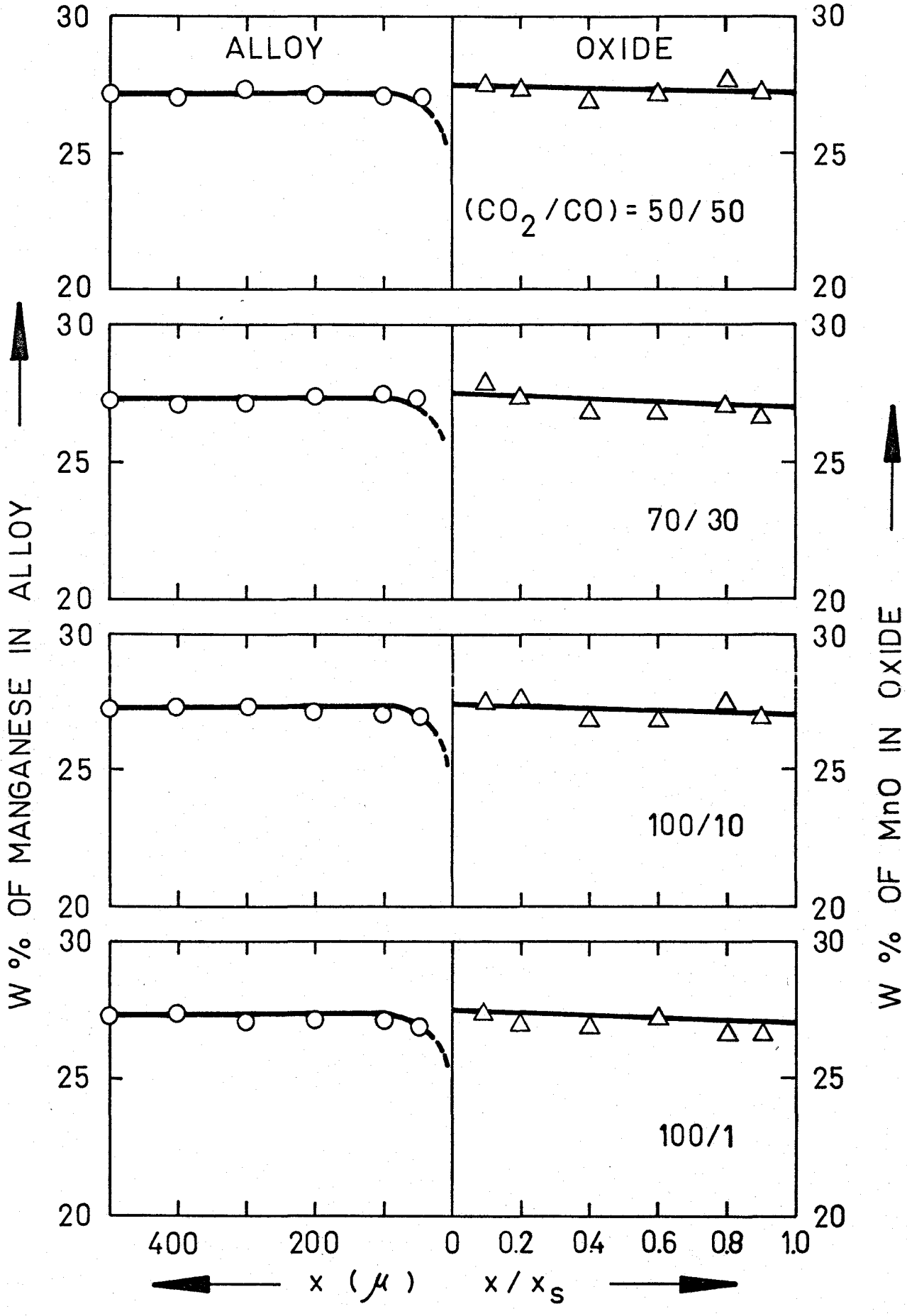

Figure 5.10 Concentration Profiles for Mn in Alloy and MnO in Oxide of Fe-27.35% Mn Alloy Oxidized at 1000°C.

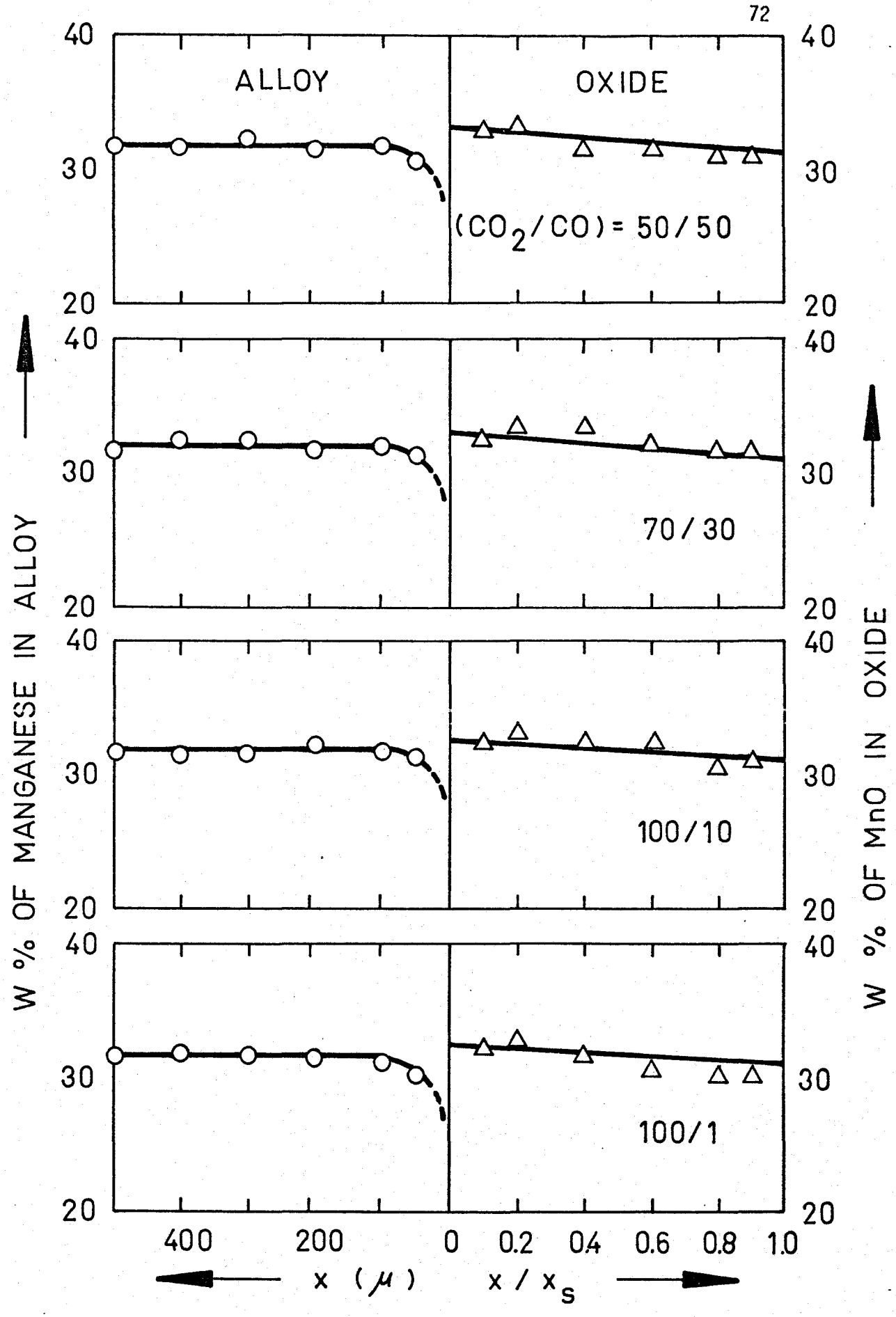

Figure 5.11 Concentration Profiles for Mn in Alloy and MnO in Oxide of Fe-31.83% Mn Alloy Oxidized at 1000°C.

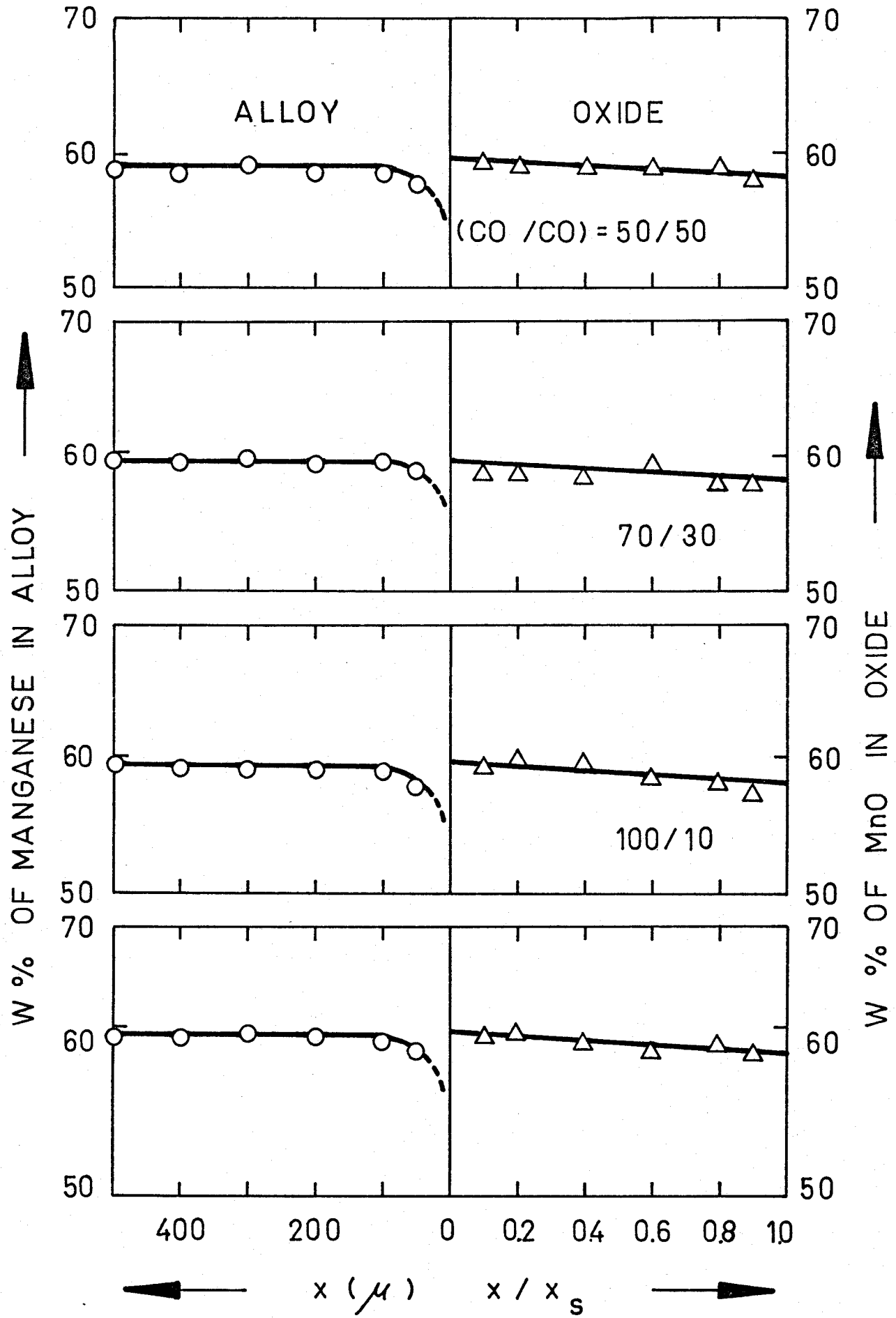

Figure 5.12 Concentration Profiles for Mn in Alloy and MnO in Oxide of Fe-59.04% Mn Alloy Oxidized at 1000°C.

experimental conditions are quoted on each figure separately. The manganese profile in the oxide is plotted as w/o of MnO obtained by simple calculations from w/o of Mn because it illustrates much better the actual physical picture. The location within the oxide phase is expressed by ratio of the distance from the alloy-scale interface to the instantaneous thickness of the scale. The concentration profile of Mn in the metal is plotted as the distance from the alloy-scale interface in μ versus the w/o of Mn. The concentrations in oxide scale, marked as triangles, are mean values for different exposure times in the parabolic region of oxidation kinetics. The circles in the alloy represent also the mean values of Mn concentration for different exposure times in the same kinetic region. The accuracy of the measurements is illustrated in the form of deviations from the mean values listed in Table 5.4.

The plots show that the variation of concentration of MnO across the oxide scale is very small. There is, however, a definite decrease of MnO content towards the outer interface and simultaneous FeO enrichment. The profiles are very flat and appear linear since the electron microprobe is not sufficiently sensitive to demonstrate any fine variations of concentration. The same problem appears when examining the variation in profiles with oxygen potential at the outer interface.

The concentration profile of Mn in an alloy is measureable close to the alloy-scale interface. If the measuring is done within 10 μ of the interface, there is interference from the X-rays generated within the oxide phase and the values obtained are sums of the intensities coming from metal and oxide. Fig. (5.13) shows for example the measured profile at the metal-scale interface for the 12.33% Mn alloy. This is not an actual profile

Table 5.4

The Deviation Limits of Microprobe Measurements of Concentration Profiles in Alloys and Oxide Scales

Base Metal Alloy [Mn %]	Error Bounds for the Profile in Metal [Mn %]	Error Bounds for the Profile in Scale [MnO %]
0.933	± 0.3	± 0.5
12.33	± 1.0	± 1.5
27.355	± 1.5	± 2.5
31.832	± 1.5	± 2.0
59.04	± 2.0	± 2.5

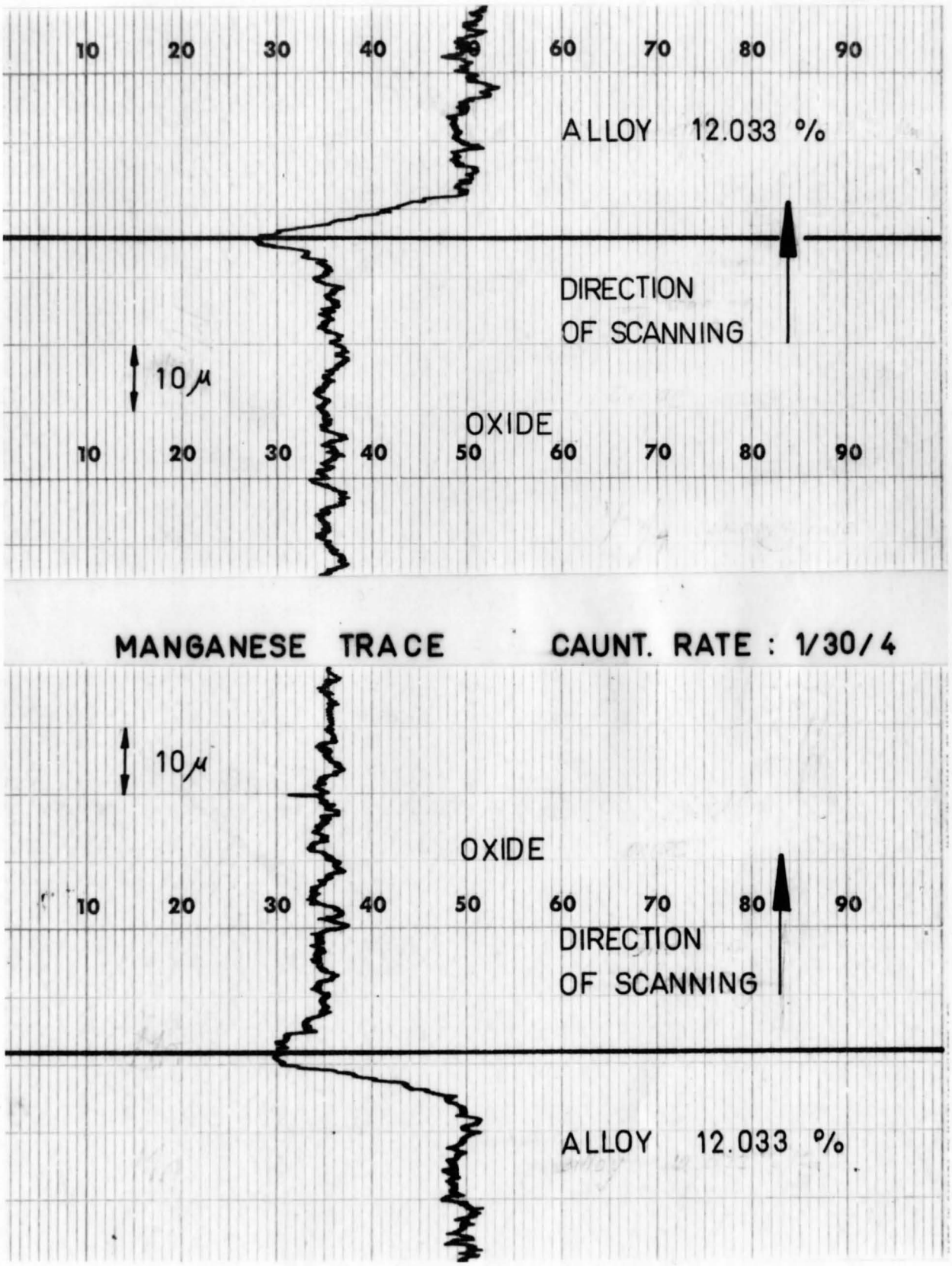

Figure 5.13 Line Scan for Distribution of Mn in the Alloy Matrix and Oxide Phase Near the Internal Interface.

but a statistical intensity distribution due to the phenomenon described above. Although the interfacial concentration in the metal cannot be measured by this technique, it is obtainable by calculation. The concentration profile in the oxide is not as steep as in the alloy and its interfacial concentration was obtained by extrapolation. Knowing the tie line in the ternary phase diagram between these two phases, it was then possible to calculate the interfacial Mn concentration in the alloy. Calculations showed that this concentration is very small. The specimens analyzed by electron probe microanalyzer were selected in order to investigate the concentration profiles at the longer oxidation times when the weight gain was not directly proportional to time, which shall be later approximated as parabolic.

CHAPTER VI

ANALYSIS AND DISCUSSION OF EXPERIMENTAL RESULTS

6.1 Introduction

In the following chapter the influence of manganese is discussed on the oxidation properties of the Fe-Mn alloys in different oxidizing atmospheres. The results obtained by different analytical methods are employed in order to correlate the results from the present experiments with the existing general theoretical treatment of the problem. From the thermogravimetric measurements combined with the other observations, it is possible to gain valuable information about the reaction mechanisms, the rate controlling reaction, the transport and structural properties of the FeO-MnO solid solutions. Additional experiments are needed as well as theoretical derivations based on experimental results in order to obtain a complete picture of the oxidation characteristics of Fe-Mn alloys in CO_2-CO atmospheres.

6.2 Reaction Rates

The experimentally obtained weight gain-time curves, in general, for oxidation of Fe-Mn alloys up to 12% Mn content in the base alloy can be best described as composed of three intervals:

(i) an initial period of low linear reaction rate,

(ii) an intermediate period of linear oxidation rate considerably greater than the first period,

(iii) a final period of parabolic oxidation.

The weight gain-time curves for alloys containing more than 12% Mn did not exhibit the two initial linear oxidation regions before onset of parabolic kinetics.

6.2.1 Linear Oxidation

The experiments on the linear sections of the reaction curves are only preliminary, since the main objectives of the present work were to investigate the parabolic growth kinetics, structures and compositions of a single phase scale on the Fe-Mn alloys. Therefore, the problem is discussed only briefly.

Two sets of experimental weight gain-time curves are shown in Figs. (6.1) and (6.2). Fig. (6.1) illustrates the initial stages of oxidation of the alloy series in a 50/50 CO_2/CO atmosphere and Fig. (6.2) illustrates the initial oxidation in a 70/30 atmosphere. Both series show the same feature. Low alloyed samples exhibit a characteristic curve shape, which has been found previously[32,33,41] for the oxidation of pure iron. High alloyed samples show onset of diffusion-controlled oxidation essentially from the commencement of the reaction. For the alloys with manganese concentrations of 0 w/o, 0.99 w/o and 12.33 w/o, the initial portion of the rate curve consisted of two regions of approximately linear slopes. The first linear region was observed for oxide thicknesses about 10^{-4} cm to 10^{-3} cm and appeared to be related to the grain size of metal substrate, mechanical finish of the surface, etc.[33]. The rate of reaction in the second linear region was always greater than that for the first.

The analysis of the first linear region is outside the scope of this work.. The slopes of the second linear region of the weight gain-time

curves may be used to determine linear oxidation constants,

$$\left(\frac{\Delta m}{A}\right) = k_L t \qquad (6.1)$$

The k_L's obtained from the present experiments as well as from the literature are listed in Table 6.1 and graphically represented in Fig. (6.3). It appears that the magnitude of the linear scaling constants do not change upon addition of manganese to the alloy. The present results are in agreement with experimental results obtained by Pettit and Wagner[32] for pure iron. Although the slopes do not change with addition of Mn to the base metal, the length of the second linear region changes considerably. The second linear region disappeared in oxidation curves of alloys with Mn-content 27.355 w/o and larger. With decreasing length of the second region, the limiting thickness of oxide before the onset of diffusion control decreased from approximately 1×10^{-2}cm to nearly zero. The limiting thickness of the scale before diffusion becomes a rate controlling process may be determined by the decrease in diffusion rate with increased manganese content in the scale.

In Chapter III the linear oxidation kinetics of iron were interpreted by a model for transport of iron via vacancies and positive holes in wustite to react with oxygen at the oxide/gas interface. The dissociation of carbon dioxide to chemisorbed oxygen and its incorporation into the wustite lattice were assumed to determine the reaction rate. This mechanisms has been expanded by Morris and Smeltzer[35] to account for the oxidation kinetics of alloys. Accordingly, the scale growth on Fe-Mn alloy may be represented by the following reaction

$$CO_{2(g)} = O^{2-}_{(ads)} + CO_{(g)} + 2\oplus \qquad (6.2)$$

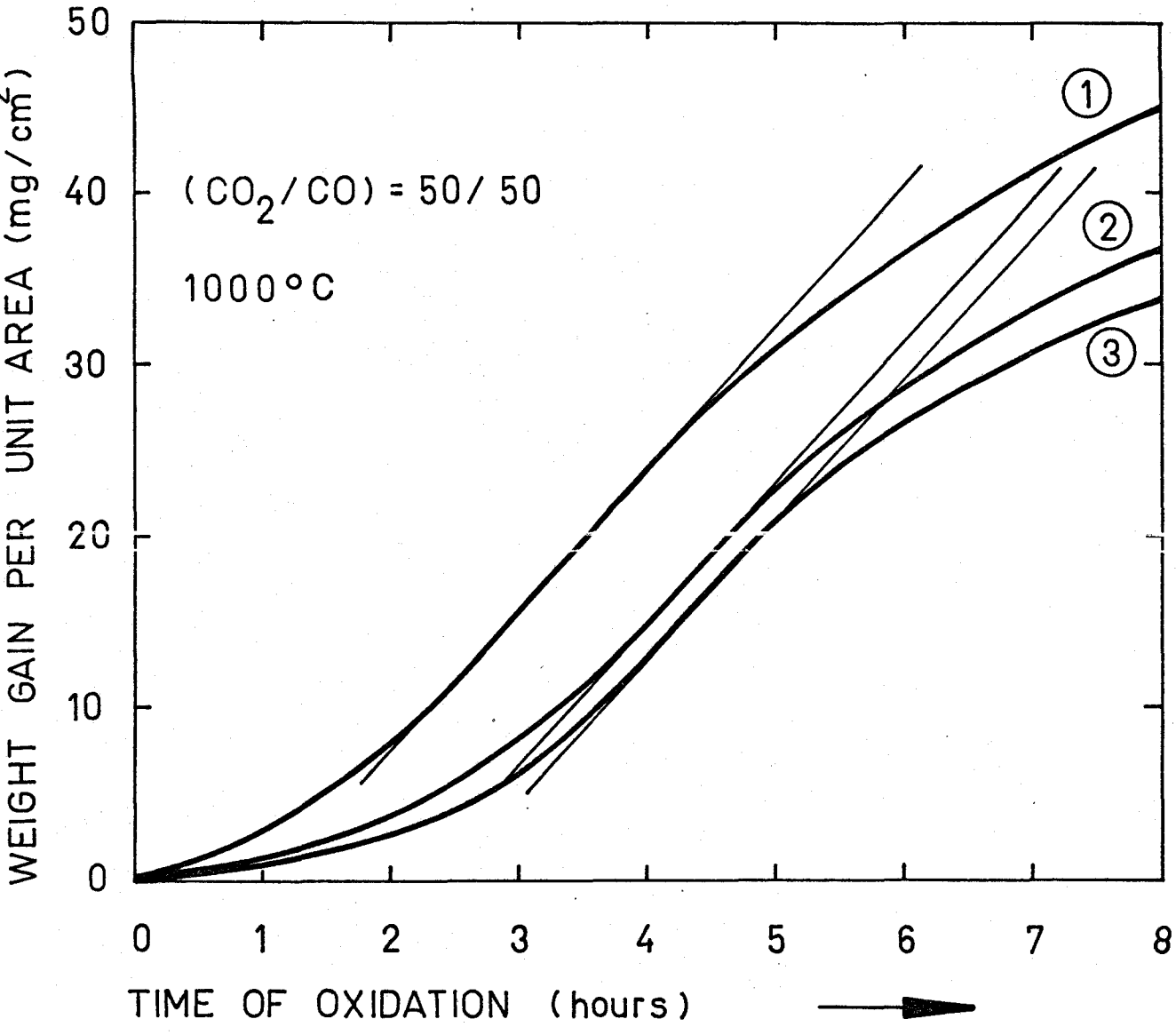

Figure 6.1 Linear Oxidation Kinetics

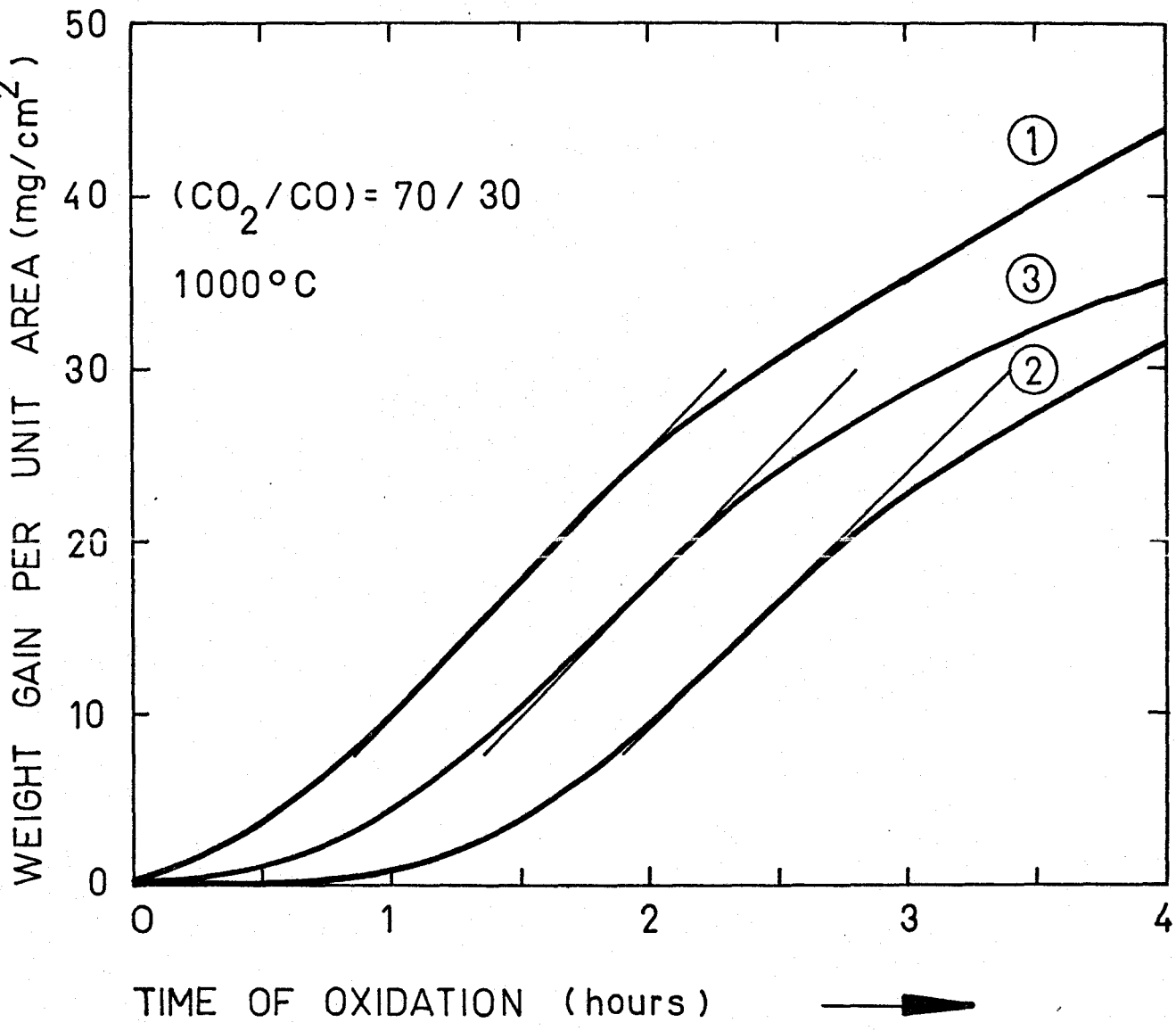

Figure 6.2 Linear Oxidation Kinetics

Table 6.1

Second Linear Oxidation Rate [g/cm^2]

[% Mn] in Alloy	Atmospheres CO_2/CO (v/o)	
	50/50	70/20
0.000	2.6×10^{-6} 1.9×10^{-6} 2.1×10^{-6}	4.5×10^{-6} 3.9×10^{-6} 4.2×10^{-6}
0.99	1.7×10^{-6} 1.8×10^{-6} 2.0×10^{-6}	3.5×10^{-6} 3.8×10^{-6} 3.9×10^{-6}
12.33	2.0×10^{-6} 1.9×10^{-6} 1.8×10^{-6}	3.8×10^{-6} 4.2×10^{-6} 4.3×10^{-6}

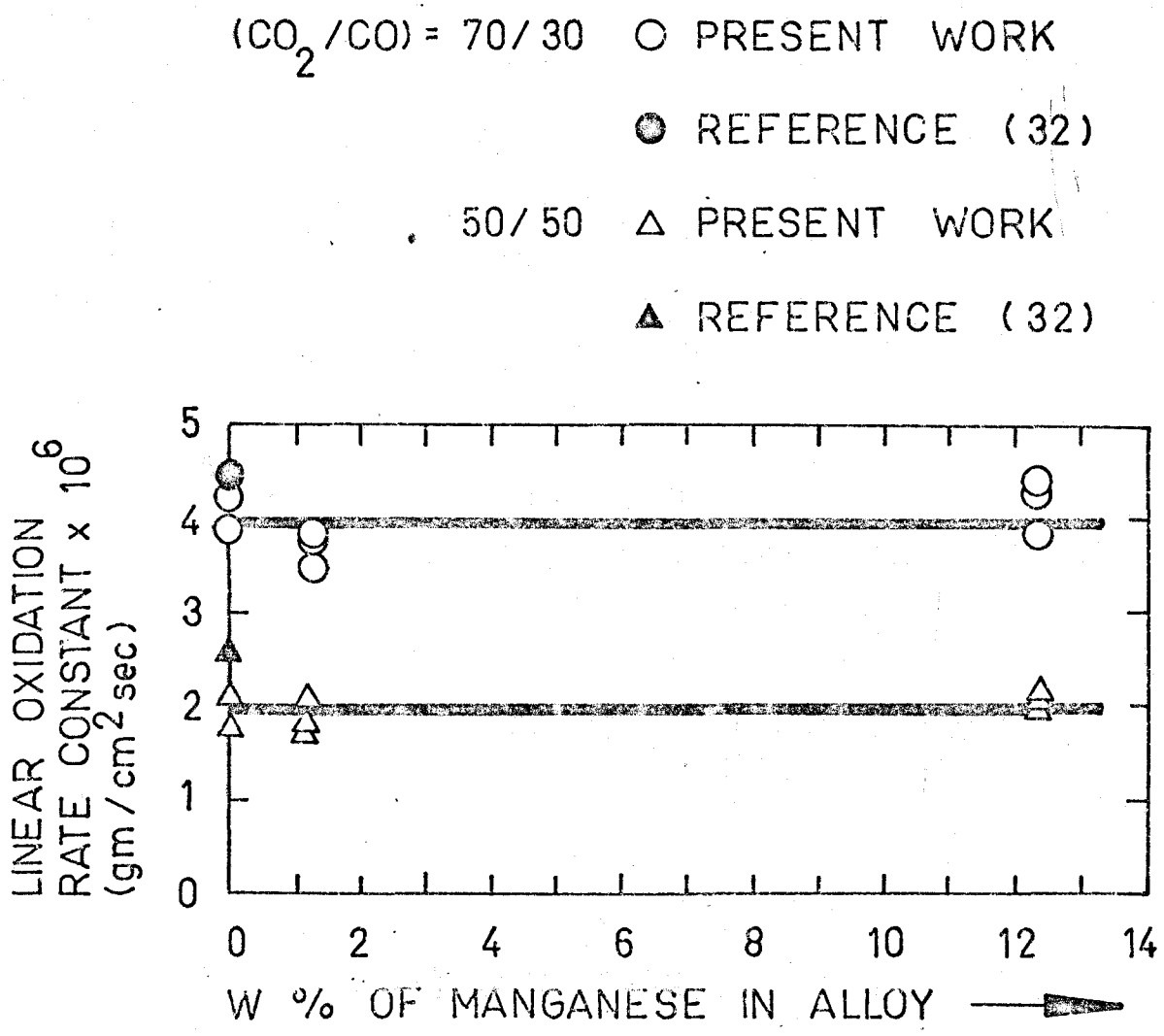

Figure 6.3. Linear Oxidation Constants a Function of Mn Content in Fe-Mn Alloys and Oxygen Potential.

$$O^{2-}_{(ads)} = (Fe\ Mn)\ O + Fe''_{\square} \quad (6.3)$$

$$Fe''_{\square} + 2\oplus + Fe(alloy) = Nil \quad (6.4)$$

$$Mn\ (alloy) = Mn\ (oxide) \quad (6.5)$$

Equations (6.2) and (6.3) represent the rate controlling surface reaction steps involving dissociation of carbon dioxide and incorporation of chemisorbed oxygen into the wustite lattice. For the case of linear oxidation the transport of ions in the lattice is assumed to be rapid and not rate controlling during the period of linear oxidation. Nil refers to the annulment of lattice defects by the solution of Fe in wustite. (Fe Mn) O represents the solid solution of FeO and MnO.

The fact that the linear oxidation constants in a given atmosphere do not change with the addition of manganese to the base alloy suggests, that the reaction rate is not dependent on Mn concentration at the oxide-gas interface. If this is valid, the incorporation of adsorbed oxygen may not play a role in the rate-controlling reaction. Consequently, the oxidation rate changes with oxygen potential in a given reaction atmosphere may be related to the mechanism, where dissociation of CO_2 into CO and adsorbed oxygen is the slowest step in the reaction sequence.

6.2.2 Parabolic Oxidation Kinetics

The reaction course in the third period of oxidation which could be approximated to obey a parabolic law refers to steady state scaling controlled by diffusion through the oxide scale. In this system, as in

many instances of alloy oxidation, it required time and considerable thickness of scale before the steady-state pattern was fully attained. The required time varied from alloy to alloy and was dependent on relative values between the rate of interfacial reaction and the rate of diffusion through oxide.

The parabolic law for oxidation was discussed in Chapter II and could be expressed in the form

$$\left(\frac{\Delta m}{A}\right) = \sqrt{k_p t} \quad \text{or} \quad \left(\frac{\Delta m}{A}\right)^2 = k_p t \ . \qquad (6.6) \text{ and } (6.7)$$

Upon plotting the experimental data on diagrams where the abscissa is time and the ordinate is the square of weight gain per unit area, the experimental curves yielded straight lines. A sample set of experimental curves is shown in Figs. (6.4 - 6.7) for four different oxidizing atmospheres at 1000°C. Each curve is designated by a number which represents an alloy with a particular content of manganese (see Table 5.1). The slopes of the lines are k_p's - parabolic oxidation constants according to the equations (6.6 and 6.7). The parabolic oxidation constants are listed in Table (6.2). The values of k_p's are means from the numerous experiments. Each experiment was repeated at least two times. The deviations from the mean values are also listed in Table 6.1 and were in the limits of ± 15%. This reproducibility in oxidation studies is considered as acceptable.

The parabolic oxidation rate constants are plotted versus the bulk manganese composition of alloys in Fig. (6.8). These results show that there is a considerable decrease in the oxidation rate with an increase of bulk manganese concentration of alloys. This general decrease may be

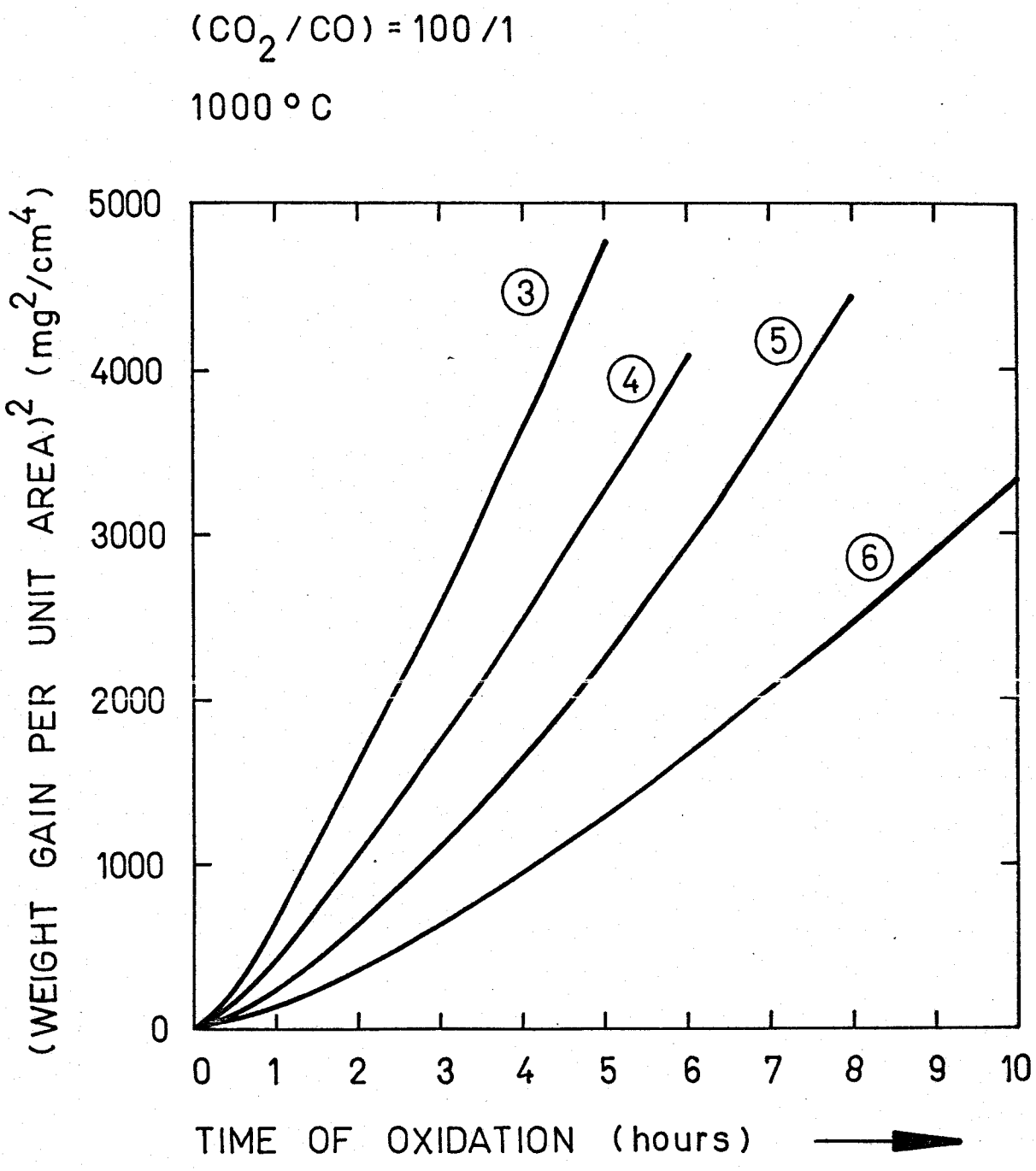

Figure 6.4 Parabolic Oxidation Kinetics

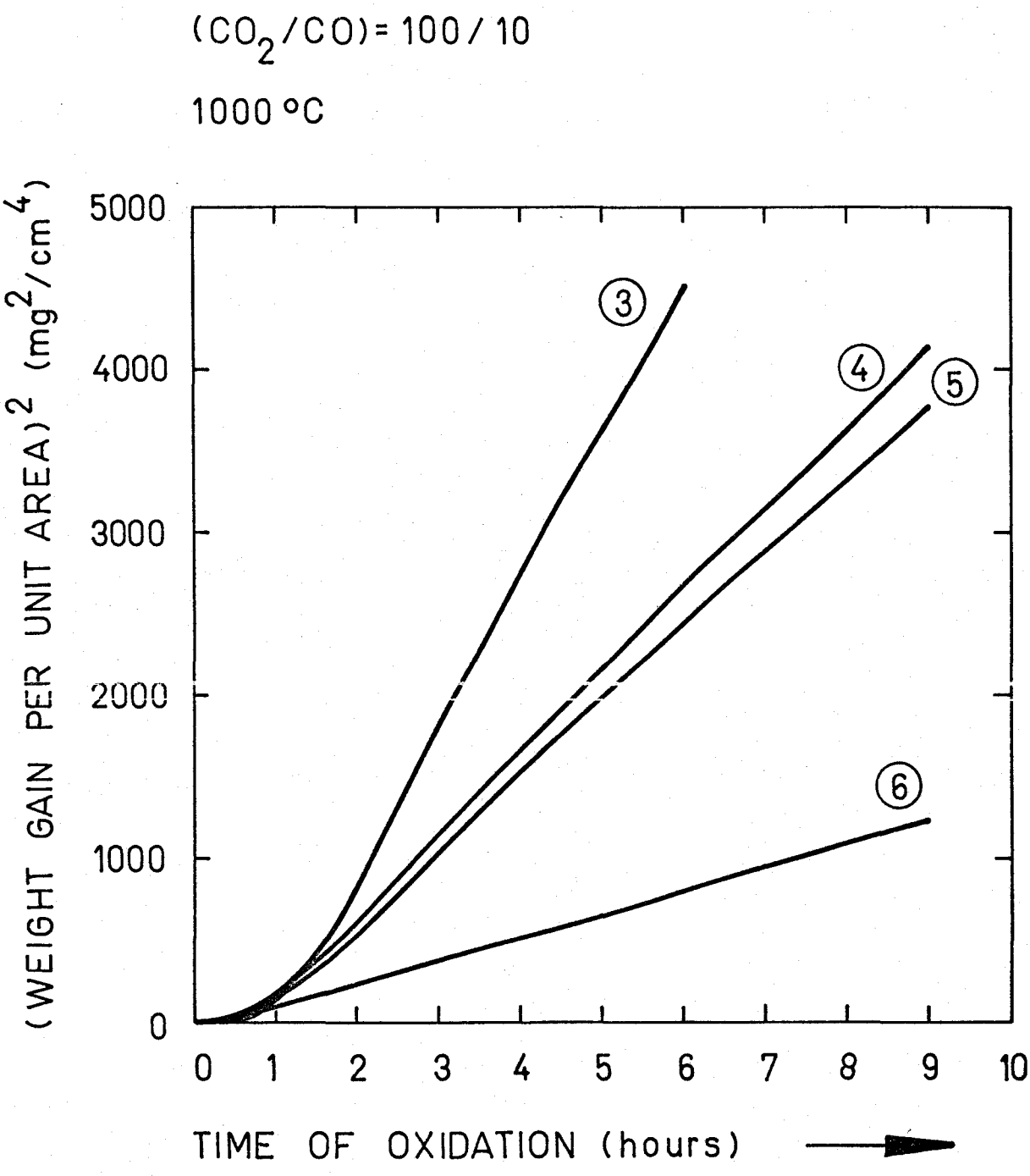

Figure 6.5 Parabolic Oxidation Kinetics

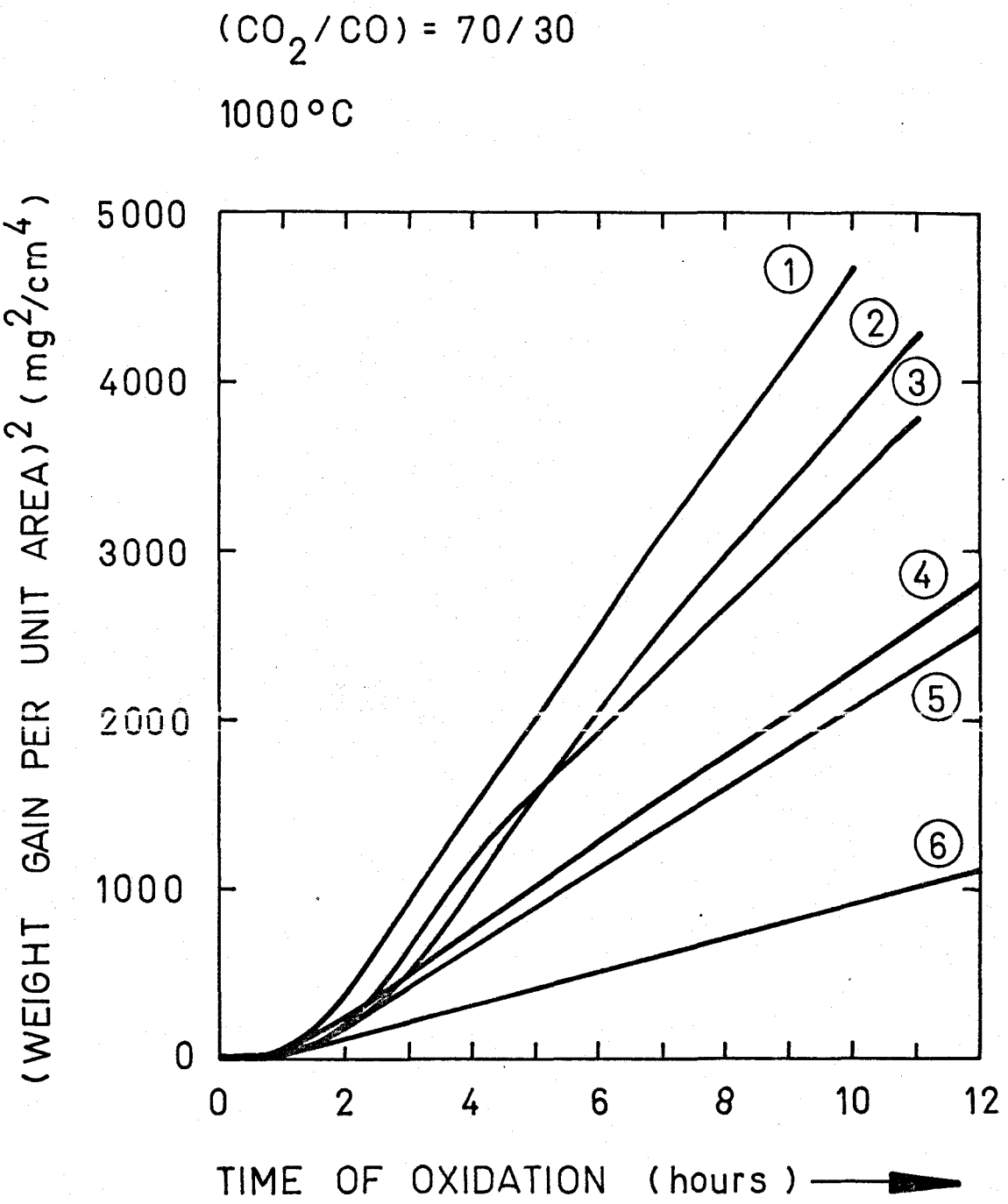

Figure 6.6 Parabolic Oxidation Kinetics

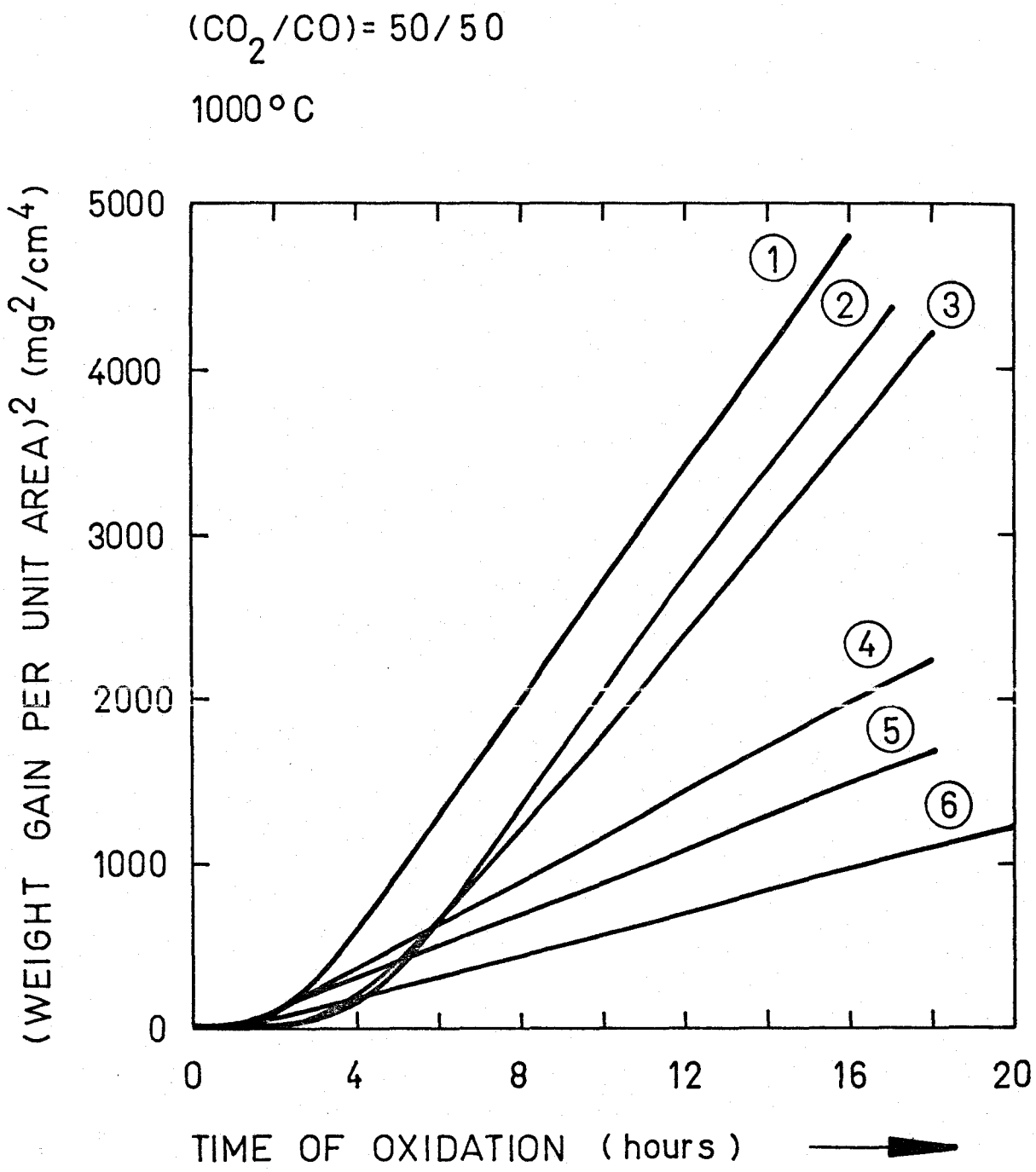

Figure 6.7 Parabolic Oxidation Kinetics

Table 6.2

Parabolic Oxidation Rate Constant for Fe-Mn Alloys in CO_2-CO Atmospheres at 1000°C

Atmosphere CO_2/CO [v/o] / Alloy Composition [% Mn]	Parabolic Oxidation Rate Constant (x 10^{-9}) gm^2/cm^2 sec			
	50/50	70/30	100/10	100/1
0.933	89.17 ± 10.7	117.78 ± 15.31	-	-
12.33	90.27 ± 13.54	111.11 ± 9.87	190.00 ± 15.2	276.67 ± 24.9
27.355	41.39 ± 3.31	66.89 ± 4.68	135.00 ± 9.45	237.50 ± 16.62
31.832	38.33 ± 3.83	6394 ± 6.39	123.00 ± 7.38	183.10 ± 21.97
59.045	27.09 ± 2.709	31.66 ± 3.48	73.00 ± 8.76	113.33 ± 11.33
0.00	97.22 ± 4.86	136.67 ± 16.40	-	-

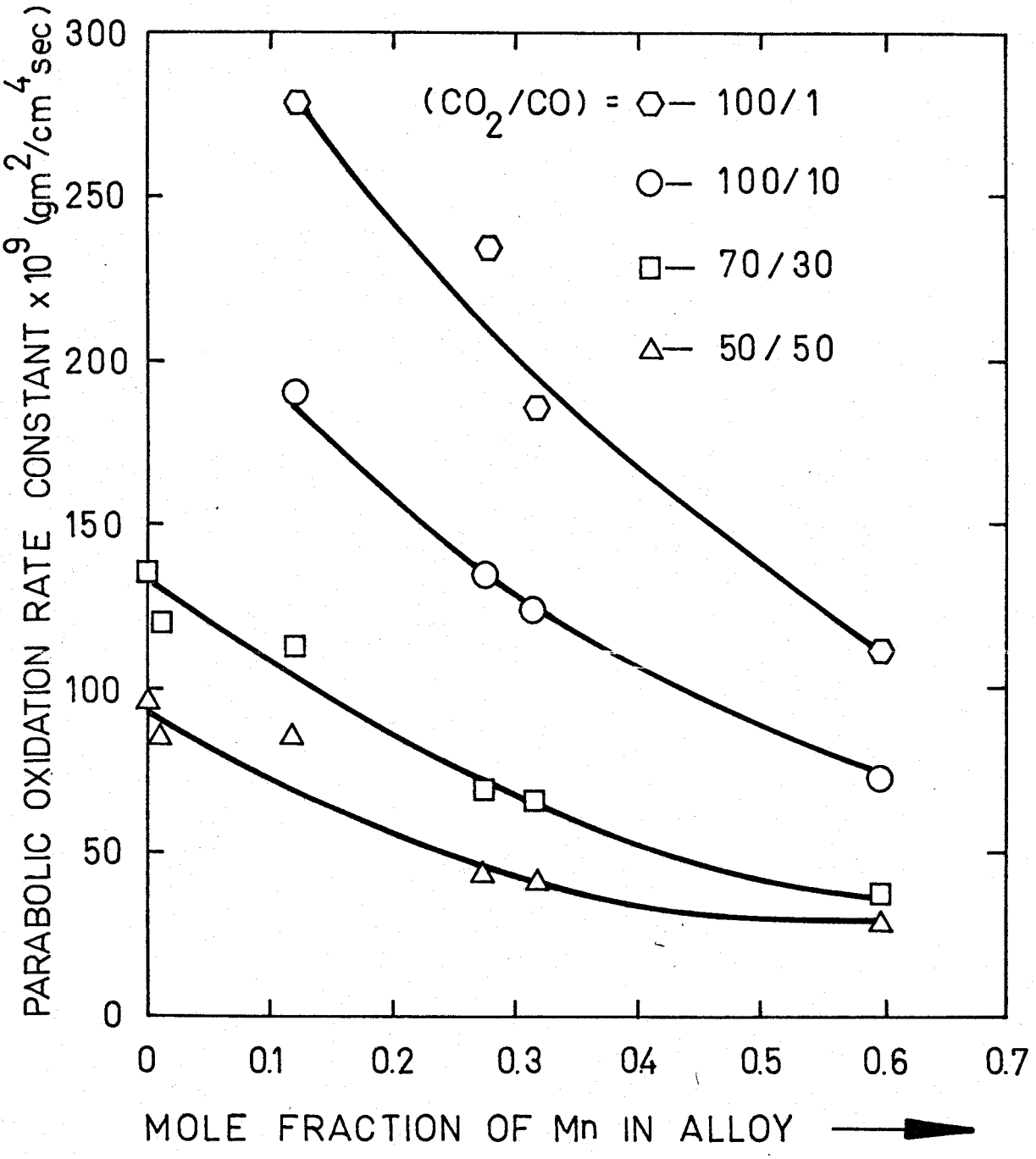

Figure 6.8 Parabolic Oxidation Constant as a Function of Mn Constant in Fe-Mn Alloys.

Table 6.3

Least Square Approximations for Parabolic Oxidation Constants as a Function of C_{Mn} (w/o Mn in alloy) in Fe-Mn Alloys

$$k_p = A\, C_{Mn}^3 + B\, C_{Mn}^2 + C_{CMn} + D$$

Oxidizing Atmosphere 1 atm Total Pressure CO_2/CO [w/o]	Calculated Constants for Polynomial of the Third Degree	
100/1	A	-8.7142×10^{-7}
	B	$+1.4092 \times 10^{-6}$
	C	-2.1331×10^{-7}
	D	$+2.3045 \times 10^{-7}$
100/10	A	-1.9744×10^{-7}
	B	$+2.7654 \times 10^{-7}$
	C	-1.0779×10^{-7}
	D	$+1.8753 \times 10^{-7}$
70/30	A	-4.5387×10^{-8}
	B	$+1.7343 \times 10^{-7}$
	C	-2.5688×10^{-7}
	D	$+1.3051 \times 10^{-7}$
50/50	A	-1.1727×10^{-7}
	B	$+2.6195 \times 10^{-7}$
	C	-2.4123×10^{-7}
	D	$+9.8104 \times 10^{-8}$

explained by a large decrease in diffusion rate in spite of the increase in oxygen potential drop across the oxide scale. The variation of the k_p's for the same alloy with a change in oxidizing atmosphere may be due to a change in the oxygen potential drop across the scale and diffusivity of cations in scale. Increased oxygen potential in the oxidizing atmosphere increases values of both factors.

In general, the parabolic oxidation rate constant is a function of a number of variables such as oxygen potential in the reaction gas, the concentration and mobilities of moving species, and concentration profiles of the alloying elements in the alloy and in the oxide, respectively. It has been emphasized in Chapter II, that it is very difficult to obtain an analytical solution from the theoretical approach provided even when all required data are available. For the FeO-MnO system, the required data are not available to describe the transport properties and type of defects in the scales. Hence, the desired calculations may not be carried out without obtaining additional data which is out of the scope of this work. Accordingly, the values of the parabolic oxidation constants have been only empirically represented as a function of alloy composition by polynomials of different degrees. The computer was employed in order to calculate the best fit curves using the least square method. A polynomial of the third degree was the most suitable mathematically and the coefficients of correlation were within .95 and .98. The calculated polynomials are listed in Table 6.3. The numerical values of the k_p's calculated for the different oxygen potentials and bulk alloy concentrations of manganese are represented as solid curves in Fig. 6.8.

6.3 Self-Diffusion Coefficients of Cations in FeO-MnO Solid Solutions

It is possible to obtain information on the transport properties and defect properties of FeO-MnO solid solutions at 1000°C from the experimental values of the parabolic oxidation constants. The equations derived by Wagner[14] in the theoretical treatment of the concentration profiles in scales during alloy oxidation previously outlined in Chapter II may be utilized with the experimental data obtained from the present experiments to calculate the self-diffusion coefficients of cations in the FeO-MnO solid solutions. It is expected that the self-diffusion coefficients will be functions of the oxide compositions and oxygen potentials at constant temperature.

If all conditions of Wagner's[14] analysis are satisfied, it is possible to start with equation (2.19) for the FeO-MnO system

$$D_{Fe}\,(1-\xi)\left(-\frac{\partial \ln \partial_{FeO}}{\partial \xi}\,\frac{d\xi}{dy}+\frac{Z_{Fe}}{Z_o}\,\frac{d \ln a_o}{dy}\right)+$$

$$+\,D_{Mn}\,\xi\left(-\frac{\partial \ln a_{MnO}}{\partial \xi}\,\frac{d\xi}{dy}+\frac{Z_{Mn}}{Z_o}\,\frac{d \ln a_o}{dy}\right)=k \qquad (6.8)$$

where ξ is the mole fraction of MnO in the oxide and y is the standardized scale thickness. Using the Gibbs-Duhem equation for the continuous solid solution

$$(1-\xi)\,\partial \ln a_{FeO}+\xi\,\partial \ln a_{MnO}=0 \qquad (6.9)$$

Rearrangement yields

$$\partial \ln a_{FeO} = - \frac{\xi}{1-\xi} \partial \ln a_{MnO} \tag{6.10}$$

Consequently, equation (6.8) may be placed in the form

$$D_{Fe} (1-\xi) \left(\frac{\partial \ln a_{MnO}}{\partial \xi} \cdot \frac{\xi}{1-\xi} \cdot \frac{d\xi}{dy} + \frac{Z_{Fe}}{Z_o} \frac{d \ln a_o}{dy}\right) +$$

$$+ D_B \xi \left(- \frac{\partial \ln a_{MnO}}{\partial \xi} \cdot \frac{d\xi}{dy} + \frac{Z_{Mn}}{Z_o} \frac{d \ln a_o}{dy}\right) = k \tag{6.11}$$

The FeO-MnO solid solution may be considered to be nearly ideal in view of data by Foster and Welch[34]. Accordingly

$$\frac{\partial \ln a_{MnO}}{\partial \ln \xi} = 1 \tag{6.12}$$

and

$$\partial \ln \xi = \frac{1}{\xi} \partial \xi \tag{6.13}$$

Substituting (6.13) into (6.12) yields

$$\frac{\xi \partial \ln a_{MnO}}{\partial \xi} = 1 \tag{6.14}$$

from which we obtain

$$\partial \ln a_{Mn(O)} = \partial \ln \xi = \frac{1}{\xi} \partial \xi \tag{6.15}$$

If the relation $|Z_{Fe}|=|Z_{Mn}|=|Z_O| = 2$ is valid, we can write equation (6.5) upon subsitituing in (6.15) and (6.16) in the form

$$D_{Fe}\,(1-\xi)\,\left(\frac{1}{1-\xi}\frac{d\xi}{dy} + \frac{d\ln a_o}{dy}\right) +$$

$$+ D_{Mn}\,\xi\,\left(-\frac{1}{\xi}\frac{d\xi}{dy} + \frac{d\ln a_o}{dy}\right) = k \qquad (6.17)$$

Upon rearranging equation (6.17) and substituting for

$$k = k'\ D_{Fe} \quad \text{and} \quad p = \frac{D_{Fe}}{D_{Mn}} \qquad (6.18) \text{ and } (6.19)$$

$$(1-p)\frac{d\xi}{dy} + \frac{d\ln a_o}{dy}\ [(1-\xi) + p\xi\ ] = k' \qquad (6.20)$$

The electron microprobe determinations have demonstrated that the profiles of metal in the oxide scales were stationary and very flat under conditions for steady state oxidation of the alloys. Also, the profiles in the scale could be approximated by a linear relationship

$$\xi = a + by \qquad (6.21)$$

where $a = \xi$ is the mole fraction of MnO in the scale at its inner interface and b is the gradient across the oxide. Accordingly,

$$\frac{d\xi}{dy} = b = \text{constant} \qquad (6.22)$$

Equation (6.14) therefore could be written as

$$(1-p)b + \frac{d \ln a_o}{dy}[(1-\xi) + p\xi] = k' \qquad (6.23)$$

and rearrangement yields

$$\frac{d \ln a_o}{dy} = \frac{k' + (p-1)b}{1 + (p-1)\xi} \qquad (6.24)$$

The second equation which could be utilized in this calculation from Wagner's analysis[14] is the algebraic expression (2.26)

$$- D_{Mn}\left[\left(\frac{\partial \ln a_{MnO}}{\partial \xi} \cdot \frac{d\xi}{dy} - \frac{d \ln a_o}{dy}\right)\right]_{y=1} = \xi'' k \qquad (2.26)$$

Upon applying the same simplifications as in the previous case, the resulting expression is

$$k' = p \frac{d \ln a_o}{dy} - \frac{pb}{\xi''} \qquad (6.25)$$

Substitution of equation (6.24) into (6.25) yields

$$k' = \frac{p_k + pb\,(p-1)}{1 + \xi''\,(p-1)} - \frac{pb}{\xi''} \qquad (6.26)$$

Upon rearrangement, equation (6.26) may be written

$$k' = \frac{pb}{(p-1)(1-\xi'')\xi''} \qquad (6.27)$$

Substitution of equation (6.18) into (6.27) yields

$$D_{Fe} = \frac{k\xi''\ (p-1)(1-\xi'')}{pb} \tag{6.28}$$

and from equations (6.19) and (6.27)

$$D_{Mn} = \frac{k\xi''\ (p-1)(1-\xi'')}{b} \tag{6.29}$$

The oxidation constant k may be related to k_p by the expression

$$k = \frac{k_p}{2} (V \times 16)^2\ cm^2/sec \tag{6.30}$$

where V is the molar volume of the mixed oxide.

In order to carry out the calculations for self-diffusion coefficients, certain assumptions and approximations must be made. Parabolic oxidation in the followed region is considered as steady state, which means that the values p and ξ'' for a particular alloy and oxygen potential should not change with time. There is experimental evidence that this is so. Because the variations of b and ξ'' with oxygen potential at the outer interface for a given alloy are very small, these terms would be regarded as constant to a first approximation. The value of b was approximated to from the concentration profiles in the scales and the ξ'' listed in Tables 6.4 and 6.5. Values of b are in Table 6.3a.

Sheil and Kiwit[35] consider that the diffusivity of Fe and Mn in an FeO-MnO oxide are of approximately the same magnitude because of the even distribution of iron and manganese cations in a scale upon the

Table 6.3a

Parameter b

Parameter b (slope of MnO profiles in oxide) X 10^{-4}					
Oxidation Atmospheres v/o [CO_2/CO] \ Alloy Composition w/o [Mn]	0.93	12.33	27.35	31.83	59.04
50/50	-0.93 x ± .23 x	-12.33 ± 3.46	-27.01 ± 6.84	-31.45 ± 3.95	-59.23 ± 4.01
70/30	-0.92 x ± .29 x	-12.01 ± 2.97	-27.85 ± 7.01	-31.89 ± 8.05	-53.31 ± 9.05
100/10	/	-12.64 ± 2.53	-27.21 ± 6.34	-31.21 ± 4.98	-59.14 ± 6.58
100/1	/	-12.80 ± 3.94	-27.73 ± 3.95	-31.68 ± 6.05	-59.01 ± 2.73

oxidation of Fe-Mn alloys. In the present investigation, the distribution of cations in scales shows that the iron has a slightly higher diffusivity than manganese, since a small increase of FeO content was found in a scale towards the outer interface. Accordingly, the estimated value of ratio D_{Fe}/D_{Mn} is more but very close to one, approximately 1.01. From the experimental values of k_p (Table 6.3), microprobe determinations and the estimated value of p, the self-diffusion coefficients of Fe and Mn were calculated, and their dependences on the oxide composition determined. The results of these calculations for different oxygen potentials are listed in Tables 6.4 and 6.5 and illustrated in Figs. (6.9 and 6.10).

There are not available data in the literature with which the calculated values from the present work could be compared except for pure FeO. The value for the self-diffusion coefficient of iron in FeO for an oxygen potential given by CO_2/CO = 50/50 is 2.923×10^{-8} cm^2 sec^{-1} and for CO_2/CO = 70/30 is 4.030×10^{-8} cm^2 sec^{-1} [56]. These values are illustrated in Fig. (6.9) by triangular and rectangular symbols, respectively. The calculated values from the present work are consistent with the values from the literature. Addition of MnO to FeO noticeably decreases the diffusion rate of both cations. The diffusion rate in the oxides forming a continuous solid solution is a function of numerous factors which are at the present time not clearly defined. However, this very complex problem may be simplified by proper assumptions in order that our experimental results may be used to gain more detailed understanding of the properties of the FeO-MnO oxide solid solution.

Table 6.4

Self-Diffusion Coefficients of Iron at 1000°C in the FeO-MnO Solid Solution. (cm^2/sec)

Mole Fraction of MnO in Oxide ξ"	Atmosphere CO_2CO [volume/o]			
	50/50	70/30	90/10	100/1
0.000	2.954×10^{-8}	4.106×10^{-8}	-	-
.00981	2.705×10^{-8}	3.841×10^{-8}	-	-
.118	2.114×10^{-8}	2.994×10^{-8}	5.52×10^{-8}	7.997×10^{-8}
.271	1.244×10^{-8}	1.746×10^{-8}	3.244×10^{-8}	5.003×10^{-8}
.314	9.921×10^{-9}	1.459×10^{-8}	2.783×10^{-8}	4.139×10^{-8}
.584	3.143×10^{-9}	4.118×10^{-9}	9.98×10^{-9}	1.699×10^{-8}

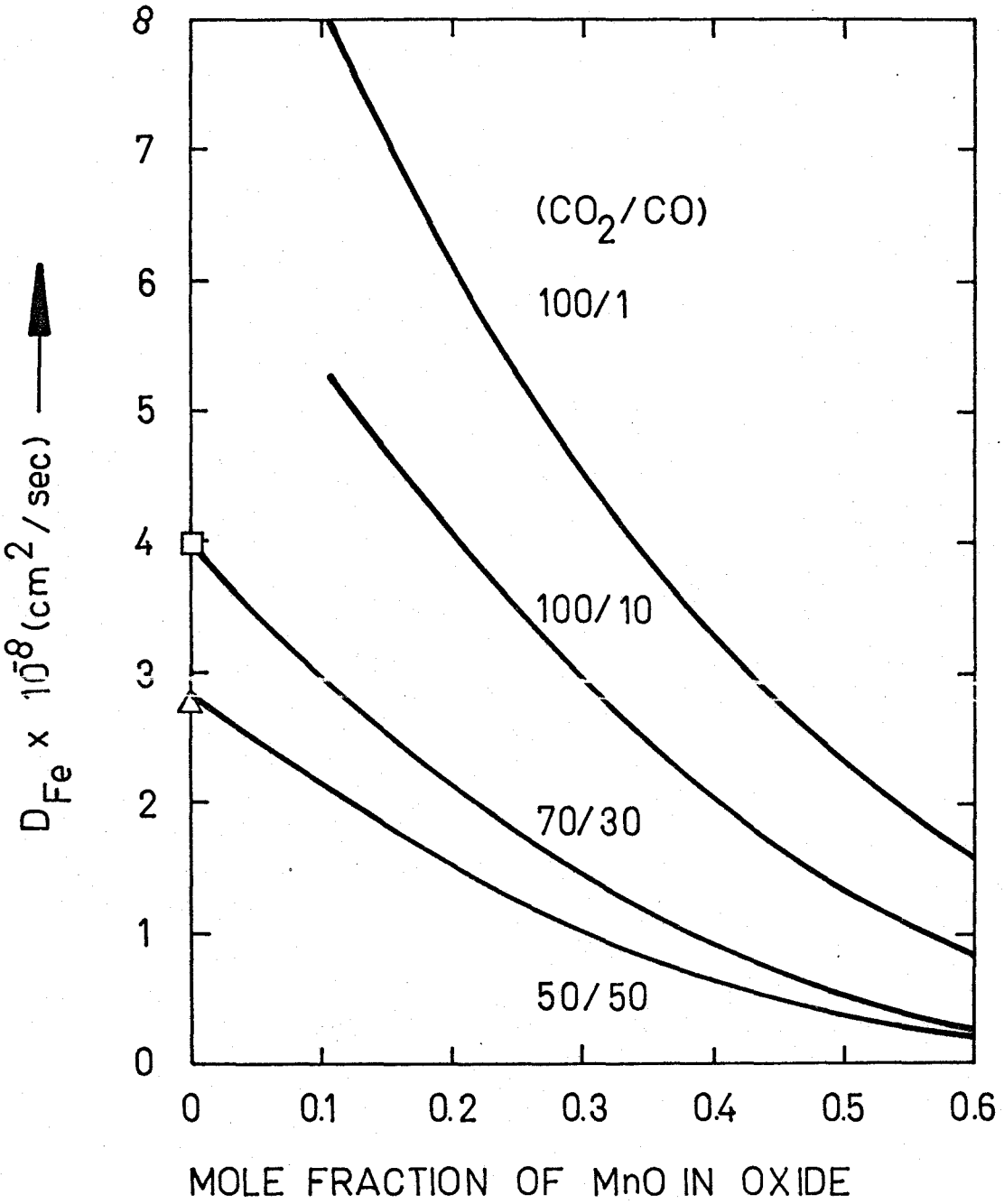

Figure 6.9 Self-Diffusion Coefficient of Iron as a Function of MnO Content in the FeO-MnO Solid Solution at 1000°C.

Table 6.5

Self-Diffusion Coefficients of Manganese at 1000°C in the FeO-MnO Solid Solution (cm^2/sec)

Mole Fraction of MnO in Oxide ξ''	Atmosphere CO_2/CO [v/o]			
	50/50	70/30	90/10	100/1
.00981	2.678×10^{-8}	3.802×10^{-8}	-	-
.1188	2.092×10^{-8}	2.964×10^{-8}	5.467×10^{-8}	7.917×10^{-8}
.271	1.244×10^{-8}	1.728×10^{-8}	3.212×10^{-8}	4.953×10^{-8}
.314	9.821×10^{-9}	1.444×10^{-9}	2.755×10^{-8}	4.098×10^{-8}
.584	3.112×10^{-9}	4.076×10^{-9}	9.88×10^{-9}	1.699×10^{-8}

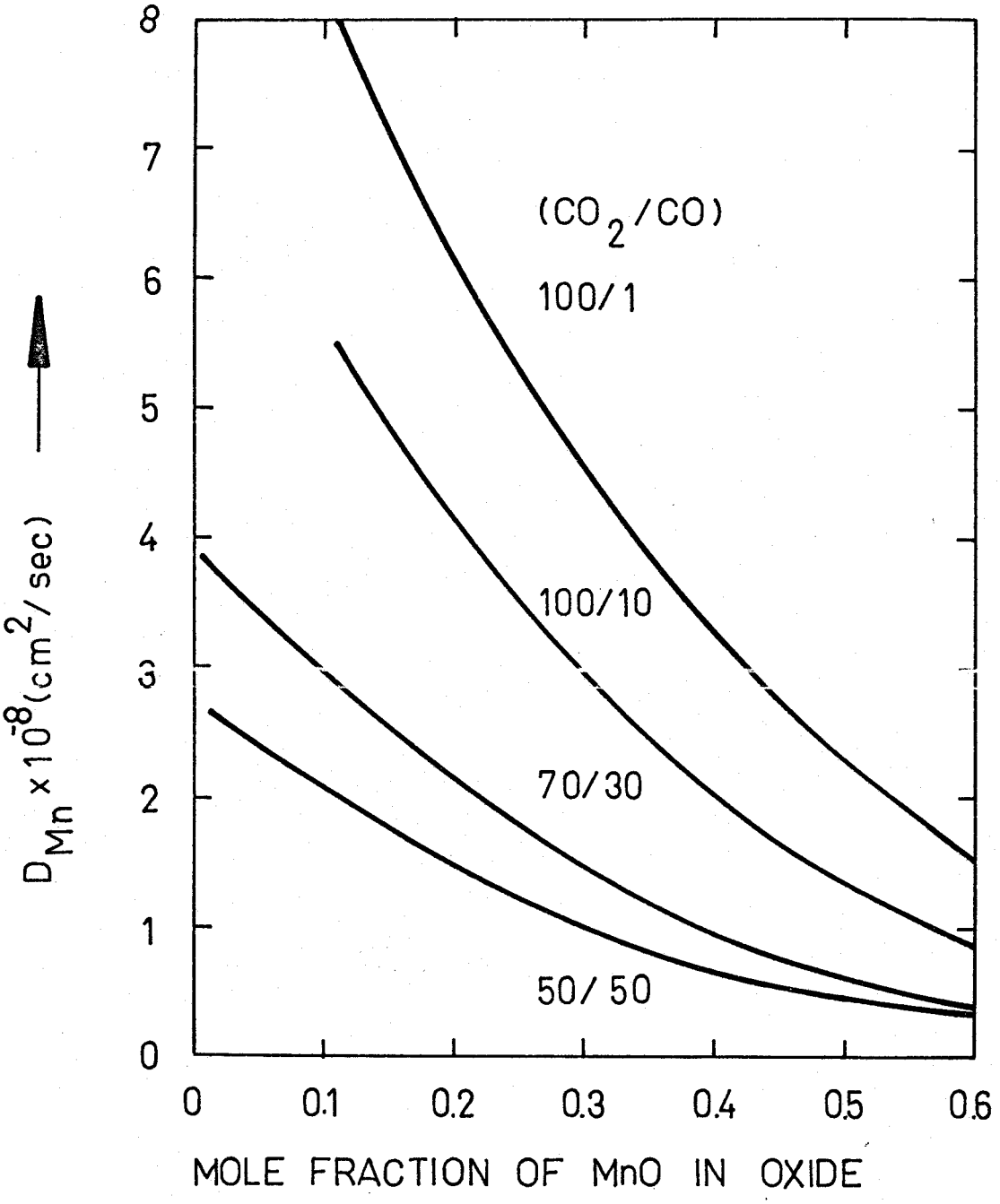

Figure 6.10 Self-Diffusion Coefficient of Manganese as a Function of MnO Content in the FeO-MnO Solid Solution at 1000°C.

6.4 Concentration and Type of Defects in FeO-MnO Solid Solutions

It is generally agreed that the transport of Fe and Mn in FeO and MnO scales takes place via cation vacancies[10,17]. In both, pure FeO and pure MnO, the metal deficit corresponds to the presence of cation vacancies and electron holes. Although information is not available on FeO-MnO solid solutions, it is expected that the type of defects occurring in the pure oxides is preserved in solution. It has been found[42], in general, for two oxides forming a continuous solid solution, that the concentration of defects changes with composition for a given oxygen potential in an exponential manner. Wagner[57] has suggested that the mole fraction of cation vacancies in a metal deficit oxide solid solution is a function of oxide composition and oxygen activity. The suggested empirical relationship for FeO-MnO may be written as

$$\log x_{\square} = \log x^{FeO} + \xi \log (x_{\square}^{MnO} / x_{\square}^{FeO}) + \log a_o^{1/\nu} \qquad (6.31)$$

where $a_o \equiv [P_{O_L}\ (atm)]^{\frac{1}{2}}$, $x_{\square}^{FeO}$ and $x_{\square}^{MnO}$ are the vacancy mole fraction at particular oxygen potential in FeO and MnO respectively and ν is a coefficient. As was mentioned, there are no literature references on the defect concentrations in FeO-MnO solid solutions. For this reason the coefficients in expression (6.31) are not known and the change in concentration of the defects with change in composition of the FeO-MnO solid solutions can not be obtained. However, these concentrations could be calculated from self-diffusion coefficients obtained by the calculations presented in the previous section of this chapter. Since the diffusivities of Fe and Mn cations in FeO-MnO solid solutions are almost equal, the relation between the self-

diffusion coefficients and concentrations of defects may be approximated by[57]

$$D_{Fe} = D^{\circ}_{Fe} \frac{x_{\square}}{x^{FeO}_{\square}} \tag{6.32}$$

where $D^{\circ}_{Fe} = D_{Fe}$ (in pure FeO at constant oxygen pressure)

$x_{\square}$ is the concentration of defects in the FeO-MnO solution

and similarly,

$$D_{Mn} = D^{\circ}_{Mn} \frac{x_{\square}}{x^{MnO}_{\square}} \tag{6.33}$$

where $D^{\circ}_{Mn} = D_{Mn}$ (in pure MnO at constant oxygen pressure).

Utilizing equation (6.32) and diffusivity data calculated from the thermogravimetric experiments (Tables 6.4 and 6.5), the required concentration change could be obtained. In order to carry out the calculations, the ratio $D^{\circ}_{Fe}/x^{FeO}_{\square}$ is required, which is the mobility of the migrating species in the oxide phase under given oxygen potential and temperature. For an atmosphere containing CO_2/CO = 70/30 the oxygen potential at 1000°C is 4.06×10^{-15} atm[44] and the corresponding self-diffusion coefficient of Fe in FeO is 4.03×10^{-8} cm^2 sec^{-1} [56]. The measured concentration of defects in pure FeO[17] for this oxygen potential is .105 in mole fraction. From these data and D_{Fe}'s from Table 6.4, the change in defect concentration with composition of FeO-MnO was calculated. The numerical values of $x_{\square}$ are listed in Table 6.6 and illustrated in Fig. 6.11 by circular symbols. The same calculation was carried out for CO_2/CO = 50/50 atmosphere. The $D^{\circ}_{Fe} = 2.923 \times 10^{-8}$ cm^2 sec^{-1} and the corresponding concentration of defects is .07615 in mole fraction. The

Table 6.6

Calculated Values of Defect Concentration from Present Investigation

Mole Fraction of MnO in Oxide	Mole Fraction of Defects in Oxide	$1-x_{MnO}-2x_{\square}$	log $(1-x_{MnO}-2x_{\square})$	$1-x_{MnO}-3x_{\square}$	log $(1-x_{MnO}-3x_{\square})$
Atmosphere CO_2/CO = 50/50 [v/o]					
0.000	0.0852	0.8296	-0.08145	0.7449	-0.1281
0.0098	0.0835	0.8232	-0.0798	0.7397	-0.1310
0.118	0.0551	0.7718	-0.1125	0.7167	-0.1447
0.271	0.0327	0.6636	-0.1780	0.6309	-0.2001
0.314	0.0258	0.6344	-0.1977	0.6086	-0.2157
0.584	0.0081	0.3998	-0.3981	0.3917	-0.4071
Atmosphere CO_2/CO = 70/30 [v/o]					
0.000	0.1090	0.7820	-0.1067	0.6730	-0.1737
0.0098	0.1089	0.7724	-0.1129	0.6635	-0.1783
0.118	0.0779	0.7718	-0.1125	0.6483	-0.1883
0.271	0.0454	0.6636	-0.1780	0.5928	-0.2271
0.314	0.0380	0.6344	-0.1977	0.5420	-0.2660
0.584	0.0107	0.3998	-0.3981	0.3839	-0.4158

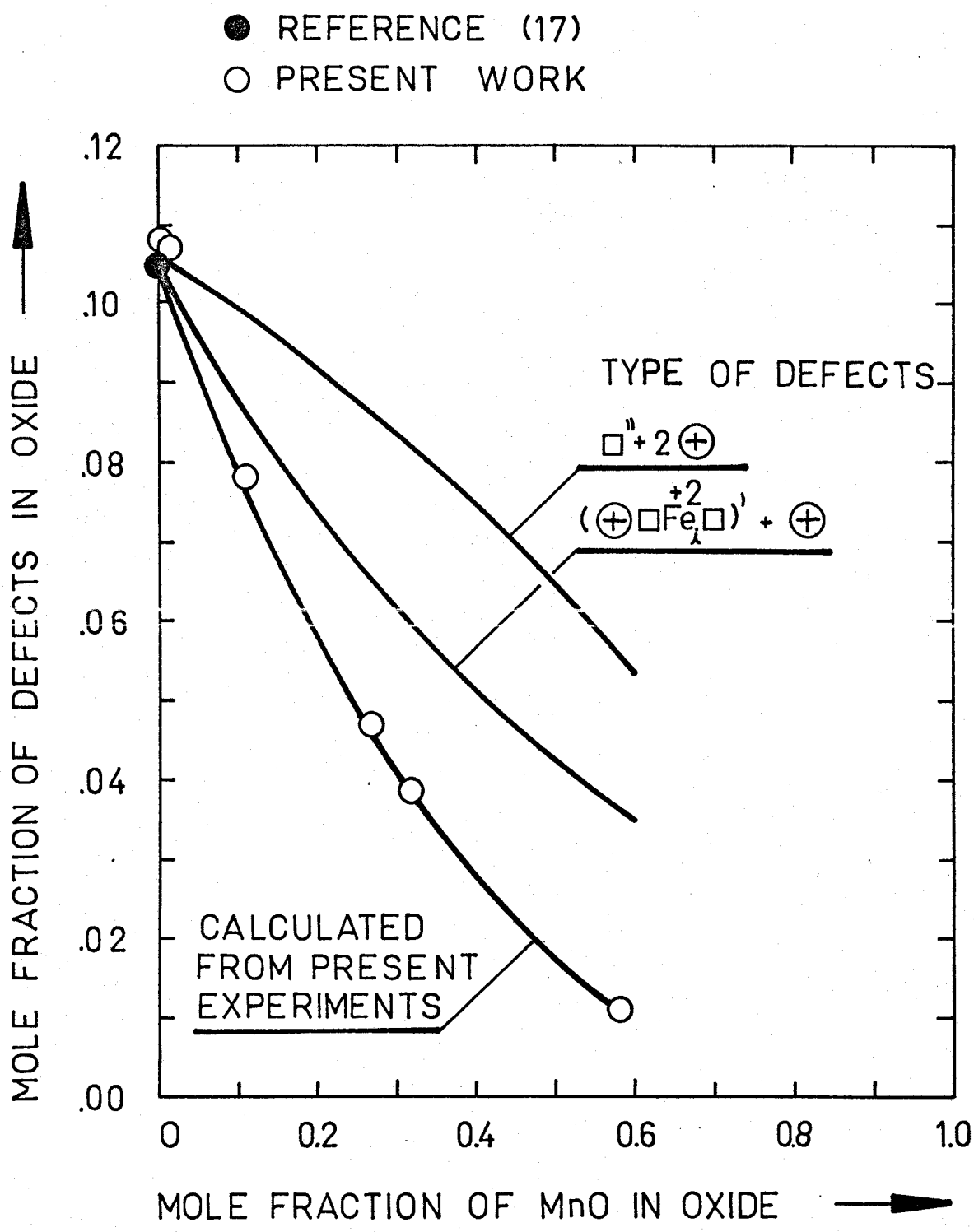

Figure 6.11. Variation of Concentration of Defects in FeO-MnO solid solutions in CO_2/CO = 70/30 Atmosphere.

results of the calculation are listed in Table 6.6 and illustrated in Fig. 6.12 by circular symbols.

In order to assess the type of defects in an FeO-MnO solid solution the defect concentrations calculated from this present experimental work will be compared with the concentrations of defects calculated by assuming two different defect models. It has been assumed[41] that defects in an FeO-MnO solid solution are present as double charged vacancies and completely dissociated positive holes. The defect equation for pure wustite may then be written,

$$2\ Fe^{+2} + \frac{1}{2}\ O_2 \rightarrow \square'' + 2\oplus + O^{=} \qquad (6.34)$$

Addition of Mn^{+2} cations to form an FeO-MnO solid solution is assumed not to change the conditions for electrical neutrality. Because the energetic barrier for formation of Mn^{+3} from Mn^{+2} is much higher than for Fe^{+3} from $Fe^{=2}$, the bivalent manganese cations are mainly present. This condition implies that they do not participate to any significant extent in the reaction for defect formation in the presence of Fe^{+2} ions. Their presence in the cation lattice also serves to decrease by dilution the concentration of Fe^{+2}-ions and accordingly the concentration of defects. If the defects are not affected by the surrounding ionic species within the lattice, equation (6.34) could be used to calculate the defect concentration in the FeO-MnO solid solution.

Application of the mass action law yields

$$K_1 = \frac{x_{\square}\ x_{\oplus}^2}{x_{Fe^{+2}}^2\ P_{O_2}^{\frac{1}{2}}} \qquad (6.35)$$

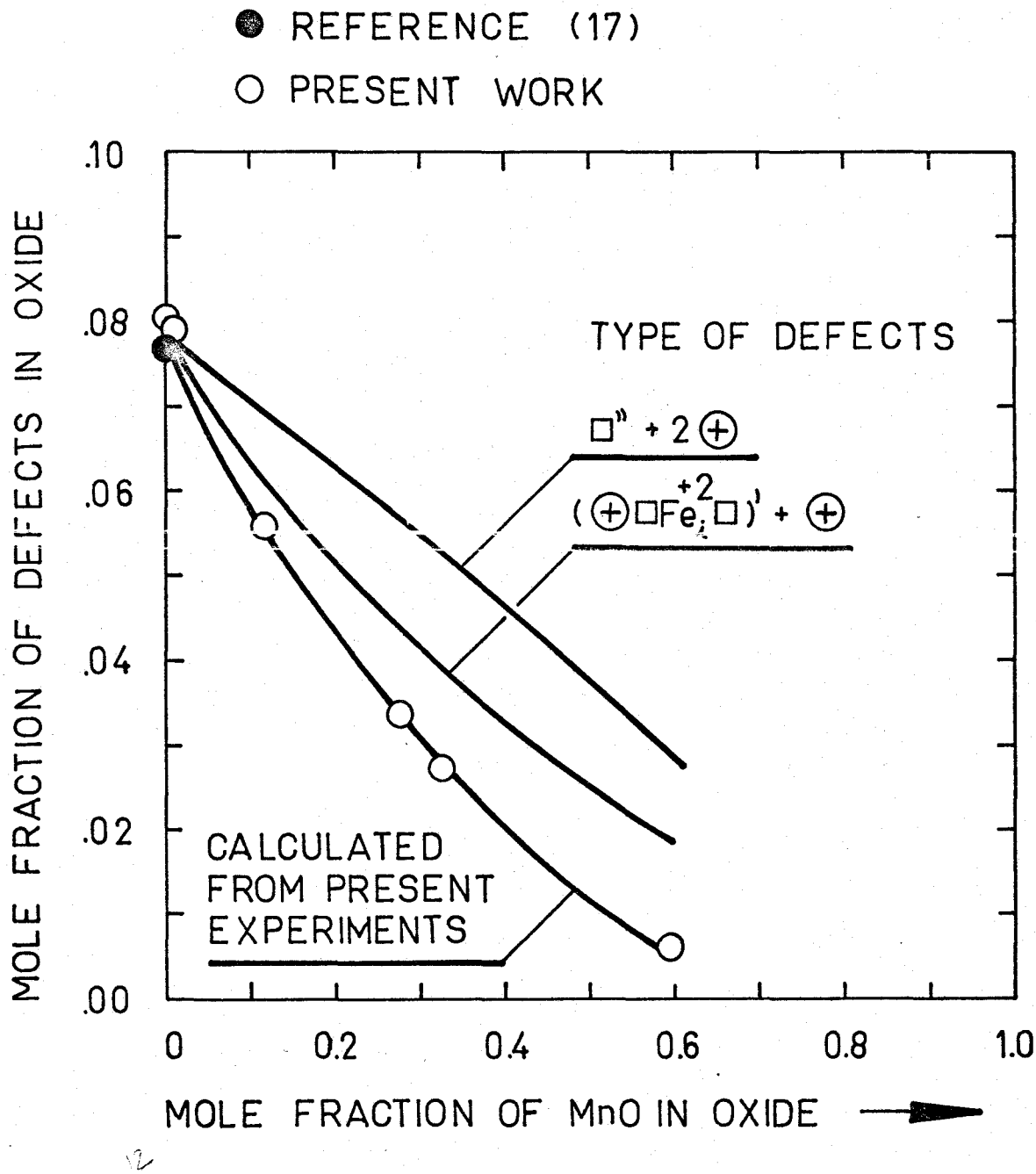

Figure 6.12. Variation of Concentration of Defects in FeO-MnO Solid Solution in CO_2-CO = 70/30 Atmosphere.

where

$$2\, x_{\square} = x_{\oplus} \tag{6.36}$$

and

$$x_{Fe^{+2}} = 1 - x_{MnO} - 2\, x_{\square} \tag{6.37}$$

Rearrangement and substitution of equations (6.36) and (3.37) into equation (6.35) yields

$$x_{\square} = \left(\frac{K_1}{4}\right)^{1/3} \cdot P_{O_2}^{1/6} \cdot (1 - x_{MnO} - 2x_{\square})^{2/3} \tag{6.38}$$

In this case K_1 is a function of temperature only[41] and is independent of the MnO content in the oxide solid solution. Using equation (6.35) and the concentration of defects for FeO from the literature[17] the K_1's were calculated for CO_2/CO = 50/50 and 70/30 atmospheres. Then by the help of equation (6.38) the change in defect concentration with MnO content in the solid solution was calculated. The numerical values are represented in Figs. 6.11 and 6.12.

Because of the high concentration of lattice defects in wustite several investigators have recently postulated the occurrence of defect complexes to account for its non-stoichiometry. Kofstad and Hed[52] invented the defect model for wustite which has been discussed in Chapter III. The defects are complexes formed by two vacancies and an interstitial ferrous cation on a tetrahedral site. This complex could be neutral associated with two electron holes (Ferric cations) or singly charged and associated only with one electron hole. Kofstad and Hed[52] have demonstrated that

at 1000°C the experimental data obtained by Valet and Raccah[20] are in good agreement with theoretically calculated results assuming the single charged defect complex. Accordingly the defect equation could be written as

$$2\ Fe^{+2} + V_i + \frac{1}{2} O_2 \rightarrow Fe_c^{'} + \oplus + O_o \qquad (6.39)$$

With the same assumptions as in the previous case, the concentration of defects is

$$x_c = K_2^{\frac{1}{2}} \cdot P_{O_2}^{\frac{1}{4}} \cdot x_{Fe^{+2}} \cdot x_{V_i}^{\frac{1}{2}} \qquad (6.40)$$

where

$$x_{Fe^{+2}} = 1 - 3\,x_c - x_{MnO} \qquad (6.41)$$

and

$$x_{V_i} = [2(1 - x_{MnO}) - 7\,x_c] \qquad (6.42)$$

The concentration of complexes is equal to the vacancy concentration responsible for the non-stoichiometry of oxide. This value could be compared with the concentration of vacancies calculated from equation (6.32). Hence

$$x_c = x_{\square} \text{ (due to non-stochiometry)} = \text{mole fraction of defects} \qquad (6.43)$$

Using equations (6.40), (6.41), (6.42) and (6.43) and the same computational procedure as for the first model, the change in concentrations of defects

with change of composition of FeO-MnO solid solution was calculated. Numerical values are illustrated in Fig.'s 6.11 and 6.12.

The values deduced from the two theoretical models and the calculated values from the experimental results are not in good agreement. The findings, however, indicate that the defects in FeO-MnO solid solutions would possibly be of a complex type since the curve calculated from this theoretical model approximates most closely the values calculated from present investigations at all manganese compositions. It is emphasized that the representation of the actual relations in the FeO-MnO system by the above theoretical models is limited by the simplifications and assumptions used in this analysis. Accordingly the factors representing interactions between the defects and the effects arising from the change in the kind of cations surrounding the defects in the lattice due to addition of the alloying element may cause the discrepancies between the actual situation and the ideal theoretical model.

Zintl[42] has advanced a more detailed methodology to account for the dependence of defect concentrations on the composition of the solid solution of the two oxides. He measured the concentration of defects in CoO-MgO and CoO-NiO solid solution and proposed that the decrease in concentration of defects by addition of MgO to CaO was due to two factors. There is a dilution effect since Mg^{+2} ions substitute for Co^{+2} in the lattice and accordingly decrease the concentration of defects. There is an additional strong effect of increased concentration of Mg^{+2} ions causing a decrease in concentration of defects due to an alternation of the surroundings within the lattice about a defect. Zintl[42] explains

the second effect as follows. In pure CoO each Co^{+3} ion is surrounded by 12 nearest Co^{+2} neighbours if the defects are statistically distributed in the lattice. If the energetic potential barrier between cations is not very high and wide, one obtains a decrease of the electron energetic states by means of resonance and accordingly stabilization of the trivalent state. This resonance is distorted by substitution of $Co^{2}+$ by Mg^{+2} ions and consequently the trivalent state is less stable. The trivalent state of magnesium could be reached only by overcoming a much higher energetic barrier than in the case of cobalt because an electron has to be removed from the inner electron shell which has the configuration of an inert gas. This explanation is applicable in general for systems involving a continuous solid solution of oxides of similar type. To describe the changes in concentration of defects, Zintl[42] invented a theoretical treatment of the problem on the basis of statistical thermodynamics. According to him the equilibrium constants for reactions involving formation of defects are functions of the additional element content in the oxide solid solution. This arises when the equilibrium constants are expressed in terms of concentrations rather than activities. If the reaction is in equilibrium the standard free energy change of oxygen dissolution in oxide is

$$\Delta G^\circ = - RT \ln K \tag{6.44}$$

Accordingly the change in K causes change in ΔG°.

$$\Delta G^\circ_{(x_{BO})} - \Delta G^\circ_{(x_{BO}=0)} = - RT \ln \frac{K_{(x_{BO})}}{K_{(x_{BO}=0)}} \tag{6.45}$$

where $\Delta G^{\circ}_{(x_{BO}=0)}$ - standard free energy change for pure oxide AO.

$\Delta G^{\circ}_{(x_{BO})}$ - standard free energy change for AO-BO solid solution at particular concentration of BO.

similarly $K_{(x_{BO}=0)}$ - equilibrium constant for reaction of pure AO with oxygen.

$K_{(x_{BO})}$ - equilibrium constant for reaction of AO-BO with oxygen.

He employed equation (6.45) to obtain functional relationships to describe experimental results.

This type of representation of experimental results may be employed for the system FeO-MnO. Rearrangement of equation (6.45) yields

$$\Delta G^{\circ}_{(x_{MnO})} - \Delta G^{\circ}_{(x_{MnO}=0)} = - RT \ln K_{(x_{MnO})} + \\ + RT \ln K_{(x_{MnO}=0)} \qquad (6.46)$$

where $RT \ln K_{(x_{MnO}=0)}$ is constant at a given oxygen potential. Hence,

$$\Delta(\Delta G^{\circ}) = A - RT \ln K_{(x_{MnO})} \qquad (6.47)$$

where

$$A = RT \ln K_{(x_{MnO}=0)}$$

$$\Delta(\Delta G^{\circ}) = \Delta G^{\circ}_{(x_{MnO})} - \Delta G^{\circ}_{(x_{MnO}=0)}$$

Substitution of rearranged equation (6.35) and equation (6.40) into equation (6.47) yield for the model assuming defects present as doubly changed vacancies and two positive holes,

$$\Delta(\Delta G_1^\circ) = A_1 - 3\ RT\ \ln x_{\square} + 2\ RT\ \ln (1 - x_{MnO} - 2\ x_{\square}) \qquad (6.48)$$

and for the model assuming complex defects,

$$\Delta(\Delta G_2^\circ) = A_2 - 2\ RT\ \ln x_c + 3\ RT\ \ln (1 - x_{MnO} - 3\ x_c) \qquad (6.49)$$

The subscripts 1 and 2 refer to the particular model.

Equations (6.48) and (6.49) may be used to obtain simple relationships for the concentrations of defects, vacancies or complexes as a function of the mole fraction of MnO in the oxide scale.

Rearrangement of equation (6.48) gives

$$\log x_{\square} = B_1 - G_1 \Delta(\Delta G_1^\circ) + D_1 \log (1 - x_{MnO} - 2\ x_{\square}) \qquad (6.50)$$

where

$$B_1 = \frac{A_1}{6.9\ RT}$$

$$C_1 = \frac{1}{6.9\ RT}$$

$$D_1 = \frac{2}{3}$$

Similarly, rearrangement of equation (6.49) gives

$$\log x_c = B_2 - C_2\ \Delta(\Delta G_2^\circ) + D_2 \log (1 - x_{MnO} - 3\ x_c) \qquad (6.51)$$

where

$$B_2 = \frac{A_2}{4.6\ RT}$$

$$C_2 = \frac{1}{4.6\ RT}$$

$$D_2 = \frac{3}{2}$$

From equations (6.50) and (6.51), it is possible to calculate the concentration of defects provided that $\Delta(\Delta G^\circ)$ and the concentration $(x_{MnO})\ x_C$ are known. Auxiliary functions $\Delta(\Delta G^\circ) = f\ (x_{MnO})$ and $\log x_{FeO} = f\ (x_{MnO})$ could be obtained from the present experimental results. Using the values of the defect concentration calculated from equation (6.32) as a function of MnO concentration in the oxide for given pressures and equations (6.34) and (6.39) for the two different models, values for the equilibrium constants were calculated. Obtained values of K's as a function of MnO content in the oxide and equation (6.45) enabled calculation of the change in ΔG° as a function of MnO content in solid solution. Numerical values calculated assuming the single vacancy model are illustrated in Fig. 6.13. The circles represent the values at the compositions used in this experimental work. Similarly, the values calculated assuming the complex model are illustrated in Fig. 6.14 The plots show that the change in ΔG° of the FeO-MnO solid solution with increasing concentration of MnO follows a simple linear relationship almost up to $x_{MnO} = .5$. The empirical relations obtained could be represented for oxygen potential.

$$CO_2/CO = 50/50 \text{ by } \Delta(\Delta G_1^\circ) = 25.1\ x_{MnO}\ [\text{k cal}] \qquad (6.52)$$

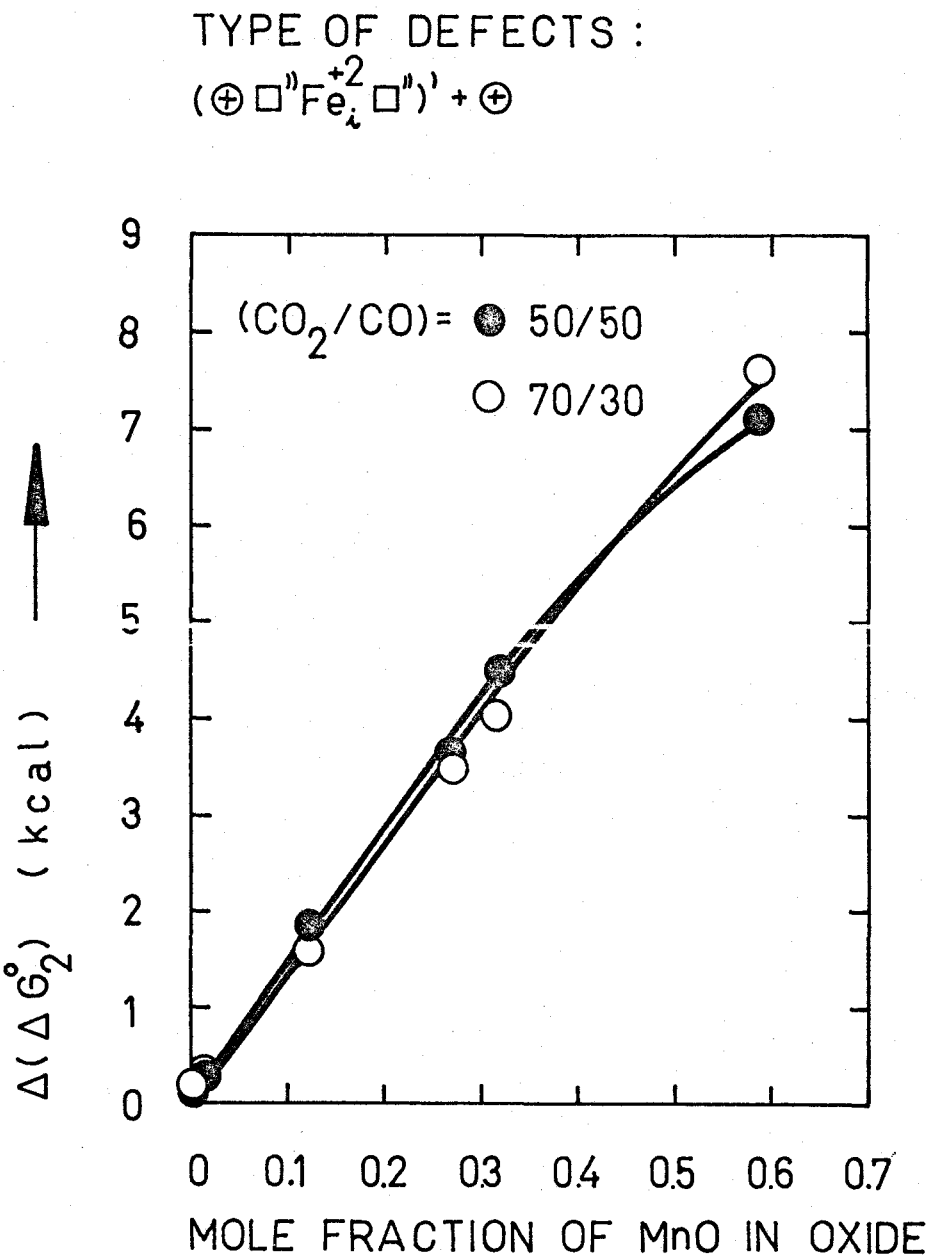

Figure 6.13. Dependence of standard free energy change of oxygen dissolution in FeO-MnO solid solution at 1000°C on mole fraction of MnO in oxide.

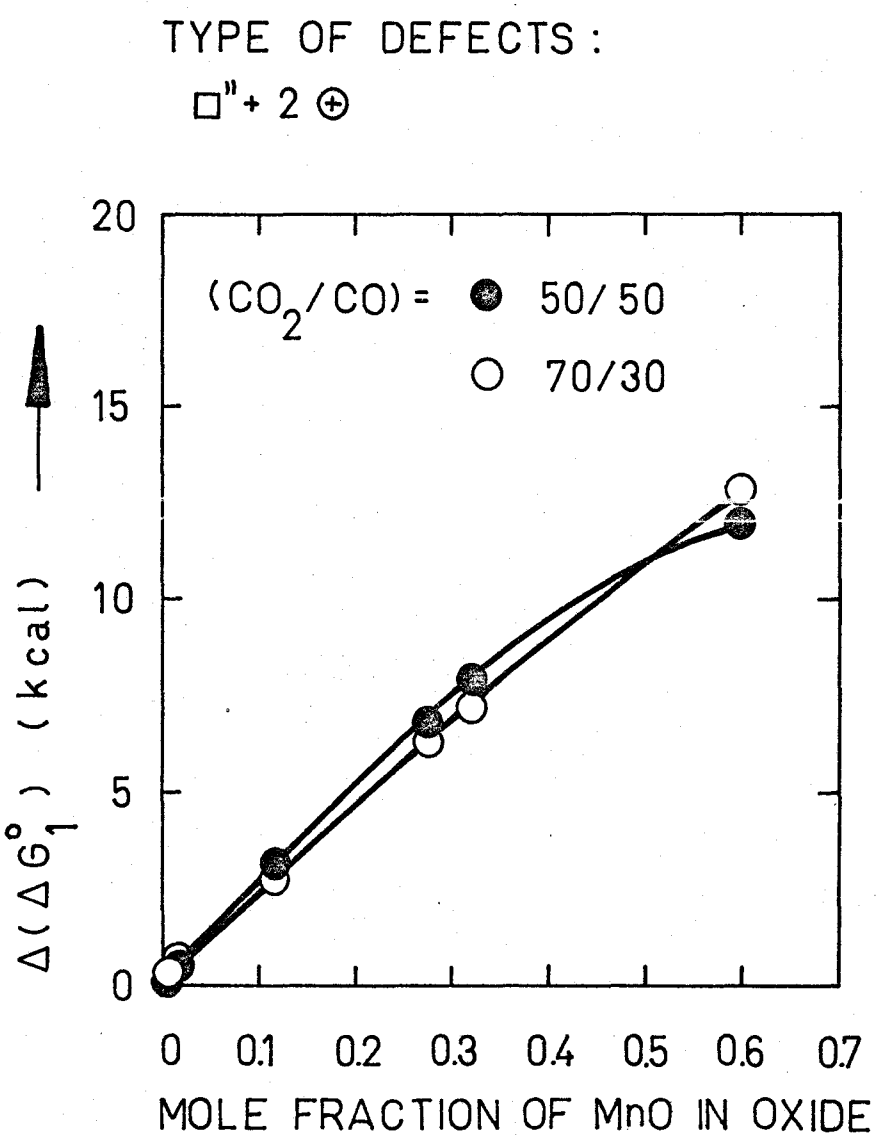

Figure 6.14. Dependence of standard free energy change of oxygen dissolution in FeO-MnO solid solution at 1000°C on mole fraction of MnO in oxide.

$$\Delta(\Delta G_2^\circ) = 15.4\ x_{MnO} \quad [k\ cal] \tag{6.53}$$

and for oxygen potential $CO_2/CO = 70/30$

by $$\Delta(\Delta G_1^\circ) = 21.5\ x_{MnO}\ [k\ cal] \tag{6.54}$$

$$\Delta(\Delta G_2^\circ) = 13.2\ x_{MnO}\ [k\ cal] \tag{6.55}$$

The functional relationship for $x_{FeO} = f\ (x_{MnO})$ could be obtained from the auxiliary plots in Figs. 6.15 and 6.16 which show that the change in log x_{FeO} by addition of x_{MnO} follows a linear relationship. Hence for the $CO_2/CO = 50/50$ atmosphere

$$\log x_{FeO}^1 = -\ 0.59\ x_{MnO} - 0.05 \tag{6.56}$$

$$\log x_{FeO}^2 = -\ 0.56\ x_{MnO} - 0.08 \tag{6.57}$$

similarly, for the $CO_2/CO = 70/30$ atmosphere

$$\log x_{FeO}^1 = -\ 0.72\ x_{MnO} - .17 \tag{6.58}$$

$$\log x_{FeO}^2 = -\ 0.68\ x_{MnO} - .12 \tag{6.59}$$

The subscripts 1 and 2 refer to particular model.

Substitutions of equations (6.52 - 6.59) into 6.50 and 6.51 yield the resulting empirical equation for the $CO_2/CO = 50/50$ atmosphere

$$\log x\ (\square \text{ or } c) = -\ 1.82\ x_{MnO} - 1.06 \tag{6.60}$$

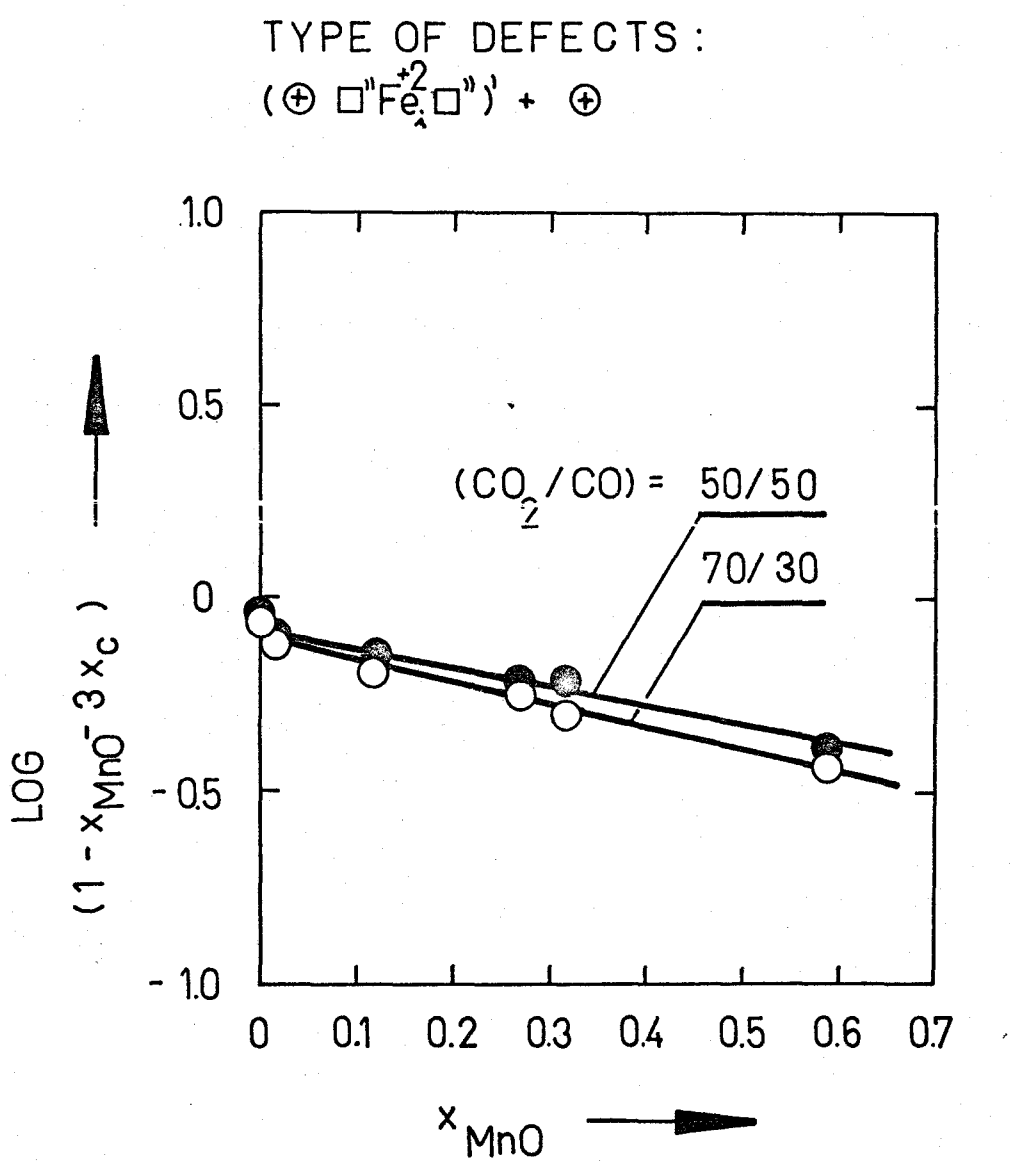

Figure 6.15. Auxiliary plot for the complex type defect model.

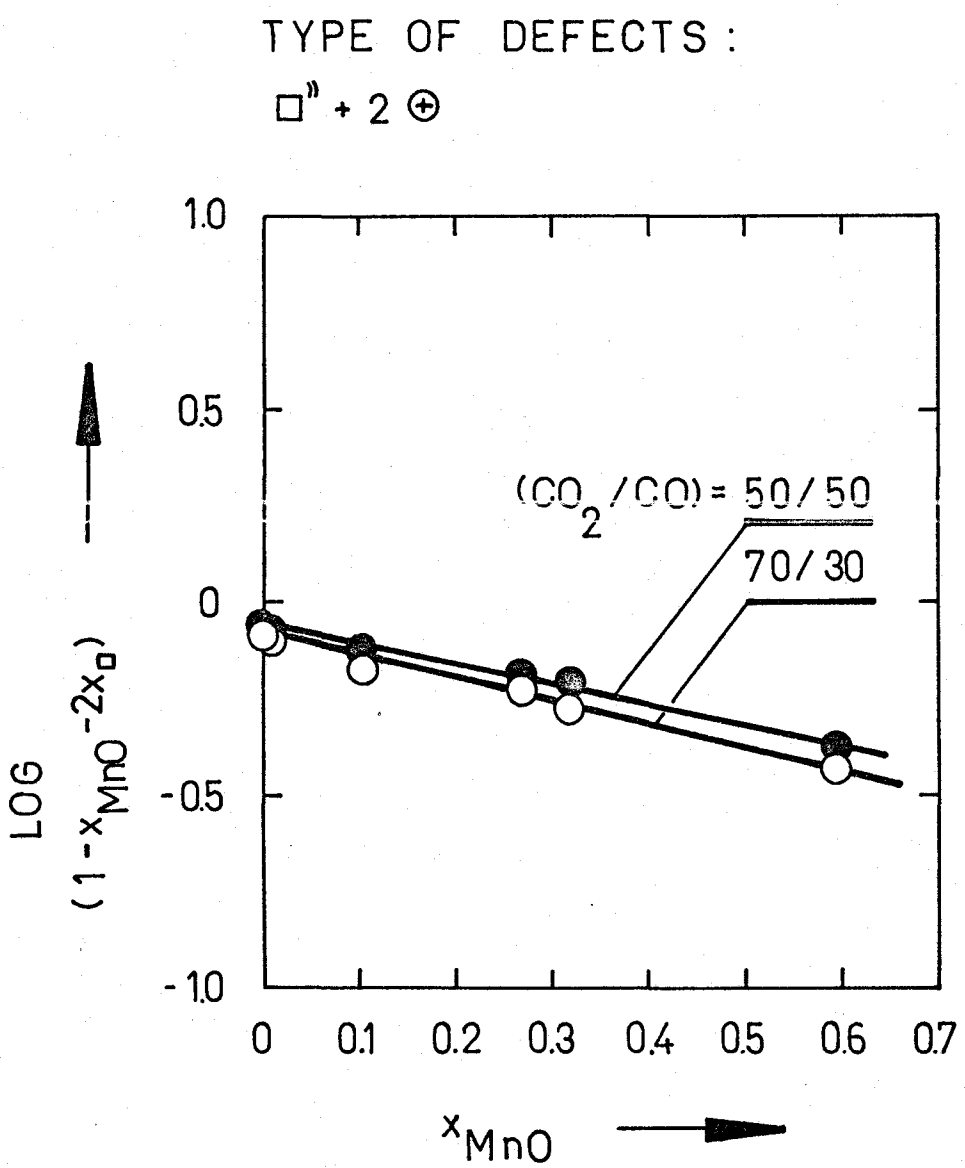

Figure 6.16. Auxiliary plot for the simple type defect model.

and for $CO_2/CO = 70/30$

$$\log x\ (\square \text{ or } C) = -1.91\ x_{MnO} - 0.93 \qquad (6.61)$$

Graphical representation of these two relationships is shown in Fig. 6.17

Unfortunately, the independent theoretical calculations for the change in ΔG° as a function of concentration of the additional element in the considered type of solid solution is complex. Within our knowledge an attempt has not yet been made to apply a statistical thermodynamic approach to these types of systems in the available literature. The type of analysis used in this investigation, nevertheless, shows the possible sources whereby discrepancies exist between concentration of defects calculated from the present experiments and theoretical models considering the equilibrium constant K = constant. For these reasons we can not deduce the most appropriate defect model from comparison of defect concentrations calculated from experiments and using theoretical models. The relationships deduced must be simply regarded as simple empirical correlations of results based upon consistent theoretical considerations for a type of defect consisting of either doubly ionized vacancies or single ionized complexes composed of two vacancies associated with a metal ion in an interstitial site.

6.5 Proposals for Future Work

In order to correlate the experimental oxidation characteristics of the Fe-Mn alloys with theoretical models, the transport and structural properties of the alloy-oxide system must be more completely defined

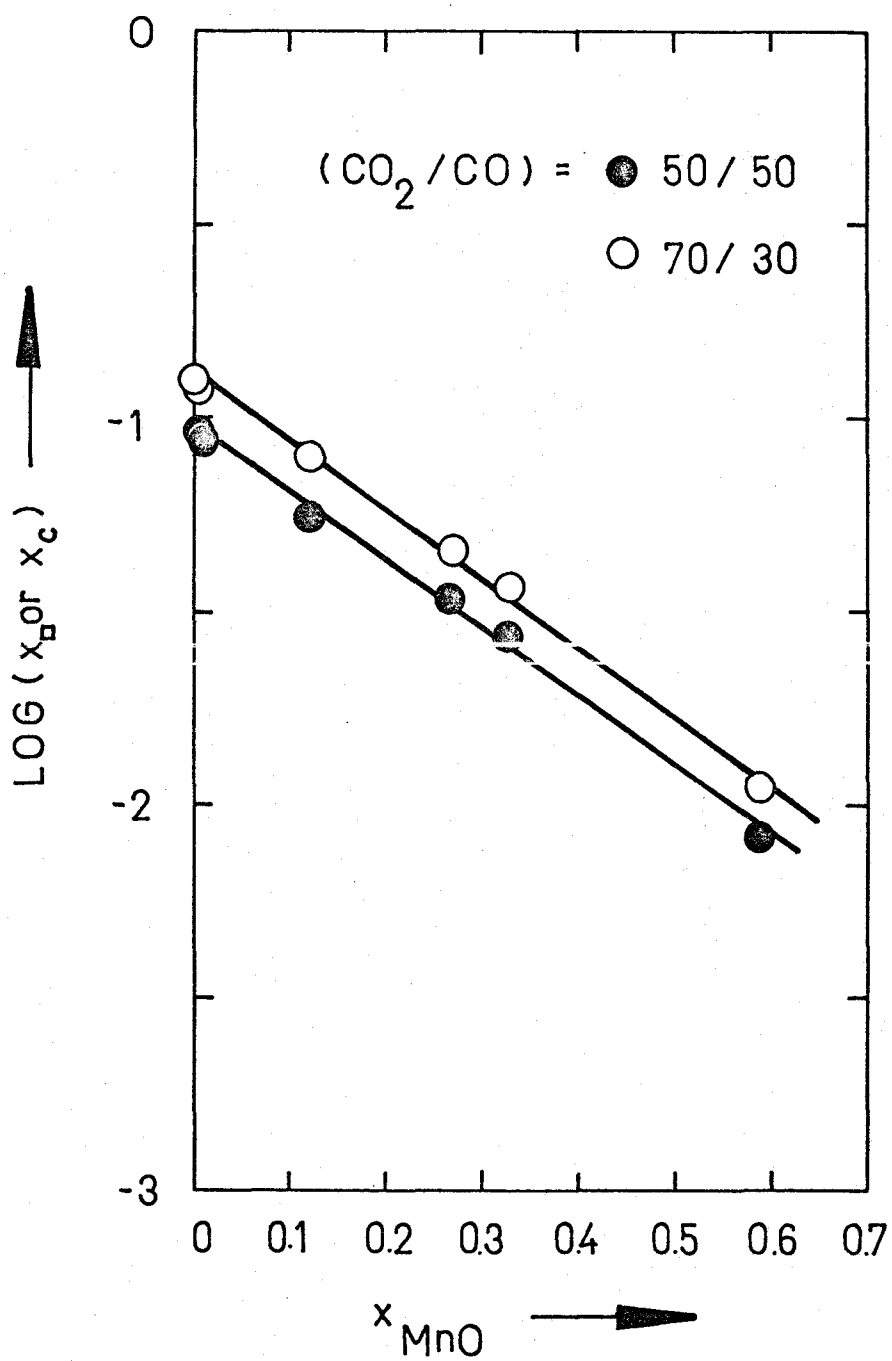

Figure 6.17. Logarithms of defect concentration vs. concentration of MnO in scale.

experimentally and theoretically. The Fe-Mn alloys at 1000°C are well defined thermodynamically and constitutionally. Transport properties and structures have been the subjects of many investigations. The properties of FeO-MnO solid solutions are not well known. There has been some work done, but in general, the transport and structural properties have not yet been sufficiently defined.

An attempt has been made, to define transport and structural properties of solid solutions of FeO-MnO in the present work from thermogravimetric measurements. These calculations are based on a number of assumptions, which must be verified by independent measurements. The transport properties should be confirmed by radioactive tracer measurements of D_{Fe} and D_{Mn} as a function of MnO content in FeO-MnO solid solutions. Measurements of electrical properties are required to elucidate the defect structure of oxides. Also chemical diffusion parameters should be obtained using diffusion couples and electron probe microanalysis. This additional information on the solid solutions of FeO-MnO should enable a detailed application of the general theory of binary alloy oxidation when one phase oxide scale is formed.

CHAPTER VII

CONCLUSIONS

1. The oxidation kinetics of Fe-Mn alloys follow linear and parabolic relationships. The scale consists of wustite with manganese oxide in solid solution.
2. Alloys up to 12% Mn exhibit at the onset of oxidation two linear regions. The first region is dependent upon numerous factors which have not been defined. The second linear region is associated with a rate controlling interfacial reaction. Because the rate of this reaction does not vary with concentration of Mn in the alloy, it is suggested that the dissociation of CO_2 to form adsorbed oxygen and CO is the rate limiting process. At later stages of exposure, the rate of metal diffusion through a scale becomes rate controlling and the oxidation kinetics are parabolic.
3. Alloys with Mn contents greater than 12% obey parabolic oxidation kinetics from very early exposure times due to the ion diffusion rates of metal in the scale.
4. The metal concentration gradients in the scales formed on Fe-Mn alloys are linear and of very small slope which demonstrate that the diffusivities of Fe and Mn under the same oxygen concentration gradient in FeO-MnO solid solutions are approximately of the same magnitude.
5. The parabolic oxidation rate constants decrease with addition of Mn to an iron alloy by an exponential relationship.

6. An analysis was carried out of the parabolic oxidation kinetics by ternary diffusion theory to demonstrate that the diffusivities of both elements in an FeO-MnO solid solution decrease by the addition of MnO and are possibly due to the decrease in concentration of point defects present as metal vacancies and positive holes.

7. X-ray diffraction studies confirmed data from the literature that FeO and MnO form a one-phase solid solution throughout its complete range of composition.

8. An attempt was made to interpret the defect structure of the FeO-MnO solid solution. A comparison of calculated defect concentrations from the present investigation and from theoretical models suggests that the defects may be present as singly ionized complexes containing two ion vacancies or completely ionized iron vacancies, the former exhibiting the smallest deviation from calculated values obtained in the present investigation.

9. Using an analysis due to Zintl[42], calculations show that the standard free energy change of oxygen dissolution in FeO-MnO oxide solid solutions changes linearly with MnO content almost over the entire experimentally tested composition range.

References

1. Wagner, C., Z. Phys. Chem., (B), 21, 25 (1933).
2. Nagel, K., and Wagner, C., Z. Phys. Chem., (B), 25, 71 (1934).
3. Wagner, C., Z. Phys. Chem., (B) 32, 447 (1936).
4. Wagner, C., and Grunwald, K., Z. Phys. Chem., (B), 40, 445 (1938).
5. Carter, R. E. and Richardson, F. D., Trans. AIME, 203, 336 (1955).
6. Turkdogan, E. T., McKewan, W. M. and Zwell, L., J. Phys. Chem., 69, 327 (1965).
7. Gulbransen, E. A., and Andrew, K. F., J. Electrochem. Soc., 101, 3, 128 (1954).
8. Moore, W. J., and Lee, J. K., Trans. Faraday Soc., 48, 916 (1952).
9. Baur, J. P., et al., J. Electrochem. Soc., 110, 185 (1963).
10. Fueki, K., and Wagner Jr., J. B., J. Electrochem. Soc., 112, 384, (1965).
11. Kofstad, P., High-Temperature Oxidation of Metals, Wiley, New York, 1966.
12. Moreau, J., and Benard, J., L' Oxydation des Metaux, Vol. 1, 318, Gauthier-Villars, Paris, 1962.
13. Wood, G. C., Oxidation of Metals, 2, 11 (1970).
14. Wagner, C., Corrosion Science, 9, 91 (1969).
15. Tamman, G., Z. anorg. allg. Chem., 111, 78 (1920).
16. Elliot, J. F., and Gleiser, M., Thermochemistry for Steelmaking, Vol. 1, Addison-Wesley, Mass., 1960.
17. Swaroop, B., and Wagner, Jr., J. B., Trans. AIME, 239, 1215 (1967).
18. Geiger, G. H., Levin, R. L., and Wagner Jr., J. B., J. Phys. Chem. Solids, 27, 947 (1966).
19. Kofstad, P., and Hed, A. Z., J. Electrochem. Soc., 115, 102 (1968).
20. Valet, P. and Raccah, P., Mem. Sci. Rev. Met., 62, 1 (1965).

21. Seltzer, M. S., and Hed, Z. A., J. Electrochem. Soc., 117, 815, (1970).

22. Kleman, M. Mem. Sci. Rev. Met., 62, 457 (1965).

23. Fender, B. E. F., and Riley, F. D., J. Phys. Chem. Solids, 30, 793 (1969).

24. Rizzo, F. and Smith, J. V., J. Phys. Chem., 72, 485 (1968).

25. Hauffe, K., and Pfeiffer, H., Z. Metallk., 44, 27 (1953).

26. Smeltzer, W. W., Acta Met., 8, 377 (1960).

27. Pettit, E., Yinger, R., and Wagner, J. B., Acta Met., 8, 617 (1960).

28. Pettit, E., and Wagner Jr, J. B., Acta Met., 12, 35 (1964).

29. Turkdogan, E. T., McKewan, W. M., and Zwell, L., J. Phys. Chem., 69, 327 (1965).

30. Morris, L. A., and Smeltzer, W. W., Acta Met., 15, 1591 (1967).

31. Fueki, K., J. Electrochem. Soc. Japan, 26E99 (1950).

32. Fueki, K., J. Electrochem. Soc. Japan, 26E120 (1950).

33. Fueki, K., and Wagner Jr., J. B.,J. Electrochem. Soc., 112, 970 (1965).

34. Foster, P. K., and Welch, A. J. E., Trans. Faraday Soc., 52, 1626 (1956).

35. Davies, M. W., and Richardson, F. D., Trans. Faraday Soc., 55, 604 (1954).

36. Eror, N. G. and Wagner Jr. J. B., see ref. 33.

37. T. Kurland, unpublished thesis, Dept. of Chem. Eng., University of Delaware, 1969.

38. Hay, R., Howatt, D. D., and White, J., J. West. Scot. Iron and Steel Inst., 41, 97 (1933-34).

39. Foster, P. K., and Welch, J. J. E., Trans. Faraday Soc., 52, 1636 (1956).

40. Driessens, F. C. M., I., Ber. Busen Phys. Chem., 72, 754 (1968).

41. Engell, H. J., and Kohl, H. K., Z. Electrochemie, 66, 684 (1962).

42. Zintl, G., Z. Phys. Chem. N. F., 48, 340 (1966).

43. Swisher, J. H., Trans. AIME, 242, 1035 (1968).

44. Kubashewski, O., and Evans. E. U., Metallurgical Thermochemistry, Wiley, New York, 1956.

45. E. Sheil, and Kiwit, K., Arch. Eisenhuttenw, 9, 405 (1936).

46. Hessenbruch, W., and Rohn, W., Heraus Vakuumshmelze, p. 247 (1923-1933).

47. Pfeil, L. B., J. Iron and Steel Inst., 119, 501 (1929).

48. Pfeil, L. B., J. Iron and Steel Inst., 123, 237 (1931).

49. Kubachewski, O., and Hopkins, B. E., Butterworths, London, 1962.

50. C. E. Birchenall, A.S.M. Pre-Congress Seminar, "Oxidation of Metals and Alloys", Cleveland, October 17-18, 1970, to be published.

51. Roth, W. L., Acta Cryst., 13, 140 (1960).

52. Kofstad, P., J. Phys. Chem. Solids, 28, 1842 (1967).

53. Lang, Z. Anal. Chem., 10, 8 (1935).

54. Dalvi, A. D., The Electron Probe Microanalyser, Internation Publication, McMaster University, 1969.

55. Seltzer, S. M., and Hed, A. Z., J. Electrochem. Soc., 117, 815 (1970).

56. Dalvi, A., Ph.D. Thesis, McMaster University, Hamilton, 1971.

57. Coates, D. E., and Dalvi, A. D., Oxidation of Metals (to be published) 1971.